Naturskyddsföreningen

Jordens Vänner
Friends of the Earth Sweden

mkg
Miljöorganisationernas kärnavfallsgranskning

YTTRANDE

Stockholm och Göteborg 20 januari 2023

Till:
Strålsäkerhetsmyndigheten
171 16 Stockholm
registrator@ssm.se
patrik.borg@ssm.se

Ert dnr: SSM2022-4839

Yttrande från Naturskyddsföreningen, Jordens Vänner och Miljöorganisationernas kärnavfallsgranskning, MKG, över kraftindustrins kärnavfallsbolag SKB:s forskningsprogram Fud- 2022

Strålsäkerhetsmyndigheten (SSM) har den 3 oktober 2022 skickat kraftindustrins kärnavfallsbolag SKB:s forskningsprogram Fud- 2022 på remiss. Naturskyddsföreningen, Jordens Vänner och Miljöorganisationernas kärnavfallsgranskning, MKG, nedan kallade *föreningarna*, lämnar härmed in ett gemensamt yttrande med synpunkter på forskningsprogrammet och övergripande på behovet av kärnavfallsforskning.

1. Övergripande synpunkter på vikten av att ytterligare forskning om barriärsfunktioner löpande utförs under hela SSM:s stegvisa prövning av kärnbränsleförvaret

I detta avsnitt utvecklar föreningarna närmare varför det är angeläget med ytterligare forskning om hur barriärerna i kärnbränsleförvaret kommer att fungera, och att detta genomförs löpande under hela SSM:s stegvisa prövning av tillståndet för kärnbränsleförvaret enligt kärntekniklagen.

1.1. Grunden för SSM:s ställningstagande och regeringens beslut att godkänna kärnbränsleförvaret

Den 27 januari 2022 meddelade regeringen tillåtlighet enligt miljöbalken och tillstånd enligt kärntekniklagen för ett kärnbränsleförvar i Forsmark. Grunden för regeringens beslut var SSM:s ställningstagande att det finns förutsättningar för att förvaret ska bli tillräckligt säkert. SSM:s ställningstagande bygger på vad myndigheten kallar en ”helhetssyn” där de två konstgjorda barriärerna (kopparkapseln och lerbufferten runt kapseln) samt den tredje barriären berget tillsammans alltid ger förutsättningar för tillräcklig långsiktig miljösäkerhet. De tre barriärerna fungerar enligt myndigheten tillsammans alltid som en tillräckligt robust isolering av det deponerade använda kärnbränslet för att förhindra att skadliga radioaktiva ämnen når människa och miljö.

Att kopparkapseln och lerbufferten kring kapseln är konstgjorda barriärer är uppenbart. Men det finns skäl att påpeka att bergbarriären inte är en alltigenom naturlig barriär, trots att den modelleras som sådan i säkerhetsanalysen.

I själva verket är även bergbarriären till betydande del att anse som en konstgjord barriär, eftersom en viktig del av dess skyddande funktion beror på vad som sker i mötet mellan berget och den bentonitlera som fyller och ska täta tunnlar och schakt. Enligt föreningarnas mening är den svagaste länken i förvarets funktion att förhindra vattenflöden från förvarsdjup till jordytan inte berget och dess

Naturskyddsföreningen
Box 4625, 116 91 Stockholm
Telefon: 08-702 65 00

Jordens Vänner
Box 7048, 402 31 Göteborg
Telefon: 031 -12 18 08

Miljöföreningarnas kärnavfallsgranskning, MKG
Fjällgatan 2, 413 17 Göteborg
Telefon: 031-711 00 92

sprickor i sig, utan vattenflöden genom den lera som placerats i tunnlar och schakt som måste svälla och hålla minst lika tätt som berget i sig för att denna barriärfunktion ska fungera som tänkt.

Föreningarna menar att SSM har intagit ståndpunkten att en ”helhetssyn” på barriärernas sammanlagda funktion gör att det finns förutsättningar för att kärnbränsleförvaret kan bli tillräckligt säkert. Denna inställning är grundad i att det i säkerhetsanalysen för kärnbränsleförvaret tagits fram s.k. ”what if”-scenarier i den modellerade säkerhetsanalysen för förvaret för att undersöka vad som händer om inte alla barriärer fungerar som tänkt. Dessa visar teoretiskt att om endast ett par av barriärerna fungerar som tänkt, kommer det i ett tusenårsperspektiv bara bli begränsade utsläpp av radioaktiva ämnen i Forsmarksområdet.

Föreningarna menar att sådana teoretiska beräkningar inte kan användas som utgångspunkt för SSM:s ställningstaganden. Det viktiga i en miljöprövning är att SSM:s riskgräns inte ska överskridas och då måste all tre barriärerna fungera som tänkt i säkerhetsanalysens modeller. Om riskgränsen riskerar att överskridas ska kärnbränsleförvaret inte ges tillstånd enligt kärntekniklagen eller miljöbalken. Det var denna risk en för att riskgränsen överskreds som fick mark-och miljödomstolen att i januari 2018 avstyrka att regeringen skulle ge tillåtlighet för kärnbränsleförvaret.

Den viktigaste barriären i kärnbränsleförvaret är kopparkapseln. Om kopparkapseln i sig inte fungerar som tänkt förverkligas de allvarligaste riskscenarierna i ”what if”-analyserna och det blir en mer omfattande radioaktiv förorening i Forsmarksområdet. I ett tusenårsperspektiv riskeras då att det blir en radioaktiv zon ovanför kärnbränsleförvaret i Forsmark där människor inte kan bo, äta den mat som odlats området eller dricka vatten från grundvattenreservoaren. Dessutom kommer havet att bli förorenat av radioaktiva ämnen.

Föreningarna menar att det finns ett vetenskapligt underlag för att säga att det finns betydande risker för att kopparkapselns långsiktiga integritet är mycket sämre än det som angetts av kärnkraftindustrins kärnavfallsbolag SKB. Detta stöds av uttalanden av från industrin oberoende och framstående korrosionsexpertis. Föreningarna anser att det saknas tillräcklig kunskap om kopparkapselns funktion för att använda de antaganden som görs i modellerna i säkerhetsanalysen.

Föreningarna menar vidare att det även finns det en betydande risk att den omgivande lerbuffertens isolerande funktion bryts ner när ämnen från kopparkapselns nedbrytning tränger in i leran. Till detta tillkommer problem för lerbufferten att överhuvudtaget uppnå ett isolerande tillstånd i det torra Forsmarkberget. Den lera, bentonitlera, som används i bufferten och behöver vatten för att svälla och bli tät. Den svällande funktionen kan förstöras av värmen från det använda kärnbränslet. Föreningarna anser att det saknas tillräcklig kunskap om lerbuffetens funktion för att använda de antaganden som görs i modellerna i säkerhetsanalysen.

Om kopparkapseln och lerbufferten inte är fullgott fungerande barriärer återstår berget. I säkerhetsanalysen för kärnbränsleförvaret är kvaliteten på berget i Forsmark en viktig komponent. Berget är relativt sprickfritt och eftersom säkerhetsanalysen utgår från att läckande radioaktiva ämnen måste vandra genom berget och mindre sprickor i berget spelar det enligt kärnavfallsbolaget och SSM mindre roll hur kopparkapseln och lerbufferten fungerar.

I praktiken kommer det dock inte vara bergets funktion utan hur hög tätningsgrad tunnlar och schakt får som utgör ”bergets” barriärsfunktion. Tunnlar och schakt ska tätas med betongpluggar och fyllas med bentonitlera som ska svälla och täta när grundvatten tränger in. Föreningarna menar att det saknas tillräcklig kunskap om detta kommer att fungera på så sätt att dessa konstgjorda barriärer verkligen blir lika täta som det verkliga berget. Det kommer vara extra svårt att nå täthet i Forsmarkberget som är under högt vattentryck och där tryckdifferenser mellan större sprickor i olika delar av förvaret ger risk för att vatten ska börja flöda längs tunnlarna. Föreningarna anser att det saknas tillräcklig kunskap om ”bergets” funktion för att använda de antaganden som görs i modellerna i säkerhetsanalysen.

1.2. Föreningarnas begäran om rättsprövning av regeringens beslut att godkänna kärnbränsleförvaret

Enligt vad som framgått ovan anser föreningarna att det saknas tillräcklig kunskap om kärnbränsleförvarets samtliga barriärsfunktioner för att validera de antaganden som görs i modellerna i säkerhetsanalysen. Enligt de allmänna hänsynsreglerna i miljöbalken är ett villkor för att få tillstånd för kärnbränsleförvaret att tillräcklig kunskap finns vid den tidpunkt tillståndet ges. Dessutom måste

försiktighetsprincipen efterlevas vid tillståndsprövningen enligt miljöbalken. Ett tillstånd enligt kärntekniklagen måste dessutom följa de allmänna hänsynsreglerna i miljöbalken[1].

Föreningarna anser att det saknas tillräcklig kunskap för SSM – och därmed regeringen – för att kunna hävda att det finns förutsättningar att kärnbränsleförvaret ska bli tillräckligt säkert. Föreningarna har därför begärt rättsprövning i Högsta förvaltningsdomstolen för att få det prövat om kunskapsvillkoret och försiktighetsprincipen enligt miljöbalkens allmänna hänsynsregler har tillämpats korrekt av regeringen i besluten i januari 2022 att tillåta kärnbränsleförvaret enligt miljöbalken och att ge tillstånd enligt kärntekniklagen.

Ett beslut från domstolen förväntas under våren 2023. Om domstolen har synpunkter på kunskapsläget i relation till tillståndsfrågan kan detta komma att påverka frågan om framtida forskning om kärnbränsleförvarets barriärer. Prövningen är emellertid en så kallad lagprövning, och Högsta förvaltningsdomstolen kan bara upphäva regeringsbesluten om man anser det tydligt strider mot en rättsregel. Även om domstolen inte kommer fram till att regeringen gjort fel i besluten att godkänna kärnbränsleförvaret, menar föreningarna att den kunskapsbrist som finns bör påverka SSM:s fortsatta prövning av kärnbränsleförvaret i den s.k. stegvisa prövningen enligt kärntekniklagen.

1.3. SSM:s stegvisa prövning enligt kärntekniklagen

SSM ska enligt kärntekniklagstiftningen godkänna ett flertal säkerhetsanalyser för kärnbränsleförvarets långsiktiga säkerhet innan uppförande (PSAR), provdrift (förnyad SAR) och drift (SAR) kan påbörjas. Vid varje prövning av ärenden enligt kärntekniklagen ska miljöbalkens allmänna hänsynsvillkor följas. Det betyder att SSM vid upprepande tillfällen ska pröva om kunskapsvillkoret och försiktighetsprincipen enligt miljöbalkens praxis är uppfyllda. Det första tillfället kommer inom några år då SSM ska ta beslut om den säkerhetsanalys, PSAR, som kärnavfallsbolaget SKB förväntas lämna in 2024. Ett beslut att godkänna säkerhetsanalysen är en förutsättning för att bolaget ska få börja bygga kärnbränsleförvaret.

Vid varje beslutstillfälle måste det visas att den kunskap som finns för varje barriärs funktion, och för barriärerna tillsammans, är tillräcklig för att garantera att den fungerar som tänkt i säkerhetsanalysen. Kravet på kunskap om barriärernas funktion bör bli högre för varje beslut.

Föreningarna menar enligt ovan att det fortfarande saknas tillräcklig kunskap som visar hur alla de tre barriärer (kopparkapsel, lerbuffert och berg) som ska utgöra grunden för den långsiktiga säkerheten kommer att fungera i en verklig förvarsmiljö. Dessutom saknas det kunskap hur barriärerna är beroende av varandra, t.ex. hur nedbrytningen av en barriär påverkar andra barriärer.

En viktig frågeställning som SSM måste hantera framöver i prövningen av framtida säkerhetsanalyser i den stegvisa prövningen är hur mycket kunskap som är tillräcklig om funktionen av var och en av de tre barriärerna för att godkänna nästa steg. En kanske ännu viktigare frågeställning är hur mycket kunskap som SSM får tillgång till och som visar att en barriär inte kommer att fungera som tänkt, blir tillräcklig för att myndigheten med ”helhetssynen” på barriärernas funktion i en framtid kan komma att underkänna säkerhetsanalysen och därmed inte längre fortsätta att godkänna kärnbränsleförvaret. För ett sådant ställningstagande kan miljöbalkens villkor på tillräcklig kunskap och att försiktighetsprincipen ska tillämpas utgöra en viktig juridisk grund.

1.4. Vikten av ytterligare forskning om barriärsfunktionerna genomförs

Som angetts ovan menar föreningarna att varken kunskapsvillkoret uppfyllts eller försiktighetsprincipen följts när regeringen gav tillåtlighet enligt miljöbalken eller tillstånd enligt kärntekniklagen för kärnbränsleförvaret. Eftersom SSM:s ställningstagande låg till grund för regeringens beslut är föreningarna kritiska till SSM:s inställning om att en ”helhetssyn” innebär att det finns förutsättningar att kärnbränsleförvaret kan bli tillräckligt säkert.

Föreningarna menar att det främst är kunskaper om kopparkapselns långsiktiga integritet som saknas, en inställning som det finns en oberoende och framstående vetenskaplig korrosionsexpertis som stödjer. Men föreningarna menar även att det saknas tillräcklig kunskap om lerbuffertens förmåga att

[1] Enligt §5a i kärntekniklagen ska ”ska 2 kap. och 5 kap. 3-5 §§ miljöbalken tillämpas” vid prövning av ärenden enligt lagen. Det gäller således även godkännandet av säkerhetsanalyser i SSM:s stegvisa prövning. 2 kap. i miljöbalken är de allmänna hänsynsreglerna.

skydda kopparkapseln, särskilt i framtida scenarier där kapseln håller på att brytas ner. Kunskapen är mycket bristfällig om lera/betongpluggar kommer att kunna hålla lika tätt som berget i Forsmark efter tillslutning av kärnbränsleförvaret. Något som krävs för att bergets barriärfunktion ska kunna tillgodoräknas i säkerhetsanalyserna för förvaret på det sätt som görs.

Föreningarna menar således att det finns ett betydande behov av mer forskning om barriärernas funktion. I detta avseende är kraftindustrins kärnavfallsbolag SKB:s aktuella forskningsprogram Fud-2022 helt otillräckligt, vilket föreningarna utvecklar närmare i nästa avsnitt.

2. Specifika synpunkter som rör barriärernas funktion

I detta avsnitt tar föreningarna upp de kunskapsbrister som finns om barriärernas funktion i en kärnbränsleförvarsmiljö.

2.1. Frågeställningar som rör kopparkapsels långsiktiga integritet i kärnbränsleförvaret

Sedan över 15 år har det pågått en vetenskaplig kontrovers om hur koppar som kapselmaterial fungerar i en förvarsmiljö. Föreningarna menar att det är tydligt att denna fråga ännu inte har undersökts på ett vetenskapligt fullgott sätt. Ett huvudproblem är att kraftindustrin och dess kärnavfallsbolag SKB helt saknar intresse av en genomgripande vetenskaplig forskningsinsats, eftersom en sådan kan utmynna i ett slutgiltigt forskningsresultat om att koppar inte är ett lämpligt kapselmaterial för kärnbränsleförvaret.

Problemet förvärras av det saknas insyn enligt offentlighetsprincipen i bolagets forskningsverksamhet. Dessutom är det lagstadgat att det just är industrin och dess kärnavfallsbolag som är ansvariga för att upptäcka brister i den av dem valda kärnbränsleförvarsmetoden, vilket gör det svårt för andra aktörer att få resurser för fristående forskning.

Efter att regeringen med stöd av SSM nu har givit tillstånd förvarsmetoden enligt kärntekniklagen blir kunskapsläget rörande kopparkapselns funktion en fråga för tillsyn hos myndigheten. Detta ger SSM ett nytt utgångsläge för att ta itu med frågorna om kunskapsbrist med det allvar de förtjänar. Föreningarna vill påminna om att kunskapsläget för varje barriär i kärnbränsleförvaret måste vara det bästa möjliga innan SSM i en framtid kan godkänna en säkerhetsanalys för drift av förvaret (SAR).

Ny kunskap om förutsättningarna för kopparkorrosion

Kärnavfallsbolaget SKB har i 45 år bedrivit forskning om kopparkapslar och bentonitlera i en kärnbränsleförvarsmiljö. Det är då anmärkningsvärt att bolaget inte förrän i det nu aktuella forskningsprogrammet Fud-2022 redovisar att syrgas i försök som innehåller koppar och bentonitlera inte endast konsumeras av kopparkorrosion utan även i bentonitleran via en snabb reaktion med pyrit. Detta är egentligen känt sedan tidigare men nu har bolaget för första gången tydligt medgivit att så är fallet[2]. Att syreförbrukningen i grundvatten, t.ex. i spalter i försökspaket, är mycket snabb är känt sedan länge[3].

Frågeställningen hanteras i avsnitt 10.1.1 på sidan 146 där resultat från nya försök redovisas. Kärnavfallsbolaget skriver att ”de nya mätningarna visar å andra sidan tydligt att syrgas mycket väl kan förbrukas i bentonit och att detta tycks ske genom oxidation av pyrit”. Detta syns även tydligt i figur 10-2. Bolaget hänvisar till en intern rapport[4] som bifogas som bilaga 1.

För kärnavfallsbolaget SKB medför dessa uppgifter ett stort förtroendeproblem, då bolaget i alla relevanta bolagsrapporter genom åren som redovisat resultat från försök i Äspö-laboratoriet (LOT, Prototyp, MiniCan) förklarat den oväntat kraftiga kopparkorrosionen som ägt rum som endast orsakad av kopparkorrosion från syre instängd i försöken. Syret har främst funnits inne i bentonitlera – något

[2] I FE-försöket som installerades i mitten på 2010-talet blev stora tunnlar fyllda med bentonitlera syrgasfria på några månader. Se figur 9 på sidan 296 i ”Implementation of the full-scale emplacement (FE) experiment at the Mont Terri rock laboratory”, Müller et al., Swiss J Geosci, 110 (287–306), 2017 (https://sjg.springeropen.com/articles/10.1007/s00015-016-0251-2).

[3] Se REX-försöket från slutet av 1990-talet: ”O2 depletion in granitic media: The REX project, Puigdomenech et al., SKB TR-01-05, February 2001 (https://skb.se/publikation/18352).

[4] ”Gas phase composition during the unsaturated period: Status report”, Åkesson & Laitinen, SKB 1983850, 2022-06-10.

som nu visats inte vara fallet eftersom detta syre snabbt förbrukats och inte kunnat ge upphov till korrosion.

Föreningarna finner det därför anmärkningsvärt att avfallsbolaget inte har tagit hänsyn till denna nya kunskap i nuvarande FUD 2022. I avsnitt 8.1.2 på sidan 121 om nulägeskunskapen om korrosion under oxiderande förhållanden skriver bolaget följande:

> ”Data från tidigare fältförsök med koppar i förvarsliknande miljöer har sammanställts och analyserats med avseende på allmän korrosion (massförlust) och på vilka miljöparametrar som samvarierar med korrosionsdjupet (Johansson et al. 2019, Johansson 2019). Analys av data från försöken MiniCan, LOT, ABM och Febex visar att korrosionsdjupet korrelerar med den uppskattade totala mängden initial syrgas i bentonit och luftfyllda spalter i närområdet”.

Rapporten Johansson (2019) är en intern bolagsrapport[5] som bifogas som bilaga 2[6]. Utgående från kunskapen att syrgas i både grundvatten och lera snabbt förbrukats är hela den analys som finns i rapporten uppenbart felaktig. Den omfattande kopparkorrosion som observerats i försöken kan inte förklaras med korrosion från instängd syrgas.

SSM måste nu ta detta i beaktande både vid fortsatta utvärderingar av säkerhetsanalyser och vid granskningen av bolagets forskningsprogram. Om kopparkorrosionen i kärnbränsleförvarslikande miljöer inte kan förklaras som kommande från initialt instängd syrgas utan i stället är kontinuerlig, är korrosionen 100 till 1000 gånger snabbare än vad som antagits i kärnavfallsbolagets säkerhetsanalyser. Kunskapsbristen om varför det är så och exakt vilka processer som är inblandade måste åtgärdas.

Korrosion i syrgasfritt vatten

I avsnitt 8.1.13 på sidan 122 i Fud-rapporten står det rörande den KTH-forskning som bedrivits på kopparkorrosion i syrgasfritt vatten:

> ”Som rapporterats i tidigare Fud-program har SKB studerat processen ingående, utan att finna något stöd för KTH-forskarnas uppfattning”, samt
>
> ”Hultquist (KTH) och medarbetare har inte visat att den vätgas som bildats i deras experiment korrelerar med den massa de bildade kopparkorrosionsprodukterna borde ha”.

Föreningarna vill påpeka att termodynamiken för kopparkorrosion i rent syrgasfritt vatten har uppdaterats under de senaste 45 åren men kärnavfallsbolaget SKB envisas med att förlita sig på gamla jämviktsdata för ren kopparoxid. Moderna teoretiska beräkningar vilka är verifierade med experiment från flera olika forskargrupper visar på mycket mer omfattande kopparkorrosion i rent syrgasfritt vatten. Korrosionen sker via hydroxid- och vätesatt kopparoxidbildning på kopparytan, men även inne i kopparmetallens korngränser. Detta kan även förklara att mer vätgas kan detekteras än vad som kan förväntas av de korrosionsprodukter som bildas på kopparytan. Dessutom sker detta under en långsam väteladdning av kopparmetallen.

Föreningarna menar att det behövs fortsatt forskning inom området korrosion i syrgasfritt vatten.

Spänningskorrosion, kopparkrypning och väteförsprödning i koppar

I avsnitt 8.1.5 på sidan 123 behandlas frågeställningar som rör spänningskorrosion. Föreningarna menar att kärnavfallsbolaget SKB nedvärderar betydelsen av sulfidinducerad spänningskorrosion (SCC) i koppar trots att forskarvärlden är överens om dess existens och laboratorieförsök visar att det kan vara ett betydande problem för kopparkapseln i kärnbränsleförvaret.

Sådana försök görs vid högre sulfidhalter för att påskynda processen, vilket kärnavfallsbolaget ser som ett skäl att kritisera forskningsresultaten och inte tillmäta processen betydelse. Generellt tar industriella verksamheter resultaten från denna typ av laboratorietester på stort allvar. Om sprickor

[5] ”Corrosion of copper in repository-like field tests: Compilation and analysis of data”, J. Johansson, SKB Dokument ID 1713264, 2019-04-04

[6] Referensen Johansson et al. (2019) är endast ett konferensbidrag med ett referat av innehållet i Johansson (2019).

uppstår i ett material, om än vid förhöjda halter av korrosionsdrivande joner, så är förståelsen att sprickor kommer i den verkliga industrimiljön förr eller senare. Material som drabbas av sprickor i accelererade laboratorietester blir underkända och får ej användas för kritiska komponenter inom industrin. Föreningarna finner det anmärkningsvärt att denna grundläggande princip inte tillämpas av avfallsbolaget SKB.

En nyligen publicerad studie med resultat från ny forskning vid KTH visar dessutom att både väte och svavel tränger in i koppar och skapar spänningar i koppargittret, även vid normala grundvattenhalter av sulfid [7]. Studien är en uppföljning på en tidigare studie[8]. Studierna bifogas som bilaga 3 och 4. Forskningen ger en mekanistisk förklaring till varför både spänningskorrosion och väteförsprödning kan förväntas om koppar används kärnbränsleförvaret. I studien är det dessutom beskrivet hur SKB har försummat effekten av väte i den sulfidinducerad spänningskorrosionsprocessen av koppar.

Föreningarna vill även påpeka att det faktum att och svavel tränger in i kopparn på det sätt som visas i KTH-forskningen påverkar krypduktiliteten på ett kritiskt sätt och initierar både krypbrott och väteförsprödning, särskilt kopplat till svetsfogarna i kopparkapseln. Detta är av relevans för avsnitten 8.2.1 på sidan 127 om kopparkrypning och avsnitt 8.2.2 på sidan om väteförsprödning.

Föreningarna menar att det behövs fortsatt forskning inom områdena spänningskorrosion, kopparkrypning och väteförsprödning i koppar. SSM bör stödja den forskning som sker vid KTH.

Brytningen av LOT-experimentet och Prototypförvaret

Föreningarna har under 2019 och 2020 i en omfattande dialog med SSM visat att kärnavfallsbolaget SKB inte följde ett vetenskapligt angreppsätt eller analysmetoder vid upptaget av de två försökspaketen i LOT-experimentets som togs upp hösten 2019. Dialogen är dokumenterad i bilagorna till det yttrande till regeringen som föreningarna skickade in den 11 juni 2021[9].

Föreningarna har i ett yttrande till regeringen den 4 november 2021 framfört att det nuvarande LOT-försöket kan utnyttjas för att på ett kraftfullt sätt kan öka kunskapen om hur koppar fungerar i en kärnbränsleförvarsmiljö[10]. Genom att under ännu mer kontrollerade former driftsätta och bryta ett antal nya LOT-försökspaket där syrgasförbrukningen mäts, kan den kunskap om kopparkorrosion som redan finns från upptagna LOT-försökspaket utvärderas på nytt. Detta är särskilt viktigt med tanke på att hittillsvarande utvärderingar gjorts med det helt felaktiga antagandet all syrgas inneslutet i försökspaketen lett till kopparkorrosion (se ovan).

Föreningarna menar att det sista LOT-försökspaketet (S3) som nu funnits i en kärnbränsleförvarsmiljö i snart 25 år inte får brytas förrän ovanstående försöksprogram givit den kunskap som behövs för att på bästa sätt genomföra brytningen för att optimera kunskapstillförseln.

Föreningarna menar även att SSM måste se till att det i samband med kärnavfallsbolagets brytning av prototypförvaret tas fram kunskap om kopparkorrosion på ett vetenskapligt sätt.

Behov av nya försök för att undersöka hur koppar fungerar som kapselmaterial i en simulerad kärnbränsleförvarsmiljö

Enligt personliga kontakter med kärnavfallsbolaget SKB har föreningarna fått uppgiften att bolaget i nutid bedriver försök i egen regi i ett laboratorium med koppar och lera där syrgashalten i försöken

---

[7] ”Penetration of corrosive species into copper exposed to simulated O2-free groundwater by time-of-flight secondary ion mass spectrometry (ToF-SIMS)”, Yue et al., Corrosion Science 210 part 2, January 2023 (https://www.sciencedirect.com/science/article/pii/S0010938X2200751X). Den artikel som bifogas som bilaga är komprimerad för att ta mindre plats. En artikel i full uppläsning kan laddas ner med länken. Artikeln är i ”public domain”.

[8] ”Corrosion-induced microstructure degradation of copper in sulfide-containing simulated anoxic groundwater studied by synchrotron high-energy X-ray diffraction and *ab-initio* density functional theory calculation”, Zhang et al., Corrosion Science, 184, 15 May 2021. Den artikel som bifogas som bilaga är komprimerad för att ta mindre plats. En artikel i full uppläsning kan laddas ner med länken. Artikeln är i ”public domain”. (https://www.sciencedirect.com/science/article/pii/S0010938X21001566).

[9] Yttrandet med bilagor finns här: https://www.mkg.se/nyheter/mkg-och-medlemsorganisationer-till-regeringen-sag-nej-till-karnbransleforvaret-eller .

[10] Yttrandet finns här: https://www.mkg.se/nyheter/mkg-med-medlemsforeningar-i-ett-nytt-yttrande-till-regeringen-utnyttja-lot-forsoket-innan .

kontrolleras. SSM bör följa upp detta med bolaget eftersom det finns en risk att resultaten från försöken inte publiceras om de visar att koppar korroderar även efter att syrgasen förbrukats.

Föreningarna har sedan länge ansett att det för utföras storskaliga försök med autoklaver i laboratorier för att studera koppar och lera i en kontrollerad miljö med syrgasmätning. Förutom att följa det arbete kärnavfallsbolaget SKB utför bör SSM se till att sådana försök görs av från industrin oberoende forskare.

Behov av nya försök för att undersöka hur koppar fungerar som kapselmaterial i reell kärnbränsleförvarsmiljö

Kärnavfallsbolaget SKB anger i avsnitt 4.10 (s. 71) att bolaget avser att avsluta försöksverksamheten i berglaboratoriet under Äspö vid Oskarshamns kärnkraftverk. Föreningarna menar att SSM bör ange att så inte får ske, utan att det finns behov av fortsatta studier av hur koppar och lera fungerar i en reell kärnbränsleförvarsmiljö. Förutsättningen för att delar av sådana försök även innehåller använt kärnbränsle som strålkälla bör utredas.

Föreningen gör bedömningen att det kommer att ta upp till 15 till 20 år innan SSM kommer att godkänna en säkerhetsanalys (SAR) för ordinarie drift av ett kärnbränsleförvar. Det betyder att det finns tid för nya långtidsförsök av den typ som LOT-försöket var ett exempel på. Fokus på denna typ av försök bör vara att med noggranna mätningar av tillgången på syrgas vid kopparytan undersöka hur kopparytan påverkas, både vad gäller hur mycket korrosion som sker, i vilken mån det sker gropfrätning och hur långt in i kopparn olika ämnen tränger.

Föreningarna anser dessutom att i det i samband med att provdrift av kärnbränsleförvaret påbörjas ett omfattande och långsiktigt försöksprogram för att undersöka hur koppar och lera fungerar i Forsmarkberget.

Behov av studier på plats i SFR för att studera risken för korrosion från läckströmmar från högspänningskablarna till Finland

Föreningarna anser att det fortfarande inte är tillräckligt utrett om det finns problem i Forsmark med att läckströmmar under jord från högspänningskablarna Fenno-Skan mellan Finland och Sverige kan orsaka korrosion. MKG uppmärksammade SSM på denna frågeställning redan 2012 som en möjlig orsak till den omfattande och oväntade korrosion som äger rum i förvaret förkortlivat radioaktivt avfall SFR. Myndigheten gjorde då en utredning (SSM2012-2658). Föreningarna menar att de svar som kärnavfallsbolaget SKB då lämnade endast utgick från teoretiska resonemang i stället för att utföra mätningar och försök nere i SFR. Med tanke på den fortsatt höga korrosionen, bland annat på containrarna med det feldeponerade avfallet i SFR, anser föreningarna att det behövs ett forskningsprojekt på plats nere i förvaret för att i detalj experimentellt utreda frågeställningen.

2.2. Frågeställningar som rör barriärfunktionen hos lerbufferten

Föreningarna anser att SSM noggrant måste följa upp den forskning som kärnavfallbolaget SKB gjort på hur lerbufferten fungerar i en förvarsmiljö. Två frågor som särskilt bör studeras är hur bentonitlerans svällande och tätande funktion påverkas av att kopparkorrosionsprodukter tränger in i leran och hur dessa funktioner påverkas av att leran hettas upp och torkar ut.

Föreningarna menar att sådan kunskap bör kunna finnas i resultaten från upptagen av första delen av prototypförvaret och från LOT-upptag, men att det finns en risk att bolaget inte redovisat dessa eftersom det skulle visa brister i funktionen.

SSM bör stödja av industrin oberoende forskning inom området.

2.3 Frågeställningar som rör barriärfunktionen hos lera/betongpluggar i tunnlar/schakt

Föreningarna menar att det fortfarande saknas kunskap som visar att barriärfunktionen hos lera/betongpluggar i tunnlar/schakt fungerar som tänkt i kärnbränsleförvaret. I forskningsprogrammet verkar kärnavfallsbolaget SKB utgå från att leran i deponeringstunnlarna sväller och blir täta oberoende av de hydrologiska förutsättningarna i deponeringstunnlarna. Föreningarna menar att det behövs forskning som visar att det är så.

3. Specifika synpunkter på andra punkter i programmet

3.1. Den alternativa metoden djupa borrhål

Kärnavfallsbolaget SKB anger i avsnittet 14.13.2 om alternativa metoder på sidan 77 att bolaget inte planerar att bedriva någon egen forskning eller utveckling om den alternativa metoden djupa borrhål. Föreningarna menar till skillnad från bolaget att det pågår en utveckling av metoden internationellt, särskilt av bolaget ”Deep Isolation”[11] och att denna utveckling bör beskrivas i forskningsprogrammet.

3.2. Grundvattenströmning från djupet i Forsmark

Föreningarna har i prövningen av tillståndet för förvaren för kortlivat radioaktivt avfall, SFR, påpekat att det finns en risk att de geohydrologiska modelleringar som finns i säkerhetsanalysen kan ha brister i och med att inte tillräcklig hänsyn tagits till storregionala grundvattenflöden. Därmed kan risken underskattas för att radioaktiva ämnen relativt snabbt läcker ut i Öregrundsgrepen ovanför förvaret när det förslutits.

I avsnitt 7.4.7 på sidan 69 skriver kärnavfallsbolaget SKB att ”under de senaste åren har hydrogeologisk modellering utvecklats så att geokemiska processer och transportprocesser nu kan integreras med flödesmodelleringen. Föreningarna menar även att utvecklingen av hydrogeologisk modellering bör utnyttjas för att genomföra bättre studier av grundvattenflödena både för SFR och för kärnbränsleförvaret. SSM bör se till att från industrin oberoende studier genomförs.

3.3. Övervakning av rörelser av berget i Forsmark

Mellan 2005 och 2009 hade kärnavfallsbolaget SKB ett nätverk av GPS-stationer i Forsmarkområdet för att studera om olika delar av skjuvzonen genom området rörde sig i förhållande till andra. Sådana rörelser skulle kunna påvisa att zonen är seismisk aktiv. Efter att försöket gett resultat som var svårtydbara lades försöket ner i stället för att förbättra det och ta fram långa försöksserier.

Föreningarna menar att det behövs ny forskning på rörelser av berget i Forsmark.

3.4. Övervakning och information till framtiden

Sedan slutet av 2010-talet har det funnits ett nätverk av svenska kärnavfallsaktörer som arbetat med frågor om övervakning och att föra information om kärnavfallsförvar till framtiden. Både SSM och kärnavfallsbolaget SKB ingår i nätverket. Detta arbete nämns inte i avsnittet 4.13.1 om bevarande av information och kunskap genom generationer. Föreningarna menar att nätverket kan vara en viktig del i kunskapsuppbyggnaden inom området och att SSM bör ta ledarskap för nätverket och se till att det får tillgång till resurser.

4. Behov av en omstrukturering av den svenska kärnavfallsforskningen

4.1. Strålsäkerhetsmyndigheten (SSM) måste ta ett nytt grepp om svensk kärnavfallsforskning, inklusive öppenhet och finansiering av från industrin oberoende forskning

Föreningarna har följt den svenska kärnavfallsforskningen sedan 1990-talet. Det finns uppenbara brister i hur forskningen bedrivits av kärnavfallsbolaget SKB. Enligt lagstiftningen har bolaget allt ansvar för att forskning bedrivs, vilket som ovan berörts är problematisk eftersom bolaget inte har intresse av att bedriva en allsidig forskning som kan visa på resultat som är negativa för planerna och verksamheten. Dessutom finna det ingen offentlig insyn som kan granska arbetet.

Föreningarna anser att när regeringen meddelat tillstånd för kärnbränsleförvaret så ger SSM:s tillsynsansvar myndigheten möjlighet att ställa större krav på kärnavfallsbolagets forskning och på att bolaget genomför forskningen med en bättre insyn.

Men detta räcker inte. SSM måste även se till att myndigheten utvecklar den egna forskningsorganisationen och att mycket mer från industrin oberoende forskning görs inom kritiska områden.

[11] Se https://www.deepisolation.com.

4.2. Ett brett svenskt deltagande i europeisk kärnavfallsforskning

En möjlighet för SSM att utveckla myndighetens forskningsengagemang är att se till att möjligheten finns att delta i det europeiska kärnavfallsforsningsprogrammet EURAD[12]. Programmet är på väg in i fas 2 så det är bråttom. Bland annat måste SSM se till att regeringen tar ett beslut om att inte bara kärnavfallsbolaget SKB är en s.k. ”mandated actor” i Sverige.

Inom kärnavfallsområdet är strålsäkerhetsmyndigheterna i världen och dessas forskningsorgan organiserade i organisationen SITEX_Network[13]. Organisationen koordinerar de europeiska medlemmarnas arbete inom EURAD-projektet och SSM bör omedelbart söka medlemskap.

5. Forskning på avfall från nya reaktorer

Enligt kärntekniklagens §11 ska den som har tillstånd till att inneha och driva en kärnkraftsreaktor bedriva den allsidiga forskning som krävs för att se till att de genererade kärnavfallet hanteras och förvaras på ett säkert sätt. Regeringen verkar för att nya reaktorer ska byggas i Sverige. På förslag finns flera reaktortyper som skulle använda bränslen som avsevärt skiljer sig från de som används i nuvarande kärnkraftreaktorer.

Föreningarna menar att det är problematiskt att nya bolag som kan komma att söka tillstånd för att bygga kärnkraftreaktorer i Sverige inte behöver ta fram den kunskap som behövs för kärnavfallshanteringen förrän tillstånd för drift erhålls. SSM bör se över denna fråga och föreslå hur forskningskraven på aktörer som vill bygga ny kärnkraft i Sverige kan skärpas.

Johanna Sandahl
Ordförande, Naturskyddsföreningen

Rikard Rudolfsson
Ordförande, Jordens Vänner

Åsa Lindstrand
Ordförande, MKG

Kontakt för frågor rörande yttrandet:

Johan Swahn
Kanslichef, MKG
Mobil: 070-4673731
E-post: johan.swahn@mkg.se

Oscar Alarik
Chefsjurist, Naturskyddsföreningen
Mobil: 070-611 32 29
E-post: oscar.alarik@naturskyddsforeningen.se

Bilagor:

1. ”Gas phase composition during the unsaturated period: Status report”, Åkesson & Laitinen, SKB Document ID 1983850, 2022-06-10.
2. ”Corrosion of copper in repository-like field tests: Compilation and analysis of data”, J. Johansson, SKB Document ID 1713264, 2019-04-04.
3. ”Penetration of corrosive species into copper exposed to simulated O2-free groundwater by time-of-flight secondary ion mass spectrometry (ToF-SIMS)”, Yue et al., Corrosion Science 210 part 2, January 2023.
4. ”Corrosion-induced microstructure degradation of copper in sulfide-containing simulated anoxic groundwater studied by synchrotron high-energy X-ray diffraction and *ab-initio* density functional theory calculation”, Zhang et al., Corrosion Science, 184, 15 May 2021.

[12] Se https://www.ejp-eurad.eu.
[13] Se https://www.sitex.network.

Document ID
1983850, (1.0 Approved)
Reg no

Security class
Public

Page
1(13)

Document type
Report

Author
2022-06-10 Mattias Åkesson
Heikki Laitinen

Quality assurance
2022-08-19 Mattias Åkesson (RR)
2022-08-29 Lotta Rubio Lind (Approved)

Gas phase composition during the unsaturated period. Status report June 2022.

Contents

1 Introduction

The overall objective of this work is to investigate the evolution of gases in unsaturated bentonites. The consumption of O_2 and the production of H_2S are of particular interest. Investigations of the evolution of gases under such conditions have previously been reported by Birgersson and Goudarzi (2018). Åkesson et al. (2020) presented results from the initial tests performed with an equipment in which the bentonite was subjected to a thermal gradient provided by a centrally placed heater, made of either copper or stainless steel. The results from these latter tests indicated that the rate of oxygen consumption was approximately the same in the two tests, regardless if the heater was made of copper or of stainless steel, and this suggested that the oxygen consumption was caused by processes in the bentonite rather than by oxidation of the metal, which is in direct conflict to the conclusions in Birgersson and Goudarzi (2018). This equipment was subsequently modified in different ways:

i. By developing a new test setup in which the bentonite can be placed inside a gastight glass container, which in turn is placed in a temperature chamber. This means that the gas composition evolution can be investigated in the absence of any metals and with isothermal conditions.
ii. By installation of condensation traps, which can prevent the hot vapour from entering the gas analysis system.
iii. By expanding the measuring ranges for some of the gas sensors, especially for the H_2-sensor which was found to be too narrow in the initial tests.
iv. By using a bentonite with a higher content of sulphur. This will the enhance the prospects of quantifying gases formed as a result of oxidation or dissolution of pyrite.

A new test programme, described in the activity plan AP RD LERMTRL-20-018, was launched in the beginning of 2021. This status report presents the main results obtained within the framework of this activity plan during the first 18 months of measurements.

2 Materials and methods

2.1 Test equipment

Two sets of test equipment have been used in this work: i) a setup with a *thermal gradient* and a copper heater surrounded by bentonite, which in turn was installed in a stainless-steel container, and ii) the new *isothermal* setup with a glass container in a heating cabinet. The first set (***Figure 2-1***) was identical the one used for the initial tests (see Åkesson et al. 2020) apart from the actual heating mechanism, which was changed from a system with circulating oil to an electrical heating coil installed inside the copper heater, and the construction of a perforated cage which can be placed on top of the heater which means that fairly fine-grained bentonite material can be installed directly (thereby avoiding any block compaction). The second set consisted of a two-parted glass desiccator with a two-hole rubber stopper in the upper part, through which two gas sampling glass tubes were connected and led down into the container (***Figure 2-2***). Each set was connected to a condensation trap; with the copper heater setup the condensate can be led back to the container, whereas for the glass container setup the condensate has to be collected. The entire test system with test setups, condensation traps and the gas analysis system, connected with a number of valves, is illustrated in ***Figure 2-3***.

The gas analysis system was supplied by OmniProcess AB and was designed to measure the concentration of the following gases: oxygen (O_2), carbon dioxide (CO_2), hydrogen (H_2), hydrogen sulphide (H_2S) and sulphur dioxide (SO_2). A compilation of manufacturers, names, methods, measuring intervals and required flow rates is shown in Table 2-1. The original measuring range of the H_2-sensor was 0 -150 ppm. This has subsequently been expanded to 0 – 1000 ppm. The

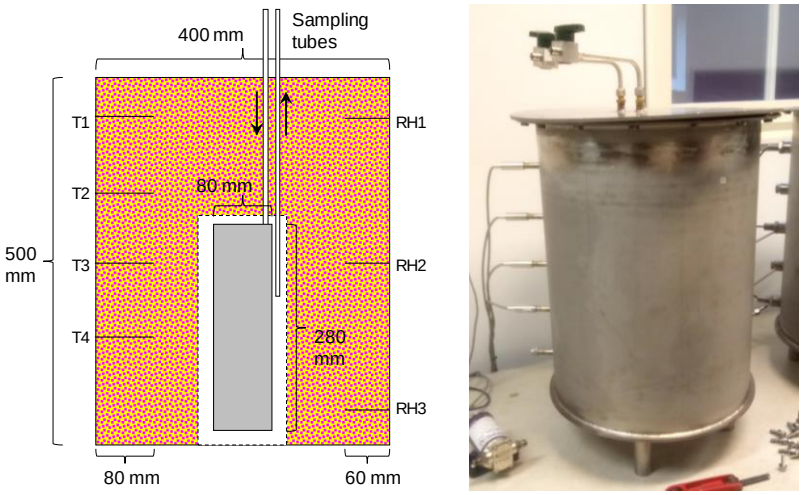

***Figure 2-1**. Test container with copper heater. Schematic section drawing with marked location of temperature and relative humidity sensors (left).*

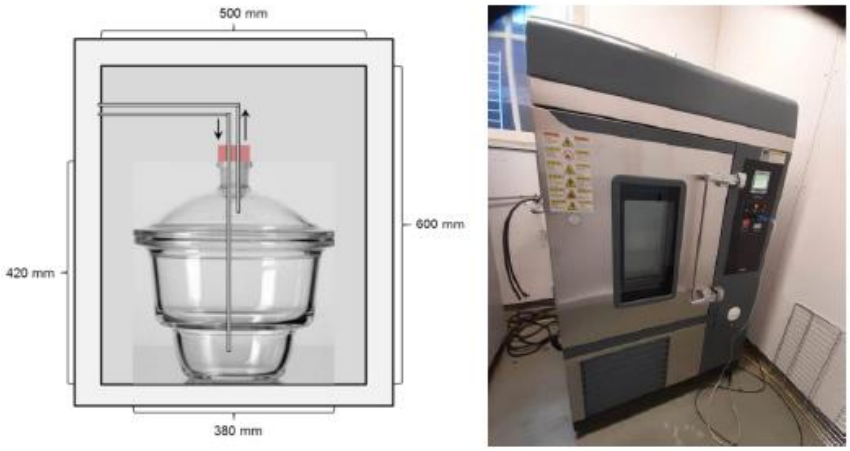

***Figure 2-2**. Glass container (left) in heating cabinet (right).*

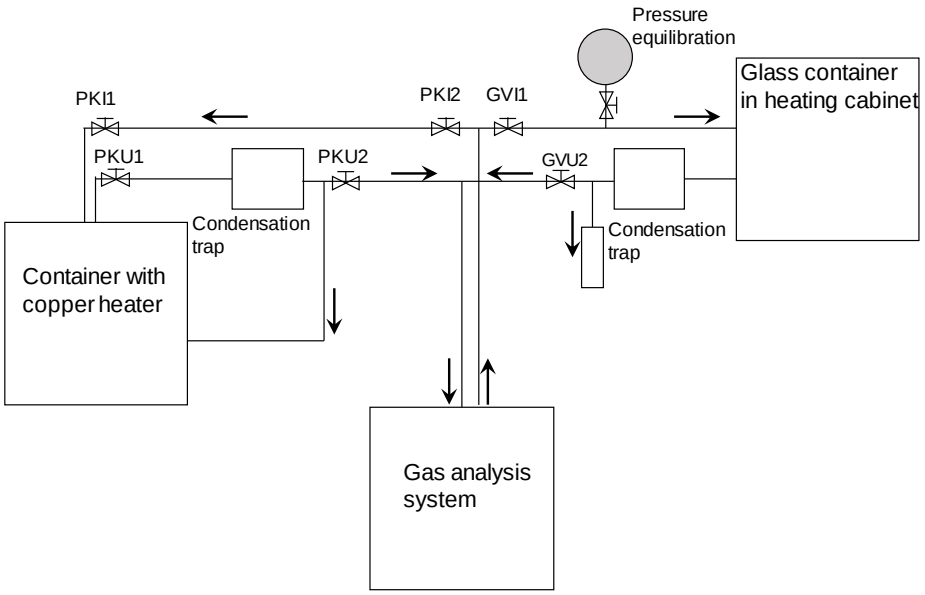

***Figure** 2-3**. Schematic flow scheme over test equipment and gas analysis system.*

measuring range of the CO_2 sensor was also expanded during the preparation for this work; from 0 – 1000 ppm to 0 – 20 %.

Sensor validation
Calibration gases were procured in order to obtain an independent validation of the different sensors. Three gas mixtures in separate tubes were obtained from Air Liquide Gas AB:

- CO_2 (10%) and H_2 (500 ppm) mixed in N_2
- H_2S (5 ppm) mixed in N_2
- SO_2 (0.5 ppm) mixed in N_2

All of these gases could be used through the calibration inlet of the gas analysis system so that the pump determines the flow rate through the different sensors. However, due to the pump in the SO_2-sensor, this had to be tested separately (see ***Figure*** 2-4). No special gas was obtained for O_2, since a well-defined concentration is provided by air. The results from these tests are compiled in Table 2-2. It can be noted that the results for the CO_2, H_2S and SO_2 sensors are in fairly well agreement with, and are generally within 10 %, from the concentration of the calibration gases. The results from the H_2-sensor suggest that the measured concentration underestimates the actual concentration with a factor of 2. The data from this sensor should therefore be regarded as quite uncertain.

Table 2-1. **Compilation of instruments and their characteristics**

Gas	Manufacturer	Instrument	Method	Measuring interval	Flow rate (l/min)
O_2	Servomex	Multiexact 4100	Paramagnetic cell	0 – 25 %	0.1
CO_2	Vaisala	GMP343	NDIR infrared cell	0 – 20 %	0.1
H_2	Compur	Statox 501	Electrochemical cell	0 – 1000 ppm	0.1
H_2S	Servomex	SERVOTOUGH Laserexact	Laser	0 – 10 ppm	2
SO_2	ThermoFisher SCIENTIFIC	iQ Series 43	Pulsated UV fluorescence	0 – 1 ppm	0.5

Table 2-2. Results from sensor validation tests

Gas component	Calibration gas concentration	Measured value
CO_2	10 %	8.76 %
H_2	500 ppm	245 ppm
H_2S	5 ppm	4.6 ppm
SO_2	0.5 ppm	549 ppb

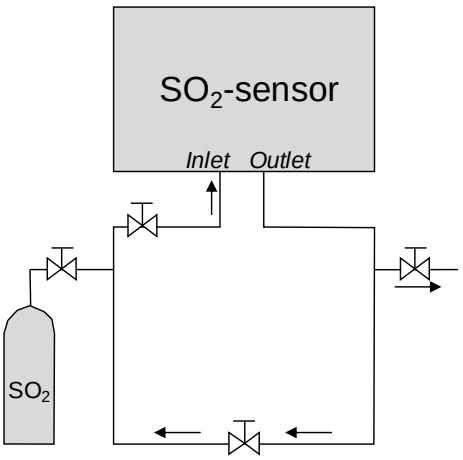

Figure 2-4**.** *Schematic flow scheme for validation of SO_2-sensor.*

2.2 Bentonite

The used bentonite comes from Milos and was provided by Imerys in Greece. The material (designated E8789) was processed in Germany. The characteristic of the delivered material, which was based on data from the supplier, is shown in Table 2-3. The material was also analysed within a characterization program at SKB (AP RD LERMTRL-20-014). This showed that the material exhibits a Tot/S content of approximately 0.9 % out of which approximately 1/3 is found as sulphide. In addition, the content of inorganic carbon was found to be about 3.5 % (as CO_2).

Table 2-3. Material specification of used bentonite provided by Imerys

Particle size	0.5 - 5.0 mm
Water content	13%
Montmorillonite content	65-75 %
Sulphur	~0.8%
Semi-activated	~30% Ca: 70% Na

2.3 Test matrix

Ten tests have been performed within this test program since the beginning, and a compilation of all tests with installed bentonite bulk mass, water content, operation temperature and test period are given in Table 2-4. The one test performed in the test container with copper heater was denoted PK_1. The remaining nine tests performed in the glass container in the heating cabinet were denoted GV_1 to GV_9. One goal of the GV tests was to investigate the influence of temperature and bentonite water content on the evolution of gas composition in general and the consumption of O_2 in particular. Whereas an analysis of the influence of the temperature has been achieved (see section 4.1), a corresponding analysis for the water content remains to be done. The results from the first two GV tests are not included in this report due to the extensive intrusion of air observed in these tests (see next section).

Table 2-4. Bentonite mass and test conditions applied in different tests

Test	Bulk mass (kg)	Water content (%)	Temperature (°C)	Test period	Remarks
PK_1	63.29	13.3	90*	210423-210618	-
GV_1	18.43	12.4	70	210224-210423	Not included here
GV_2	20.63	18.5	70	210423-210601	Not included here
GV_3	20.80	16.9	70	210601-210618	-
GV_4	20.98	16.7	70	210831-210928	-
GV_5	20.45	16.8	55	210929-211110	-
GV_6	21.09	15.9	55	211110-211216	-
GV_7	18.68	13.4	70	220120-220301	-
GV_8	19.94	14.7	70	220302-220405	-
GV_9	20.99	15.7	40	220405-220609	-

* Heater temperature

2.4 Development and challenges

Two major challenges have been encountered during the course of the work with this test programme.

The H_2-sensor

The expansion of the measuring range of the H_2-sensor was more complicated than initially thought, and this meant that this sensor had to be re-build by the manufacturer, and could therefore not be used during the first four tests (PK_1 and GV_1 through GV_3). After this modification, it was also noticed that the sensor had a recommended flow rate (0.3-0.4 L/min) which exceeded the

flow rate provided by the gas analysis system to the H_2-sensor (0.1 L/min), and results obtained from this are therefore thought to be underestimated (Table 2-2).

Leakages

During the first tests performed with the desiccator (GV_1 to GV_3) it was found that these were significantly affected by air intrusion, especially during measurements. The cooling of the extracted gas during such events could possibly lead to a gas pressure reduction, which in turn would lead to an inflow of air into the container. As a countermeasure, a gas pressure equilibration component (i.e. a balloon) was installed on the incoming tube to the glass container in May 2021. With this, it should be possible to contain the expansion of the gas caused by the initial heating of the test equipment, and also to have a surplus of gas volume which can be tapped during the measurements. A more significant improvement regarding the tightness was achieved by applying vacuum grease to the flanges in all such tests from the GV_4 tests and onward. However, also after this modification some minor, albeit significant, air intrusion was noticeable. A leakage search was therefore performed on October 29th 2021 (i.e. during the GV_5 test) with a Nordtec Testo 316-2 instrument, and by supplying a calibration gas with 500 ppm H_2 (see below) to the system. Two leaks were found during this search: i) a broken plastic T-coupling inside the O_2-sensor, which was replaced; and ii) the attachment/inlet to the H_2-sensor. The modification of the O_2-sensor seems to have been affected the calibration of this sensor, since O_2-depleted conditions have yielded results as low as -2 %. All O_2-results from test GV_6 and onwards have therefore been shifted +2%. The leakage point at the H_2-sensor has been remediated through grease application. However, it has been found to be difficult to seal this point completely.

3 Results

3.1 Gas evolutions in tests in glass container

Measured gas evolutions for four tests performed at 70 °C (GV_3, GV_4, GV_7 and GV_8) are shown in ***Figure*** 3-1. The water content of the bentonite installed in GV_3 and GV_4 was 2-3 %-units higher than in GV_7 and GV_8 (see Table 2-3). The first of these tests (GV_3) was affected by air intrusion after the first week, and to some minor extent also the other three tests were affected. Some general trends from these test results can nevertheless be identified:

- In GV_3, the O_2 decreased from typical air concentration to 10 % during the first 3 days. In the other three tests the O_2 decreased to low levels, close to 0%, in approximately 7 to 10 days.
- In GV_4, GV_7 and GV_8, the CO_2 and H_2S increased during the first two weeks to fairly stable levels, with 11-13 % CO_2 and 11-14 ppm (H_2S), respectively. The last CO_2 and H_2S concentrations in the GV_3 were also found in these intervals.
- The SO_2 increased during the first two weeks to approximately 900-1200 ppb. In GV_4 and GV_8, this concentration was reduced to approximately half that level during the subsequent two weeks.
- The H_2 increased during the first week to 200 - 700 ppm, after which it was reduced with a factor of 3 or more during the subsequent three weeks. It can be noted that maximum value in the GV_4 test was more than twice as high as in the GV_7 and GV_8 tests. This shift was probably caused by an attempt to calibrate the H_2-sensor during the GV_5 test.

Measured gas evolutions from two tests performed at 55 °C (GV_5 and GV_6), and one test performed at 40 °C (GV_9), are shown in ***Figure*** 3-2. The first of these (GV_5) was affected by air intrusion and it was during this test that a leakage search was conducted and the broken T-

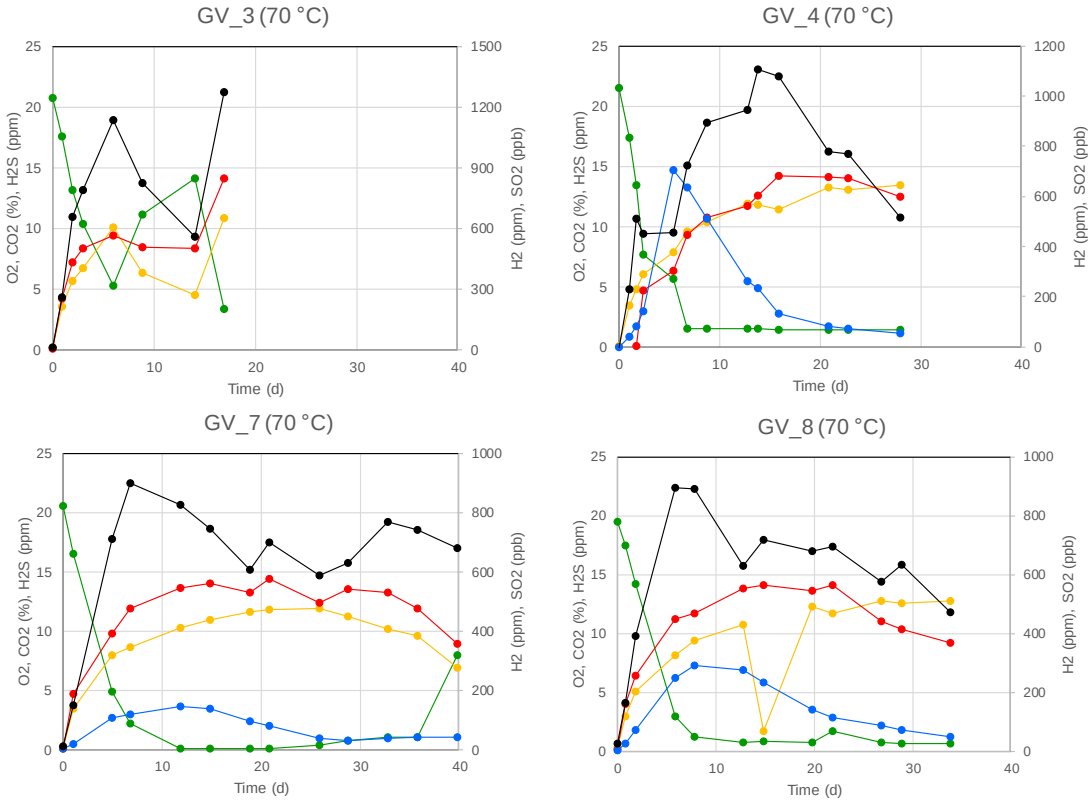

Figure 3-1. *Test results for four tests in glass desiccator at 70 °C. O_2 (green), CO_2 (orange), H_2S (red), H_2 (blue) and SO_2 (black). The O_2 data has been shifted +2% for test GV_7 and GV_8.*

coupling inside the O_2-sensor was replaced. The significant air intrusion observed after five weeks was caused by the human factor and an open valve.

The results from the second test performed at 55 °C (GV_6) indicate that the test system was more gas tight than in the previous test. The decreasing O_2 trend during the first two weeks indicates that the rate of oxygen consumption was quite constant with approximately 1 % unit per day. After this the O_2 concentration displayed a more asymptotic decreasing trend and never fell below 3 % during the measurements. In parallel to this, the concentration of the other gas components increases to fairly constant levels; CO_2: 4 %, H_2S: 5 ppm, H_2: 200 ppm, and SO_2: 600 ppb.

The results from the test performed at 40 °C (GV_9) also indicate that the test system was fairly gas tight. In this case the overall rate of O_2 consumption was approximately 0.05 % per day. However, the oxygen reduction between some consecutive measurements was almost twice as high, and this indicates that a minor air intrusion did occur during each measurement. In this test, the concentration of CO_2 increased to 0.8 %, H_2 to 60 ppm, SO_2 to 130 ppb, whereas H_2S was below 1 ppm.

Apart from the measurements performed with the gas analysis system, the acquirement of the leakage detector mentioned above has also enabled qualitative measurements of CH_4 by inserting the sensor head of the instrument into the glass container at the time of dismantling. Such measurements have been performed on several tests from the GV_4 test and onward, and indicate a significant concentration (>1%) of CH_4.

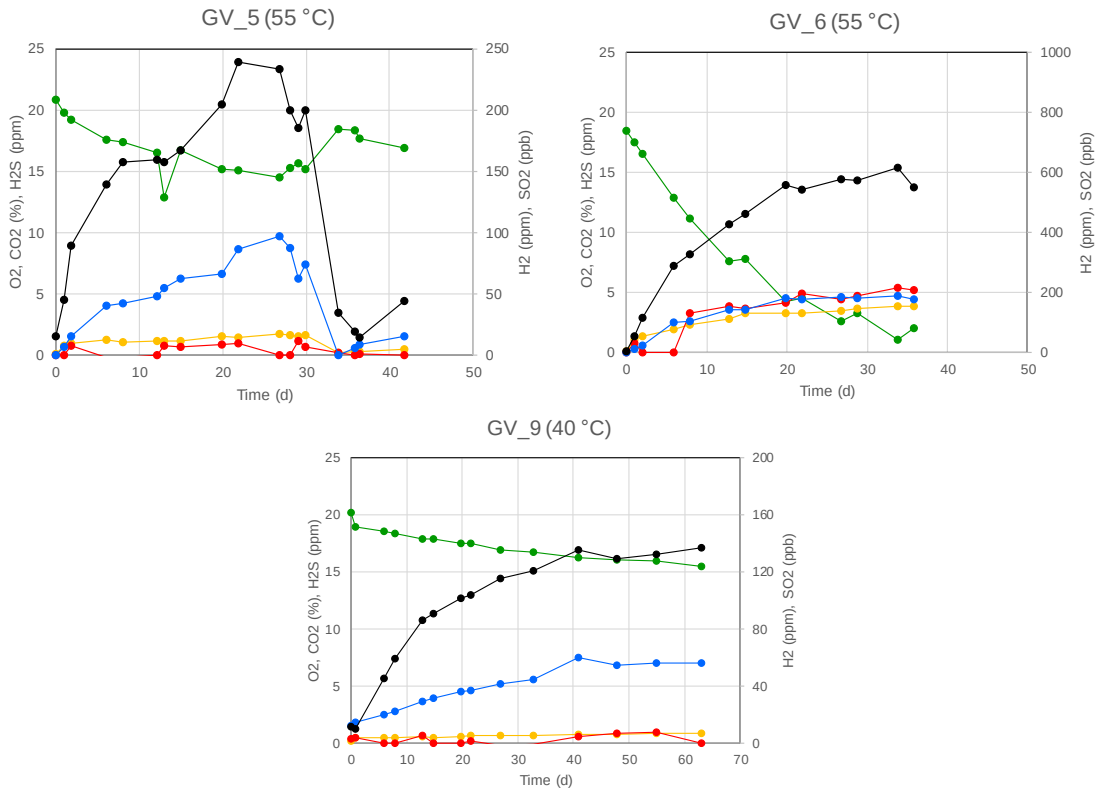

Figure 3-2. *Test results for tests in glass desiccator at 55 and 40 °C, respectively. O_2 (green), CO_2 (orange), H_2S (red), H_2 (blue) and SO_2 (black). The O_2 data has been shifted +2 % for test GV_6 and GV_9.*

3.2 PK_1 test in container with copper heater

Evolutions of measured gas components, temperature and relative humidity in the PK_1 test are shown in ***Figure*** 3-3. The temperatures measured at different heights and at 80 mm distance from the container wall (***Figure 2-1***) were generally found within the interval 30 to 40 °C. Similarly, the relative humidity values measured at 60 mm from the wall, were generally found within the interval 70 to 80 %. The rate of O_2 consumption was quite modest and the O_2 concentration never fell below 17 % during the eight-week test period. This appears to some extend to be caused by air intrusion, e.g. after the first week when the O_2 concentration increased, and the SO_2 and CO_2 concentrations decreased from 140 to 20 ppb, and from 1.1 to 0.5 %, respectively. However, it can be noted that the overall temperature level in the bentonite around the heater was quite low (***Figure*** 3-3, lower left), and the conditions in this test therefore appears to resemble those in the GV_9 test (with 40 °C) most closely among the tests performed in glass container. The test system appears to have been more gas tight during the last few measurements of the test, since the O_2 concentrations again decreased while the SO_2 and CO_2 concentrations increased. Finally, the water content distribution was measured at the end of the test (***Figure*** 3-3, lower right), and this showed that a noticeable moisture redistribution had occurred due to the thermal gradients in the bentonite.

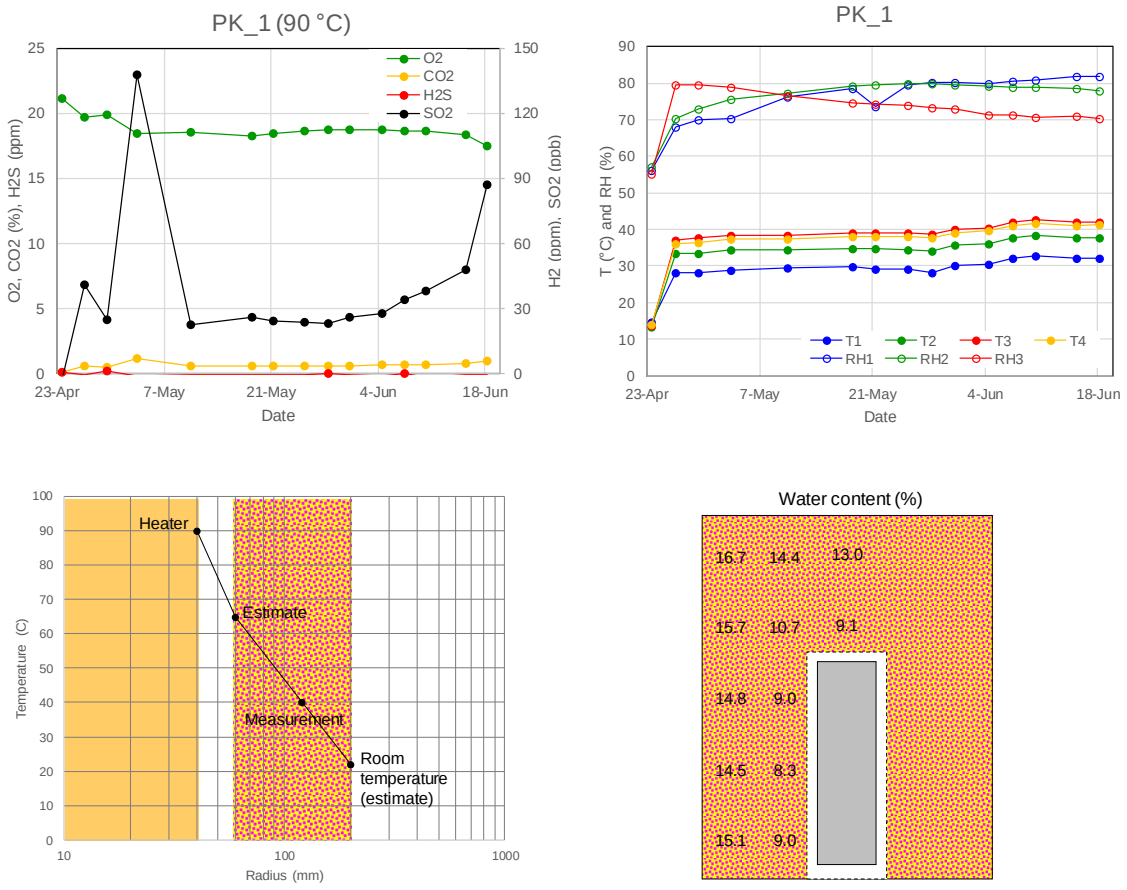

Figure 3-3. *Test results for test PK_1 in container with copper heater. Evolution of gas components (upper left) and temperature and relative humidity; sensor positions according to Figure 2-1 (upper right). An evaluation of the temperature profile at heater mid-height (lower left). Water content distribution at the end of the test (lower right).*

4 Evaluations

4.1 Temperature dependence of the rate of O_2 consumption

The temperature dependence of the rate of O_2 consumption was evaluated from data measured during the initial phase of five of the tests performed in glass container. Two of these were performed at 70 °C (GV_3 and GV_4); two at 50°C (GV_5 and GV_6); and one at 40°C (GV_9). Two additional tests performed at 70°C (GV_7 and GV_8) could also have been addressed, but the water content in these tests were slightly lower than in the other tests (Table 2-4) and therefore not included in this evaluation. Still, for comparisons, the data from these two tests are included in ***Figure*** 4-1 below.

The oxygen consumption rates used in the evaluation was simply defined as the concentration decrease per unit time (i.e. %/day). This was deemed to be sufficiently detailed, since the bulk mass and the water content in the different tests were quite similar. The evolution of O_2 consumption was simply evaluated as the difference between the first and the subsequent measurements for each test (between the second and subsequent measurements in GV_9 due to the marked initial concentration drop in this test). From these evolutions, the following consumption rates were evaluated: 4.5, 1 and 0.1 %/day for 70, 55 and 40 °C, respectively (***Figure*** 4-1, upper row). By plotting the logarithm of these consumption rates versus the inverse of the absolute temperature (***Figure*** 4-1, lower left), an activation energy of approximately 0.11 MJ/mol can be evaluated. A comparison of an exponential temperature dependence with this activation energy and the evaluated consumptions rates is shown in ***Figure*** 4-1 (lower right).

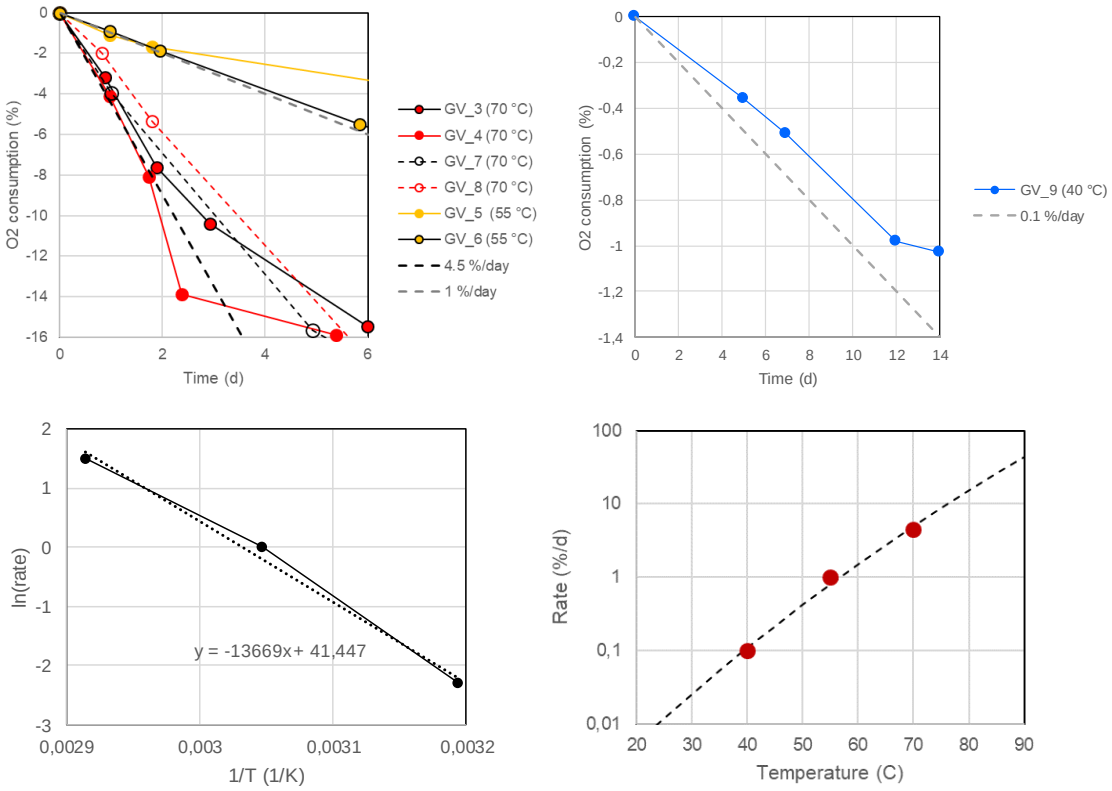

Figure 4-1. *Evaluation of temperature dependence of the rate of oxygen consumption in tests in glass containers. Evolution of O2 consumption in five tests (upper row). Arrhenius plot (lower left) and exponential temperature dependence together with measure consumptions rates (lower left).*

4.2 Tentative conceptual model

Since there are no metals in the glass container, and since a clear generation of SO_2 can be measured, it appears to be quite evident that oxygen is consumed through pyrite oxidation. This process probably occurs in the presence in water, since the O_2 concentration reduction exceeds by far the concentration of SO_2. The formation of CO_2 indicates the dissolution of calcite. This process requires the formation of H^+, which in turn also indicates pyrite oxidation in the presence of water. Pyrite oxidation does not lead to the formation of H_2S, if the sulphur is oxidized. Pyrite dissolution could therefore be the source of H_2S (see King 2013). The formation of methane, as qualitatively measured with the leakage detector, can tentatively originate from either degradation of organic material, or through hydrogenotrophic methanogenesis.

A simple mass balance calculation shows that the amounts of pyrite and calcite in the bentonite are sufficient to explain the complete consumption of all O_2 and the generation of all observed CO_2. Installed amounts of bentonite, water and air in one the glass container tests are shown in Table *4-1*. The initial amounts of O_2 in the gas phase and sulphide-S in the bentonite can then be calculated as:

- $n_{O2}=C_{O2} \cdot V_G \cdot / V_m = 21\ \% \cdot 12.7$ litre / 24 litre/mol = 0.11 mol
- $n_S = x_S \cdot m_d / M_S = 0.003$ kg/kg $\cdot 17.8$ kg / 0.032 kg/mol= 1.7 mol

By the same token, the final amount of CO_2 in the gas phase and the initial amount of inorganic carbon in the bentonite can be calculated as:

- $n_{CO2,gas} = C_{CO2} \cdot V_G \cdot / V_m = 10\ \% \cdot 12.7$ litre / 24 litre/mol = 0.05 mol
- $n_{CO2,bentonite} = x_{CO2} \cdot m_d / M_{CO2} = 0.035$ kg/kg $\cdot 17.8$ kg / 0.044 kg/mol= 14 mol

This clearly shows that the amount of sulphide-S in the bentonite is sufficient to consume all the O_2 in the gas phase, and that the initial amount of inorganic carbon far exceeds the amount of CO_2 in the gas phase at the end of the test.

The unsaturated bentonite can generally be considered to be composed of three phases: solid, liquid and gas phase. Whereas the gas phase can be assumed to be fairly homogenous, the other two are probably quite heterogenous. Due to the hydroscopic properties of the montmorillonite, it can be assumed that the dominant part of the liquid phase is absorbed in the montmorillonite, and that only a small fraction of this phase is attached with the accessory minerals (***Figure 4-2***). This means that the water volume where the chemical reactions take place may be much smaller than the gas volume.

Table 4-1. Specification of material and phases in glass container setup (test GV_3)

Bentonite mass	20.8 kg
Volume (lower part)	17.4 litre
Water content	16.9 %
Density (bulk)	1195 kg/m3
Density (dry)	1023 kg/m3
Density (solid)	2750 kg/m3*
Void ratio (e)	1.69 (-)
Porosity (n)	0.63 (-)
Degree of saturation (S)	0.28 (-)
n*(1-S)	0.46 (-)
Gas volume (lower part)	7.9 litre
Gas volume (upper part)	4.8 litre
Gas volume (total)	12.7 litre
Water volume	3.0 litre

* Adopted from Karnland et al. (2006)

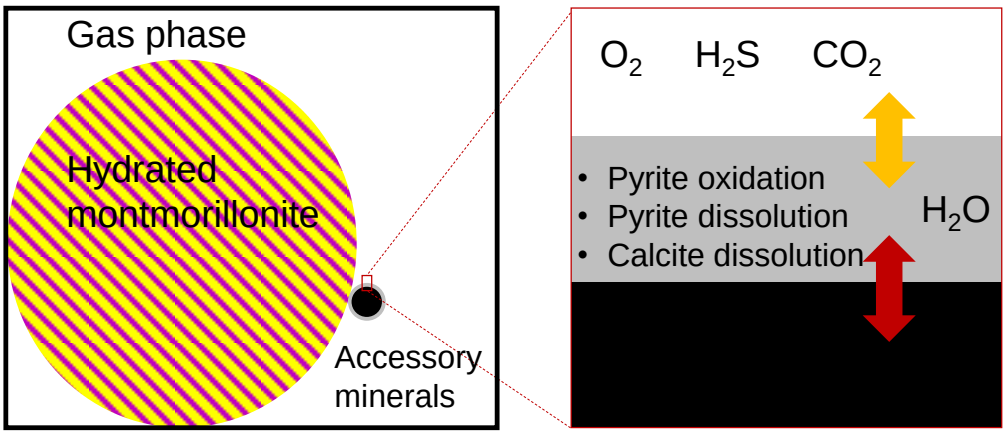

***Figure 4-2**. Tentative description of the site of the reactions of interest.*

5 Future work

This status report has presented results obtained within the framework of the activity plan AP RD LERMTRL-20-018 during the first 18 months of measurements. A number of measures and modifications could or should be addressed during the continuation of this work.

- *Service and calibration of sensors.* The CO_2-sensor should be sent to the manufacturer (Vaisala), whereas all other sensors should be subject for maintenance by the supplier (OmniProcess).
- *Modified flow rate through H_2 sensor*. The designed flow rate through the H_2 sensor (0.1 L/min) is currently not optimal for the sensor (0.3-0.4 L/min). This could possibly be rectified by installation of a new valve. It would also be advantageous if the attachment/inlet to the H_2-sensor could be sealed completely.
- *New sensors*. Tests with the leak sensor at the dismantling of some of the tests indicates that there was a noticeable formation of CH_4 in these tests. In order to obtain more detailed and reliable data on such a formation, it is proposed that that the gas analysis system is complemented with a CH_4 sensor.
- *Other analyses.* It would be beneficial if the interpretation of the measured evolution of gases could be supported by other types of analyses, e.g. pH which tentatively can be measured with a universal pH indicator after dispersion of the material in a solid:liquid ratio of 1:3 (Olsson et al. 2013).
- *Smaller glass container*. The amount of bentonite required for each test could be reduced by replacing the current glass container with a smaller one.
- *Influence of bentonite water content.* Tests with significantly higher, and perhaps lower, water content should be performed in order to investigate the influence of this parameter.
- *Other materials.* It would be interesting to tests the methodology on other material. Not only on other bentonites such at MX-80, but also on “pure” pyrite. It would also be advantageous to perform at least one control test with an empty air-filled glass container.
- *Modification of equipment test container with copper heater*. The PK_1 test demonstrated that the temperature in the bentonite in this test was relatively low. The design of this equipment should therefore be modified, first and foremost by installation of thermal insulation on the outer surfaces of the test container. Secondly, if possible, the diameter of the perforated cage around the heater should be reduced.

References

SKB's (Svensk Kärnbränslehantering AB) publications can be found at www.skb.com/publications.

Birgersson M, Goudarzi R, 2018. Investigations of gas evolution in an unsaturated KBS-3 repository. SKB TR-18-11, Svensk Kärnbränslehantering AB.

Karnland O, Olsson S, Nilsson U, 2006. Mineralogy and sealing properties of various bentonites and smectite-rich clay materials. SKB TR-06-30, Svensk Kärnbränslehantering AB.

King F, 2013. A review of the properties of pyrite and the implications for corrosion of the copper canister. SKB TR-13-19, Svensk Kärnbränslehantering AB.

Olsson S, Jensen V, Johannesson L-E, Hansen E, Karnland O, Kumpulainen S, Svensson D, Hansen S, Lindén J, 2013. Prototype Repository. Hydromechanical, chemical and mineralogical characterization of the buffer and backfill material from the outer section of the Prototype Repository. SKB TR-13-21, Svensk Kärnbränslehantering AB.

Åkesson M, Svensson D, Laitinen H, 2020. Gas phase composition during the unsaturated period. Initial tests. SKB P-20-23, Svensk Kärnbränslehantering AB.

DokumentID
1713264, (1.0 Godkänt)
Reg nr

Sekretess
Öppen
Dokumenttyp
Memo

Sida
1(20)

Författare
2019-04-04 Johannes Johansson

Corrosion of copper in repository-like field tests: compilation and analysis of data

Content

1 Introduction

Field tests of repository-like installations offer the possibility to study the integrated development of the engineered barrier system on different time scales. The strength of field tests is that they can be set up to illustrate a realistic initial development of a KBS-3 repository, which can be used for example to validate models and the conceptual understanding of the development of the system. On the other hand, field tests have a at least two weaknesses in that 1) the establishment of long-time reducing and sulfidic conditions at the canister-bentonite interface might take years if the bentonite barrier is dense and thick enough, and 2) parameter control is difficult to achieve without disturbing the system's natural development. For these reasons, the detailed mechanistic understanding of the development of the corrosion process must be approached using controlled laboratory experiments and theoretical modeling. SKB and other waste management organizations have conducted a number of field tests of the KBS-3 barrier system from which data have been obtained and conceptual understanding can be gained. In this Memo, the outcome of these field tests, with focus on the corrosion data gathered, will be analyzed and discussed.

In the corrosion model applied in SKB's safety assessments for a KBS-3 repository at the Forsmark site, the initial corrosion of copper is due to residual oxygen from the air saturated bentonite porosity and air-filled macroscopic voids in the near field, for example the gap present initially between the bentonite blocks and the copper canister. When the residual oxygen has been consumed by corrosion of copper and other oxidation processes in the near field, gamma radiolysis of water continues to cause some further corrosion of the canister until the sulfidic ground water has saturated the bentonite clay and transport-controlled corrosion by sulfide continues (King et al. 2013, 2017). Since the concentration of sulfide in the ground water is low, and since diffusion through the bentonite is slow, the residual oxygen present from the start dominates the corrosion observed in typical field tests.

In this Memo, four of SKB's field tests performed at the Äspö Hard Rock Laboratory (HRL) will be described, including the experimental configurations, the initial conditions of the tests and what is known about the development of the redox conditions. A field test performed by Enresa (Spain) and NAGRA (Switzerland) at the Grimsel test-site in Switzerland will also be described since copper corrosion data was available for comparison. The corrosion observed visually and spectroscopically in these field tests will be reviewed and it is discussed how the observations may be understood from the initial state and development of the redox conditions. The available test data, such as residual oxygen, temperature, and exposure time, will be analyzed to see what conclusions can be drawn and which parameters control the corrosion depth in these tests. The overall aim of this Memo is to examine how the corrosion model applied in SKB's safety assessments corresponds with the early development of corrosion observed in these field tests.

2 Description of the experiments

The following field tests performed at the Äspö HRL, will be described and discussed herein: Prototype Repository (PR), Long-term test of buffer materials (LOT), Alternative Buffer Materials (ABM), and In situ corrosion test of miniature canisters (MiniCan). Reference will also be made to the Full-scale Engineered Barrier Experiment in Crystalline Host Rock (Febex), performed by Enresa and NAGRA at the Grimsel site.

2.1 Prototype repository (PR)

The full scale field experiment Prototype Repository (PR) represents the initial phase and early environmental development of a future KBS-3 repository. The canisters are five meters high and consist of a five cm thick copper shell and a cast iron insert, which is the reference canister design. The copper shell was made of SKB's reference material, oxygen-free phosphorous doped copper

(Cu-OFP). The installation consists of a horizontal tunnel at 450 m depth, in which six copper canisters have been emplaced in vertical deposition holes. The deposition holes are eight meters deep and just less than two meters in diameter. The canisters are surrounded by 35 cm thick bentonite rings and cylindrical bentonite blocks fill the top and bottom of a deposition hole, see Figure 1. The horizontal tunnel was divided into an inner and an outer section, containing four (PR1-PR4) and two canisters (PR5 and PR6), respectively (Figure 1). Each section was backfilled with bentonite clay and sealed with a concrete plug, the inner section in 2001 and the outer in 2003. In 2011 the outer section of the experiment was opened and the canisters PR5 and PR6 were retrieved and analysed after eight years of exposure in the Äspö HRL. Further details of the experimental configuration of PR can be found in Svemar et al. (2016).

In order to simulate the thermal effect of the encapsulated spent nuclear fuel, the canisters were equipped with heaters, started shortly after installation. The aim of PR was to study the behaviour of the integrated rock-bentonite-canister system with primary focus on the bentonite buffer. Therefore, the experiment is not optimal for studying copper corrosion; the initial state of the canister surfaces was not characterised, and there were no mass-loss specimens mounted in the clay. However, electrochemical monitoring of corrosion rates was performed on cylindrical copper electrodes installed in bentonite blocks above the canisters in PR1 (block C3) and PR5 (block C4). Technical details of these measurements are given in Rosborg (2013a).

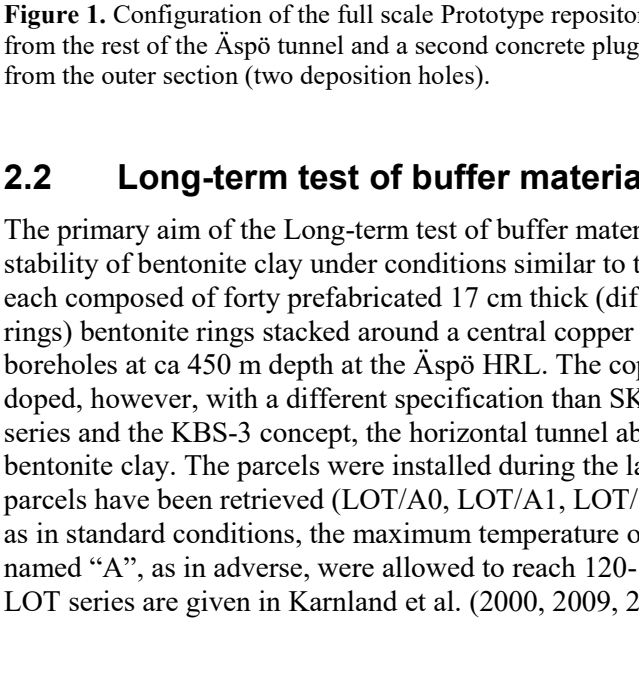

Figure 1. Configuration of the full scale Prototype repository. Initially, a concrete plug sealed the experiment from the rest of the Äspö tunnel and a second concrete plug divided the inner section (four deposition holes) from the outer section (two deposition holes).

2.2 Long-term test of buffer material (LOT)

The primary aim of the Long-term test of buffer material (LOT) was to study the mineralogical stability of bentonite clay under conditions similar to those in a KBS-3 repository. Seven test parcels, each composed of forty prefabricated 17 cm thick (difference between outer and inner diameter of the rings) bentonite rings stacked around a central copper tube, were deposited in 4 m deep vertical boreholes at ca 450 m depth at the Äspö HRL. The copper quality was oxygen-free and phosphorous doped, however, with a different specification than SKB's reference material. In contrast to the PR series and the KBS-3 concept, the horizontal tunnel above the LOT boreholes was not backfilled with bentonite clay. The parcels were installed during the late 1990's and to date (April, 2019) four test parcels have been retrieved (LOT/A0, LOT/A1, LOT/S1, and LOT/A2). In the packages named "S", as in standard conditions, the maximum temperature of the heaters were 90 °C, while the packages named "A", as in adverse, were allowed to reach 120-150 °C during the test. Further details of the LOT series are given in Karnland et al. (2000, 2009, 2011).

In order to quantify the extent of copper corrosion, each of the test parcels contains copper coupons of accurately known initial weights in bentonite rings 22 and 30 (Figure 2). In addition, a set of three cylindrical copper electrodes were installed in bentonite ring 36 of test parcel A2, which allows real-time electrochemical monitoring of corrosion (Rosborg et al. 2004, Rosborg 2013a). As for the PR test series, the copper tubes in LOT were equipped with internal 2 kW heaters to simulate the thermal effect of the spent nuclear fuel. Since mineralogical transformations can be sensitive to temperature variations, the distribution of the thermal field in the bentonite clay was monitored during exposure, which allows specification of the temperatures at the positions of the copper coupons.

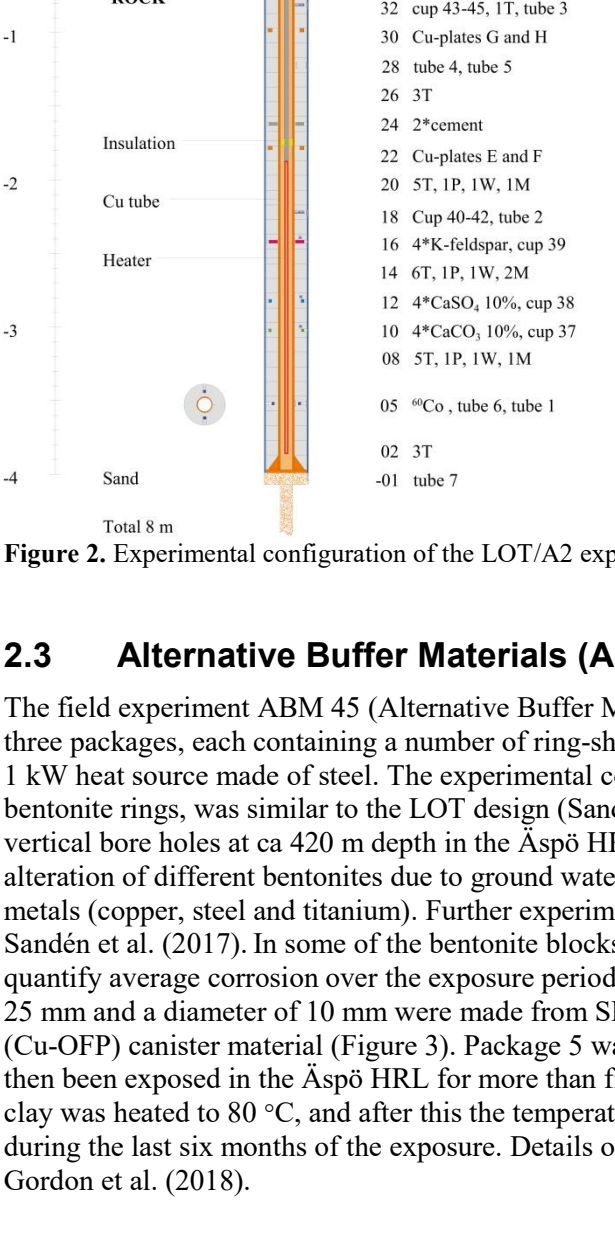

Figure 2. Experimental configuration of the LOT/A2 experiment.

2.3 Alternative Buffer Materials (ABM)

The field experiment ABM 45 (Alternative Buffer Materials package 4, 5, and 6) consisted initially of three packages, each containing a number of ring-shaped bentonite blocks stacked around a cylindrical 1 kW heat source made of steel. The experimental configuration, e.g. the diameter and thickness of the bentonite rings, was similar to the LOT design (Sandén et al. 2017). The packages were installed in vertical bore holes at ca 420 m depth in the Äspö HRL and the aim of the test was to study the alteration of different bentonites due to ground water saturation, heating and interaction with corroding metals (copper, steel and titanium). Further experimental details of the ABM series can be found in Sandén et al. (2017). In some of the bentonite blocks, copper specimens were installed with the aim to quantify average corrosion over the exposure period. Cylindrical copper specimens with a height of 25 mm and a diameter of 10 mm were made from SKB's oxygen-free phosphorous doped copper (Cu-OFP) canister material (Figure 3). Package 5 was retrieved during the autumn of 2017 and had by then been exposed in the Äspö HRL for more than five years. For the first four and a half years, the clay was heated to 80 °C, and after this the temperature was increased to between 150 and 250 °C during the last six months of the exposure. Details of the corrosion examination can be found in Gordon et al. (2018).

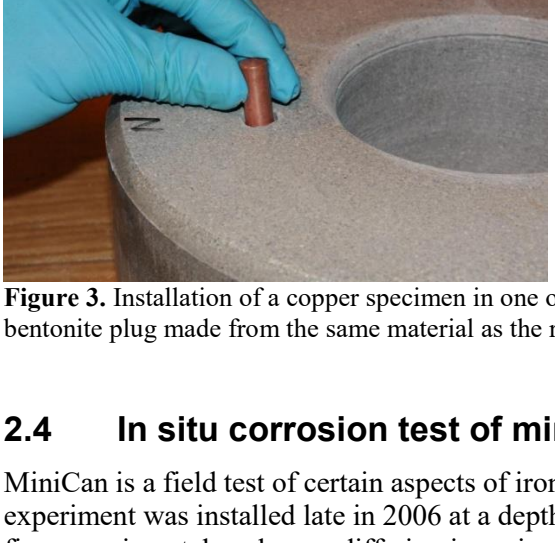

Figure 3. Installation of a copper specimen in one of the bentonite rings in ABM. The hole was sealed with a bentonite plug made from the same material as the ring.

2.4 In situ corrosion test of miniature canisters (MiniCan)

MiniCan is a field test of certain aspects of iron and copper corrosion in a KBS-3 type repository. The experiment was installed late in 2006 at a depth of 450 m in the Äspö HRL. Initially the test contained five experimental packages, differing in various ways but most importantly regarding the presence and density of the bentonite clay surrounding the miniature copper-cast iron canisters (Smart and Rance 2009). In the MiniCan experiment, the copper-cast iron canisters were mounted inside stainless steel cages, which held the bentonite clay in place in the nearly horizontal bore holes that were filled with ground water. This is in contrast to the design of the KBS-3 repository, in which the copper-cast iron canisters will be installed directly in the boreholes with high density bentonite clay filling the space between canister and rock.

In the MiniCan packages 1-3, the canisters were surrounded by low density (1300 kg/m^3 dry density) bentonite made from pellets, spatially separated from the canister by an inner steel cage and a sintered steel filter with 10 µm pores. The clay was thus not in direct contact with the canister and served the function of chemically conditioning the incoming ground water only. The steel cage was isolated from the copper canister by a plastic ribbon to avoid galvanic coupling of the metals. In package 4 the canister was embedded in 3 cm thick bentonite rings of high density (1600 kg/m^3 dry density) in direct contact with the copper surface (Figure 4). In package 5, no bentonite was present in the steel cage, and the copper surface was exposed directly to the ground water. In the void volume inside the steel cage (on top of the copper canister, which was shorter than the steel cage, see Figure 4), electrodes and corrosion specimens of both iron and copper were installed on a nylon rack and were isolated from each other. Further details of the design of the MiniCan test series are described in Smart and Rance (2009). MiniCan 3 was retrieved in 2011 and packages 4 and 5 were retrieved in 2015. During post-test examination it was found that microbial sulfate reduction had a pronounced influence on the corrosion of cast iron components in both MiniCan 3 (low density bentonite) and 5 (no bentonite). As a result, most surfaces in these packages, copper specimens included, were covered with a black deposit consisting partly of iron sulfides (Smart and Rance 2009, Smart et al. 2012, Gordon et al. 2017).

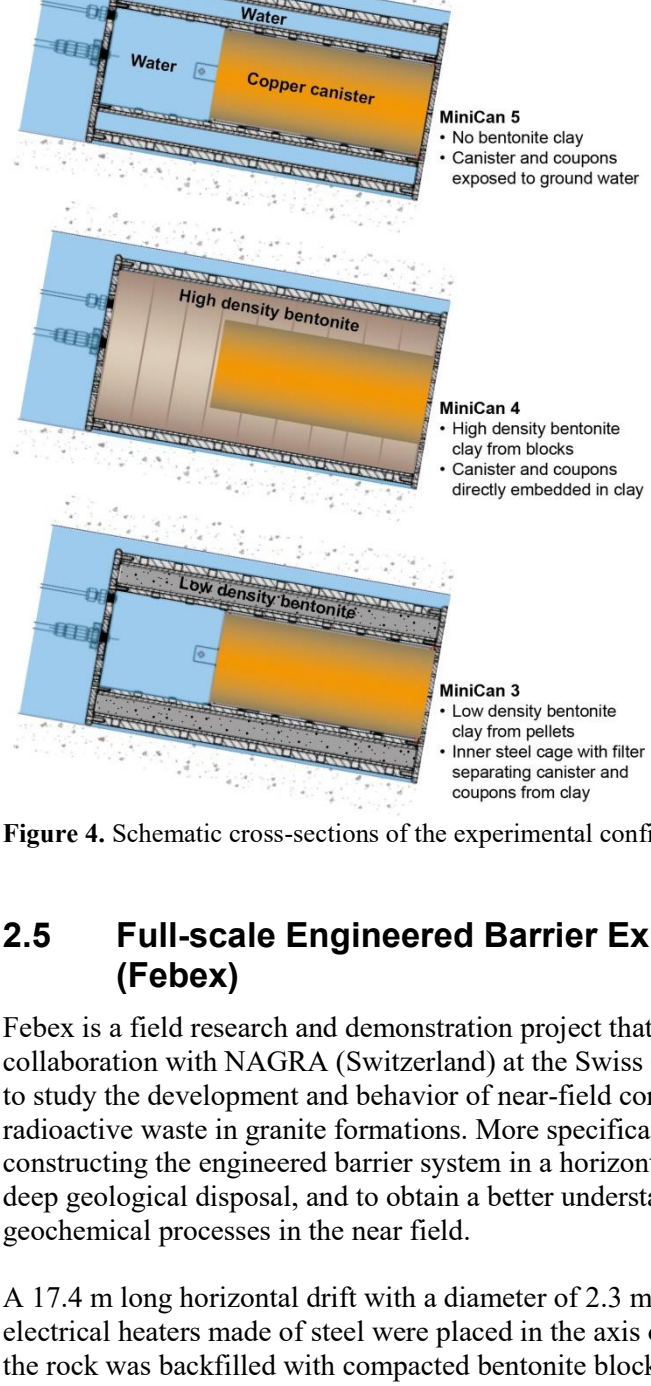

Figure 4. Schematic cross-sections of the experimental configurations of MiniCan 3, 4, and 5.

2.5 Full-scale Engineered Barrier Experiment in Crystalline Host Rock (Febex)

Febex is a field research and demonstration project that is conducted by Enresa (Spain) in collaboration with NAGRA (Switzerland) at the Swiss Grimsel Test Site (GTS). The aim of Febex is to study the development and behavior of near-field components in a repository for high-level radioactive waste in granite formations. More specifically, it is a demonstration of the feasibility of constructing the engineered barrier system in a horizontal configuration, as in the Spanish concept for deep geological disposal, and to obtain a better understanding of the thermo-hydro-mechanical and geochemical processes in the near field.

A 17.4 m long horizontal drift with a diameter of 2.3 m was excavated in the Grimsel rock. Two electrical heaters made of steel were placed in the axis of the drift. The gap between the heaters and the rock was backfilled with compacted bentonite blocks, requiring nearly 116 tons of bentonite. The backfilled area was sealed with a concrete plug. A more detailed and illustrated description of Febex is found in Lanyon and Gaus (2016). The experiment was started in 1997 and was carried out in two phases, so that the outer section and its heater were retrieved in 2002, and the inner section was retrieved during 2015. Several instruments were mounted in the experimental zone, both in the bentonite buffer and in the host rock, to monitor parameters such as temperature, humidity, pressure, displacements, ground water chemistry, and redox development. Amongst the instruments and test specimens were two copper coupons from the inner section, mounted on a plastic rack near the central heater and heated to around 100 °C during the 18 year long exposure.

3 Results and discussion

3.1 Residual O_2 and development of redox conditions

The amount of residual oxygen available is determined by the volume, porosity, and water content of the bentonite clay at installation. Since the bentonite blocks are produced under aerobic conditions it can be assumed that the porosity and the pore water are saturated with air. The porosity of compacted bentonite blocks is typically around 0.4, and ca 65 % of the pore volume is filled with water, giving a remaining air-filled porosity of 0.14. Thus, since air contains 20.9 % molecular oxygen, and since the molar volume of an ideal gas is 0.0232 m^3/mol, 1 m^3 bentonite clay contains ca 1.3 moles of O_2. In this calculation of the molar volume of an ideal gas a rock temperature of 10 °C was assumed, since this is a typical temperature in the bedrock at Äspö HRL and since heating in PR, LOT and ABM was started after installation and closure of the test. For comparison, the water filled fraction of the porosity contains ca 0.065 mol O_2 per m^3 bentonite, i.e. a minor contribution compared with the O_2 from the air filled porosity.

PR has the same dimensions as the KBS-3 reference design, in which each deposition hole contains 16.3 m^3 bentonite and thus ca 21 moles of O_2. An additional contribution of ca 7 moles of O_2 comes from the initially air-filled gap of ca 1 cm between the canister and the bentonite rings. In addition, there is in principle an additional amount of 455 moles of O_2 per canister, if the total amount of oxygen in the backfill is divided equally between the canisters (SKB 2010).

The corrosion potential (E_{corr}) of the copper electrode in PR5 was measured just before retrieval of the outer section of PR and was then found to vary between -30 and -60 mV (SHE) (Rosborg 2013b). This can be compared to the E_{corr} of ca 220-260 mV (SHE), obtained for copper electrodes embedded in a bentonite test parcel in an aerobic laboratory environment for several years (Rosborg et al. 2012), suggesting that oxygen had been depleted during the seven years of exposure of the electrode in PR. Important to note though, the E_{corr} of copper is also sensitive to variations in the concentration of chloride. The E_{corr} measured before retrieval can also be compared with E_{corr} for copper electrodes in anoxic sulfide solutions which has been determined in laboratory tests to be -400 mV (SHE) or even lower (depending on the sulfide concentration) in anoxic sulfide solutions (Smith et al. 2004, 2007a, b). This indicates that although the outer section of PR (Figure 1) had been depleted of residual oxygen, it had still not become fully reducing, i.e. the sulfidic ground water of the Äspö site had not yet conditioned the chemistry of the clay. This conclusion is further supported by the examination of corrosion products in PR, discussed below in Section 3.2.

Table 1. Initial state and development of parameters controlling the early corrosion in repository-like field tests performed in the Äspö HRL. For LOT and MiniCan the corrosion depth was determined by mass-loss. For PR the corrosion depth was not measured by mass-loss but was instead estimated by integration of electrochemical measurements of corrosion rates (see further Rosborg 2013a).

Experiment	Prototyp 5	LOT A2	MiniCan 4
Bentonite buffer volume (m^3)	16.3	0.24	0.008
Initial air filled gap between copper and clay (mm)	10	8	-
Initial free water volume (m^3)	-	-	0.4
Residual O_2 (moles)	28	0.8	0.1
Temperature (°C)	35	30	15
Exposure time (y)	7	6	8
Copper specimen	Electrode C4	Coupon 30G	Coupon M4 7:1
Corrosion products	Cu_2O $Cu_2(OH)_2CO_3$	Cu_2O $Cu_2(OH)_3Cl$	Cu_2O Cu_2S
Corrosion depth (µm)	2.8-5.6	2.5	0.2

In LOT, each test hole contains 0.24 m^3 bentonite and thus 0.3 moles of O_2. A contribution of 0.5 moles of O_2 comes from the initially air-filled gap of 0.4 cm between the copper tube and the bentonite rings. No measurements of redox or corrosion potentials were made in LOT; however, a laboratory test has recently been made in which a copper heater was embedded in bentonite rings of similar dimensions as in LOT and ABM, i.e. 17 cm thick rings. The whole experimental package was contained in a stainless steel vessel. These tests showed that residual oxygen, initially comprising 21 % of the gas-phase, fell to about 1 % within 60 days of exposure with the copper heater present. The copper heater then had a maximum temperature of 80 °C. In this test the copper surface was initially washed with hydrochloric acid to remove surface contaminants and grease; however, when instead washing the copper surface with ethanol and repeating the test, consumption of O_2 was ca 5 times slower. At the time of writing the test has not been terminated but as it seems from the online measurements it will take up to 10 months for the system to reach below 1% O_2 (Svensson D 2018, personal communication). When the test was repeated at room temperature and without the copper heater, the oxygen level in the gas-phase remained stable at 22 % for 111 days (Birgersson and Goudarzi 2018). These results show that: 1) a heated copper surface is an efficient sink for consumption of O_2 via corrosion of the copper surface, however, the kinetic efficiency depends on the surface treatment, 2) stainless steel is not an efficient sink for O_2 (probably due to passivity of the steel surface), and 3) at low temperature bentonite clay does not react with O_2 or reacts very slowly[1]. Based on these results, it is reasonable to assume that in the heated packages of the LOT series, having a central copper heater, residual oxygen was primarily consumed by copper corrosion within a period of several months. Oxygen consumption was probably slower in the LOT packages of lower temperature. Most likely, O_2 consumption was also slower in the ABM series, in which the central heater was made

[1] The redox reactivity of the clay depends on the amount of pyrite, which varies between different bentonite materials, and also within different batches of the same material.

of steel and the only copper surface was the comparatively small surface of the corrosion specimens mounted in the bentonite rings.

When comparing PR with LOT or ABM, it is important to note that while the electrodes in PR were installed in 35 cm thick bentonite rings (difference between outer and inner diameter of the rings), the copper specimens in LOT and ABM were mounted in 17 cm thick rings. This means that the amount of residual O_2 available for corrosion differed between the tests. Other notable differences between the field tests are: 1) the total metal surface, competing with the corrosion specimens for O_2, 2) the temperature, which varied between and spatially within the tests, 3) the bentonite used (most of the Äspö tests contained SKB's reference clay MX-80, while ABM contained different types), and 4) the time required to reach full water saturation of the bentonite. These variations make direct comparison of the tests complicated and a more precise understanding of O_2 consumption in the different tests would require three dimensional modeling of O_2 diffusion with the actual experimental configuration, bentonite density, water content and temperature of the specific tests.

Each MiniCan borehole contained ca 400 liters of ground water, presumably saturated with air (ca 10 mg O_2 per litre water) when the packages were installed and the boreholes were sealed. Each MiniCan experiment thus contained ca 0.1 mole of O_2 from the water and in addition the packages with clay contained less than $5 \cdot 10^{-3}$ moles of O_2 from the bentonite in which the canister and other corrosion specimens were embedded. It is important to note that the amount of residual oxygen available in the bentonite clay at start was much lower in MiniCan as compared with PR, LOT and ABM (Table 1). MiniCan is the only field test in SKB's regime where both redox- (E_h) and corrosion potentials (E_{corr}) have been measured continuously. The measurements showed that the boreholes became reducing within a few months from closure (Smart et al. 2015). The redox potential (E_h) had by then stabilized at ca -300 mV (SHE) and E_{corr} for copper had converged to around -400 mV (SHE). The corrosion potential in anoxic sulfide solution is controlled by [HS^-] which was in the order of 10^{-6} M in MiniCan during the exposure period, albeit with some variation over time and between the five packages. The E_{corr} values measured in MiniCan are in reasonable agreement with measurements in laboratory experiments, for which E_{corr} was ca -650 mV (SCE) (i.e. -400 mV (SHE)) at [HS^-]=$2.6 \cdot 10^{-5}$ M and decreasing steeply for higher sulfide concentrations (Smith et al. 2004, 2007a, b). For MiniCan 4, directly embedded in high density clay, measurements of E_h in the borehole indicate that it took about one year before the potential stabilized, however, E_{corr} of both the copper canister and other electrodes inside the experimental assembly had stabilized already after ca 4 months (Figure 4-19 in Smart et al. 2015). Due to technical problems with the counter electrode, the development of E_{corr} before 4 months could not be recorded, meaning that the interior of MiniCan 4 might have become depleted of O_2 even earlier than after 4 months.

The amount of residual oxygen at installation of Febex can be estimated from the volume of bentonite clay in the backfilled tunnel (17 m long and 2.2 m in diameter) containing the two heaters (4.5 m long, 1 m in diameter), which corresponds to an amount of ca 57 m^3 clay. Using the same assumptions regarding porosity as for PR this corresponds to an initial amount of ca 74 moles of O_2. Measurements during the test showed that the gas in the bentonite pore system had an atmospheric contain of ca 21 % O_2 at start and that it took ca 1.5 years before the O_2 level decreased to reach low levels (Giroud 2014). The reason for this rather long aerobic period in Febex is not fully understood but it has been suggested that the system was not completely air tight due to cables for instrumentation going through the concrete plug. Furthermore, the clay system was not fully water saturated and some regions were very dry, which allows air and other gases to diffuse rapidly through the system.

3.2 Corrosion products

When the canisters of PR5 and PR6 were retrieved after more than eight years of exposure, large areas were covered with a dark brown deposit, here and there decorated with blue-green regions, indicating that divalent copper corrosion products had formed. By visual inspection, the coupons (LOT/S1, LOT/A0, and LOT/A2) and electrodes (LOT/A2, PR5) mounted in the bentonite clay surrounding the

central canister or tube all had a similar appearance at retrieval (Figure 5a-c). In order to characterize the corrosion products, specimens from PR5 and LOT/A2 have been analysed using x-ray diffraction (XRD), Fourier transformed infra-red spectroscopy (FTIR), Raman spectroscopy, and scanning electron microscopy in combination with energy dispersive spectroscopy (SEM-EDS).

The appearance of the cylindrical electrode in PR5/C4 is shown in Figure 5b. FTIR transmission spectra were dominated by bands from bentonite (Si-O vibrations at 1,000–1,100 cm^{-1} and OH bands at 3,600 cm^{-1}). However, in the spectrum from a brown region of the surface a peak appeared at 620 cm^{-1}, corresponding to cuprite (Cu_2O) (Fig 3-9 in Rosborg 2013b). Similarly, the FTIR spectrum from a blue-green spot revealed several bands matching well with the spectrum of malachite ($Cu_2(OH)_2CO_3$). In agreement with FTIR, XRD spectra revealed the presence of montmorillonite (from bentonite), as well as cuprite and malachite. The Raman spectrum of a blue-green spot matches with malachite ($Cu_2(OH)_2CO_3$) but not with, for example, paratacamite ($Cu_2(OH)_3Cl$).

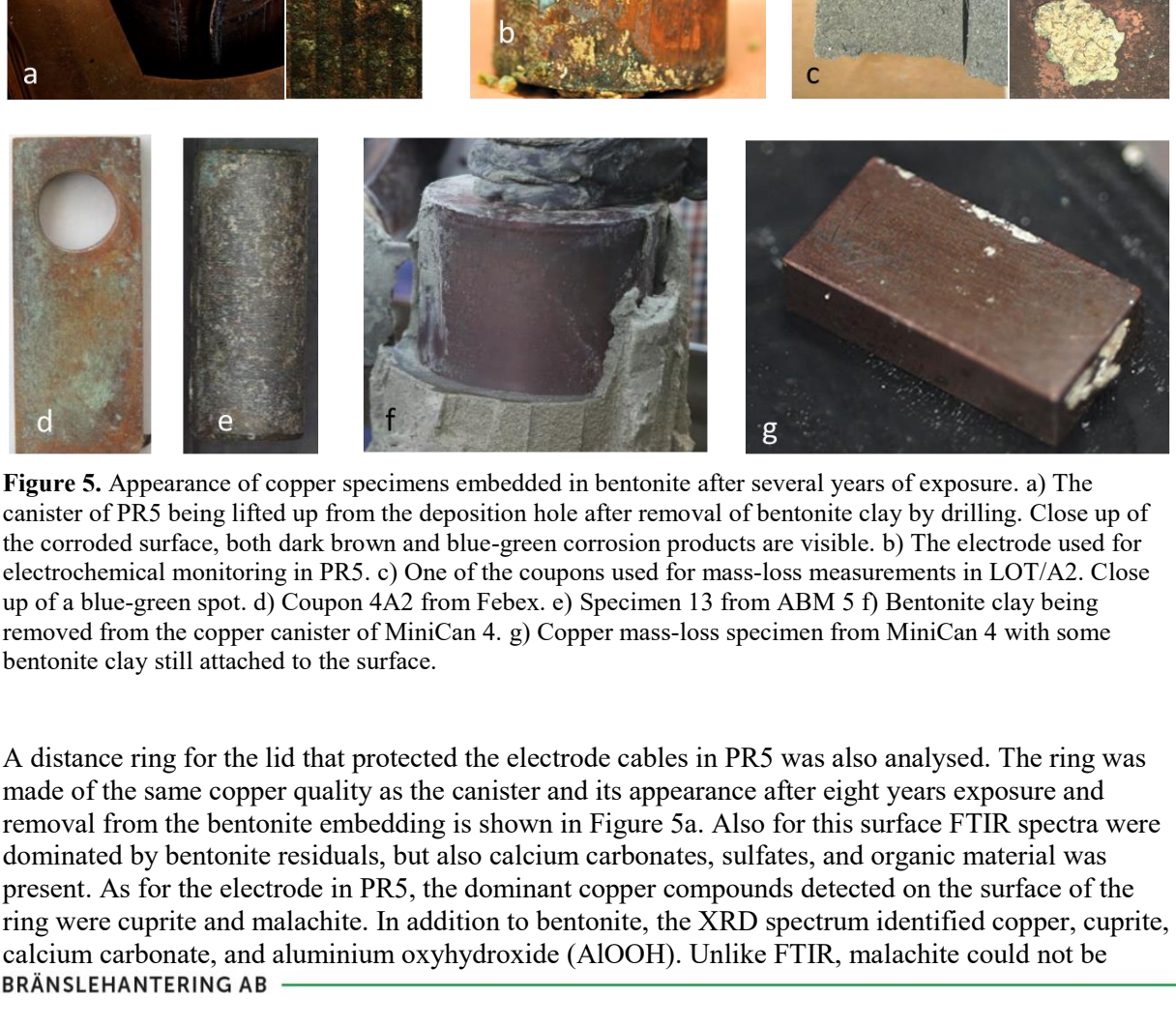

Figure 5. Appearance of copper specimens embedded in bentonite after several years of exposure. a) The canister of PR5 being lifted up from the deposition hole after removal of bentonite clay by drilling. Close up of the corroded surface, both dark brown and blue-green corrosion products are visible. b) The electrode used for electrochemical monitoring in PR5. c) One of the coupons used for mass-loss measurements in LOT/A2. Close up of a blue-green spot. d) Coupon 4A2 from Febex. e) Specimen 13 from ABM 5 f) Bentonite clay being removed from the copper canister of MiniCan 4. g) Copper mass-loss specimen from MiniCan 4 with some bentonite clay still attached to the surface.

A distance ring for the lid that protected the electrode cables in PR5 was also analysed. The ring was made of the same copper quality as the canister and its appearance after eight years exposure and removal from the bentonite embedding is shown in Figure 5a. Also for this surface FTIR spectra were dominated by bentonite residuals, but also calcium carbonates, sulfates, and organic material was present. As for the electrode in PR5, the dominant copper compounds detected on the surface of the ring were cuprite and malachite. In addition to bentonite, the XRD spectrum identified copper, cuprite, calcium carbonate, and aluminium oxyhydroxide (AlOOH). Unlike FTIR, malachite could not be

identified with XRD. A possible explanation for this inconsistency between FTIR and XRD, could be that the malachite crystals were too small or had too low crystallinity to be detected by XRD. The elemental composition of the corroded surfaces was qualitatively supported by GDOES (Glow Discharge Optical Emission Spectroscopy), which showed that oxygen was the dominant element (except copper), followed by silicon, aluminium and iron. No crystalline sulfide compounds could be identified with XRD or FTIR, however, sulfur was found with GDOES but in amounts orders of magnitude lower than oxygen (Taxén et al. 2012).

After breaking loose the copper coupons from the bentonite in LOT/A2/30, corrosion products were observed both on the copper coupon and on the bentonite surfaces facing the copper coupon (Figure 5c). A brown deposit with blue-green spots covered most of the copper coupons, although, areas with a metallic surface were also observed. When scraping off the brown corrosion product attached to the inner bentonite surface, blue-green corrosion products appeared, meaning that the blue-green product had formed on top of the brown product on the copper surface. XRD analysis confirmed that the main constituent of the brown surface deposit was cuprite and that the blue-green corrosion products contained paratacamite ($Cu_2(OH)_3Cl$). The blue-green corrosion product was not only unevenly distributed on the copper coupons, but also appeared in the clay adjacent to the coupons. SEM-EDS analysis revealed that the blue-green product in the clay had a higher content of Al, Si, and Fe, as compared to the adjacent surface on the coupon, meaning that these products had interacted chemically with the bentonite (Table A3-2 in Karnland et al. 2009). The higher chloride content of the blue-green spots, as compared with adjacent brown areas, supports the observation of paratacamite by XRD. While no copper sulfides were detected on the copper coupons with XRD or FTIR, particles rich in both copper and sulfur were identified at the copper-bentonite interface using SEM-EDS.

Copper specimens from ABM 5 have so far only been analysed for corrosion mass-loss (Section 3.3). The composition of the corrosion products will be analysed for the remaining copper specimens. Due to the similarity in experimental design and configuration, it is reasonable to presume that the corrosion product in ABM was similar to the LOT series (Gordon et al. 2018).

Table 2. Surface elemental composition of copper specimens in MiniCan 4 (EDS data from Appendix 10 in Gordon et al. 2017).

Sample/surface	O (wt%)	S (wt%)	O/S: mass	O/S: atoms
Cu electrode (5:1, point 5)	1.8	4.3	0.4	0.8
Cu electrode (6:1, analysis 1, point 6)	6.2	4.9	1.3	2.6
Cu electrode (6:1, analysis 1, point 7)	7.4	4.9	1.5	3.0
Cu electrode (6:1, analysis 2, point 4)	5.5	5.5	1.0	2.0
Cu mass loss (7:1, point 3)	3.0	5.6	0.5	1.0
Cu canister outer surface (25:1, analysis 1, point 3)	5.1	2.5	2.0	4.0
Cu canister outer surface (25:1, analysis 2, point 2)	3.5	2.7	1.3	2.6
Cu canister weld surface (26:1, point 4)	3.0	6.3	0.5	1.0
Cu canister weld surface (26:1, point 5)	2.6	2.6	1.0	2.0
Cu canister weld surface (26:1, cross section, point 4)	9.4	8.8	1.1	2.2
Average all samples/points	**4.8±2.3**	**4.8±1.9**	**1.0±0.5**	**2.0±1.0**

While the copper specimens of MiniCan 3 and 5 were not embedded in bentonite clay (and also contaminated by nearby corrosion of iron components) the copper specimens in MiniCan 4 were embedded in compact bentonite clay and were thus more comparable to copper surfaces in the other field tests. The surfaces of copper specimens in MiniCan 4 appeared to be covered with bentonite clay and a thin brown layer (Figures 5f and 5g). Raman spectroscopy was applied to several copper specimens, *e.g.* the outer canister surface and the mass-loss coupon, under strictly anoxic conditions and revealed mainly cuprite (Cu_2O) and sulfide, which was most likely chalchocite (Cu_2S). XRD was applied after some exposure to air and still showed cuprite and possibly some tenorite (CuO). Several copper surfaces in MiniCan 4 were examined regarding elemental composition using SEM-EDS (Appendix 10 in Gordon et al. 2017). Many of the analysed surfaces show bentonite as evident from the high content of Si, O, and Al. As bentonite contains oxygen, EDS spectra from these points do not

allow determination of the O/S ratio of the corrosion film. However, removing these data points and analysing bentonite free areas of the copper surfaces show that both the oxygen and sulfur contents were typically 2-9 wt.%. Notably, oxygen and sulfur occur in roughly similar amounts (wt.%) on the surfaces (Table 2). However, these numbers should be regarded as approximate, since there several factors complicating the interpretation of the EDS spectra, e.g. the semi-quantitative nature of EDS, the possibility that some Cu_2O formed during corrosion has been converted to Cu_2S, and adsorption of sulfate ions. Nevertheless, MiniCan is thus the only Äspö field test, in which a significant part of the corrosion was caused by sulfide. The explanation for this is that the residual amount of oxygen was smaller than in other field test (due to the smaller clay volume), that the flow of ground water was high at the location of MiniCan in the Äspö HRL, and that the ground water only had to diffuse through a few cm of bentonite clay to reach the copper surface.

The Febex experiment contained two copper specimens mounted in the bentonite clay close to the surface of the heater. The coupons have thus experienced high temperature (ca 100°C) during the 18 year long exposure. One of the specimens (4A2) was used for gravimetric determination of general metal loss, while the other (4A1) was used for surface examination and characterization of corrosion products. Both coupons had very similar appearance with a blue-green deposit covering large areas (Figure 5d). EDS spectra showed that the surface of coupon 4A1 was composed mainly of copper and oxygen. Brownish surfaces had a content of ca 20 wt% oxygen and traces of chloride, while blue-green areas had ca 40 wt% oxygen and a chloride content of ca 6 wt%. Elements from the bentonite clay were detected, but there were no indications of sulfur. The most plausible interpretation of the EDS data is thus that brownish surfaces were dominated by cuprite (Cu_2O), while blue-green deposits were composed of atacamite or paratacamite ($Cu_2(OH)_3Cl$). The presence of cuprite was confirmed by XRD.

In summary, the examination of copper surfaces from the field tests PR5, LOT/A2, MiniCan 4, and Febex, all resembling the KBS-3 concept in that the copper specimens were embedded in high density bentonite clay, shows that the corrosion in MiniCan 4 was less extensive (by mass-loss) and did not indicate any formation of Cu(II) corrosion products (Table 3). MiniCan 4 differed from the other experiments in two important aspects: it was at ambient temperature (ca 10°C) and it contained a very small amount of residual oxygen initially. In section 3.5 it will be analysed how these parameters might have affected the corrosion.

Table 3. Corrosion products identified on copper specimens from the test series LOT/A2, PR5, MiniCan 4, and Febex

Specimen	Technique	Corrosion Products	Reference
Febex/4A2, coupon	XRD, SEM-EDS	Cu_2O, $Cu_2(OH)_3Cl$	Wersin and Kober (2017)
PR5/C4 electrode	Raman, XRD, FTIR	Cu_2O, $Cu_2(OH)_2CO_3$	Rosborg (2013b)
PR5/lid distance ring	XRD, FTIR	Cu_2O, $Cu_2(OH)_2CO_3$	Taxén et al. (2012)
LOT/A2/30G coupon	XRD, SEM-EDS	Cu_2O, $Cu_2(OH)_3Cl$	Karnland et al. (2009)
MiniCan 4, coupon M4 7:1	Raman, SEM-EDS	Cu_2O, Cu_2S	Gordon et al. (2017)
MiniCan 4, canister surface	Raman, SEM-EDS	Cu_2O, Cu_2S	Gordon et al. (2017)

3.3 Corrosion depths determined by mass-loss

Gravimetric or mass-loss analysis of copper corrosion has been performed in several of the tests in MiniCan, LOT, ABM, and Febex. The average corrosion depth measured for a Febex copper specimen was ca 9 µm, while the depths from LOT and ABM varied between 2 and 5 µm, and all measurements in MiniCan were below 1 µm (Table 4). Mass-loss is a very robust method to quantify average corrosion depth since it does not invoke any assumptions about the corrosion process except that it occurs rather evenly over the surface.

Table 4. Gravimetric results and environmental parameters.

Coupon	T	t	Initial O_2	Buffer thickness	Mass- loss	Area	Average corr. depth	Integrated corr. rate	Reference
	°C	d	moles	cm	mg	cm^2	µm	µm y^{-1}	
Febex/4A2	100	6570	74	60	197	26.09	8.5	0.5	Wersin and Kober (2017)
LOT/S1/22A	50	487	0.8	8	80	24.5	3.7	3.1	Karnland et al. (2000)
LOT/A0/22A	80	710	0.8	8	86	20.25	4.8	2.4	Karnland et al. (2011)
LOT/A0/30C	35	710	0.8	8	83	20.25	4.6	2.4	Karnland et al. (2011)
LOT/A2/30G	30	2271	0.8	8	46	20.25	2.5	0.4	Karnland et al. (2009)
LOT/A2/30H	30	2271	0.8	8	27	20.25	1.5	0.2	Karnland et al. (2009)
ABM5/9	80	1825	0.8	8	43	9.5	5.0	1.0	Gordon et al. (2018)
ABM5/13	80	1825	0.8	8	19	9.5	2.3	0.5	Gordon et al. (2018)
ABM5/15	80	1825	0.8	8	25	9.5	2.9	0.6	Gordon et al. (2018)
ABM5/16	80	1825	0.8	8	23	9.5	2.7	0.5	Gordon et al. (2018)
MiniCan 3	15	1383	0.1	3	3.8	7.0	0.6	0.15	Smart et al. (2012)
MiniCan 4	15	3103	0.1	3	1.0	7.0	0.2	0.02	Gordon et al. (2017)
MiniCan 5	15	3103	0.1	-	5.9	7.0	0.9	0.11	Gordon et al. (2017)

3.4 Interpretation of integrated corrosion rates

Corrosion rates calculated as the measured corrosion depth (by mass-loss) divided by the whole exposure time, have been presented in several reports concerning the field tests discussed herein (Table 4). Important to note, these do not account for any changes in the corrosion process or mechanism due to changes in the environment during the exposure, and are thus not representative for the whole exposure period. In order to estimate the average corrosion rate under the initial aerobic period, information is needed regarding the amount of corrosion due to oxygen (and not sulfide), and the time it took for oxygen to be depleted.

In MiniCan 4, the integrated corrosion rate for the whole exposure period was 0.02 µm/y (Table 4). However, as was discussed above (Tables 2 and 3), both oxides and sulfides were present on the copper surfaces, and as it seems in similar amounts. Since it is known that O_2 was depleted within a few months (Section 3.1), it can be concluded that the initial oxygen driven corrosion must have occurred with an average rate that is much higher than 0.02 µm/y. For example, assuming that 50 % of the mass-loss was caused by O_2 corrosion, and that O_2 was depleted within 3 months, this would give an average corrosion rate of 0.4 µm/y during the first 3 months, i.e. twenty times higher than the integrated corrosion rate calculated for the whole exposure period of nearly 9 years. Consequently, the subsequent corrosion, most probably controlled by the diffusive transport of sulfide through the bentonite, must have occurred at a rate lower than the integrated corrosion rate for the whole exposure period. As mentioned in the discussion above when referring to Table 2, these numbers should be regarded as very approximate, since there are large uncertainties regarding the relative contributions of O_2 and sulfide driven corrosion. The calculation should not be used to predict corrosion rates during oxic or anoxic conditions, however, the example in the calculation serves to illustrate the principle problem with (and limited usefulness of) integrated corrosion rates when it is known that the corrosion process has changed during the exposure.

If the same corrosion process would have been dominating during the whole exposure periods of the field tests, i.e. if an oxidant was available at constant or similar concentration, the corrosion rate would have shown an exponential dependence on the temperature, as predicted by the Arrhenius equation. The relationship can be expressed as the logarithm of the rate plotted against the inverse temperature, which is then expected to give a linear plot (Figure 7). However, linear fitting of the logarithm of the nominal corrosion rates plotted against the inverse of the experimental temperature gave a very poor fit (R^2=0.28). The reason for the apparently weak relationship between the integrated corrosion rates and temperature, is to be found in the corrosion rates' poor representation for the whole exposure periods of the field tests, as discussed above.

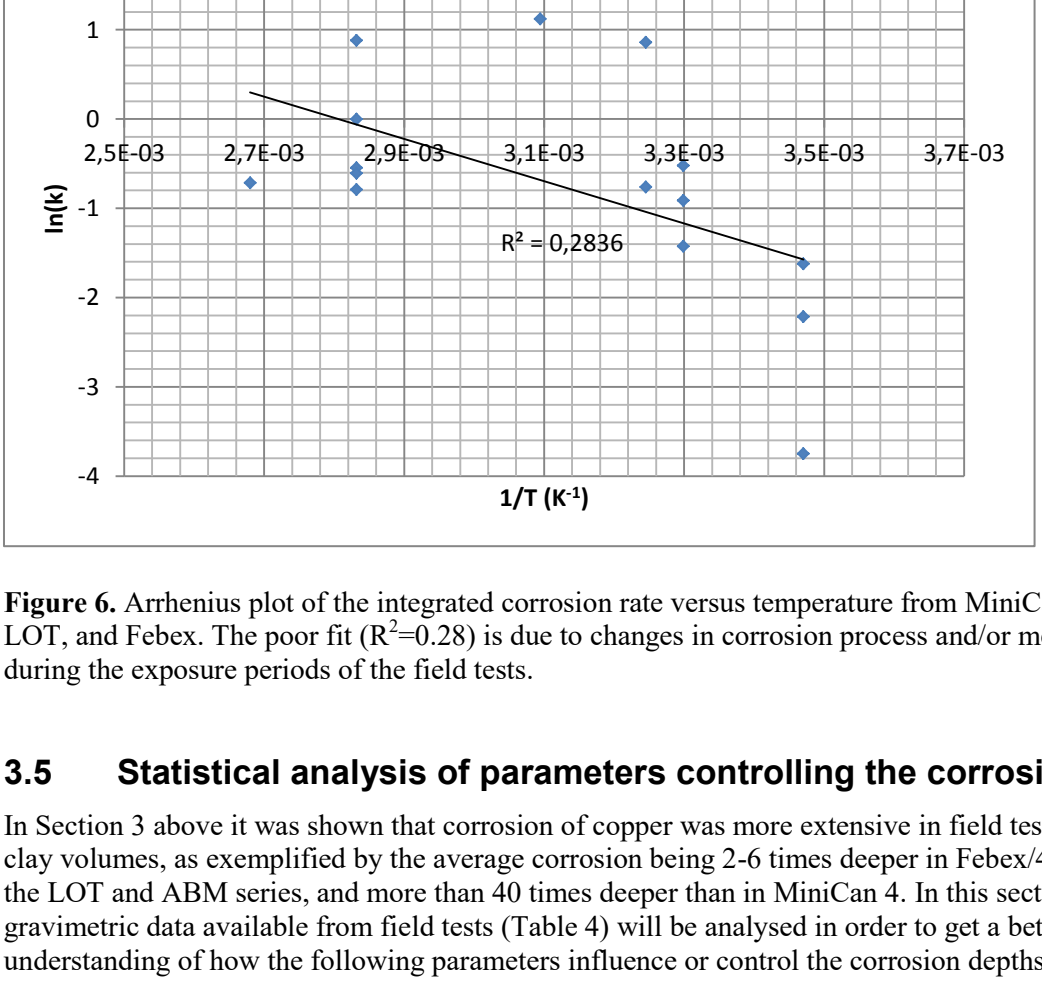

Figure 6. Arrhenius plot of the integrated corrosion rate versus temperature from MiniCan, ABM, LOT, and Febex. The poor fit (R^2=0.28) is due to changes in corrosion process and/or mechanism during the exposure periods of the field tests.

3.5 Statistical analysis of parameters controlling the corrosion

In Section 3 above it was shown that corrosion of copper was more extensive in field tests with large clay volumes, as exemplified by the average corrosion being 2-6 times deeper in Febex/4A2 than in the LOT and ABM series, and more than 40 times deeper than in MiniCan 4. In this section gravimetric data available from field tests (Table 4) will be analysed in order to get a better understanding of how the following parameters influence or control the corrosion depths measured:

- Temperature: measured as close as possible to the specific corrosion specimens.
- Time: taken as the total time of exposure in field, from installation to retrieval.
- Residual O_2: the total amount estimated as 1.3 moles O_2 per m^3 bentonite and contributions from initially air-filled gaps (see Section 3.1).
- Thickness of the bentonite buffer: used as an alternative estimate of O_2 available through diffusion.

In the first step, correlations between variables are analyzed. In the following steps, regression is used to elucidate the relative importance of the parameters. Possible outliers are excluded in a stepwise manner in order to further improve the understanding of which parameters that controlled the corrosion in these tests. The analysis was made using Statistica 12.0 and if nothing else is stated the statistical significance was set to a 95% confidence interval ($p<0.05$).

As the first step of analysis, a correlation matrix was set up for the parameters temperature, exposure time, residual O_2, corrosion depth and integrated corrosion rate. The analysis revealed relatively strong correlations of corrosion depth and temperature (R=0.73, Figure 7), as well as corrosion depth and residual O_2 (R=0.74, Figure 8). Both correlations were statistically significant.

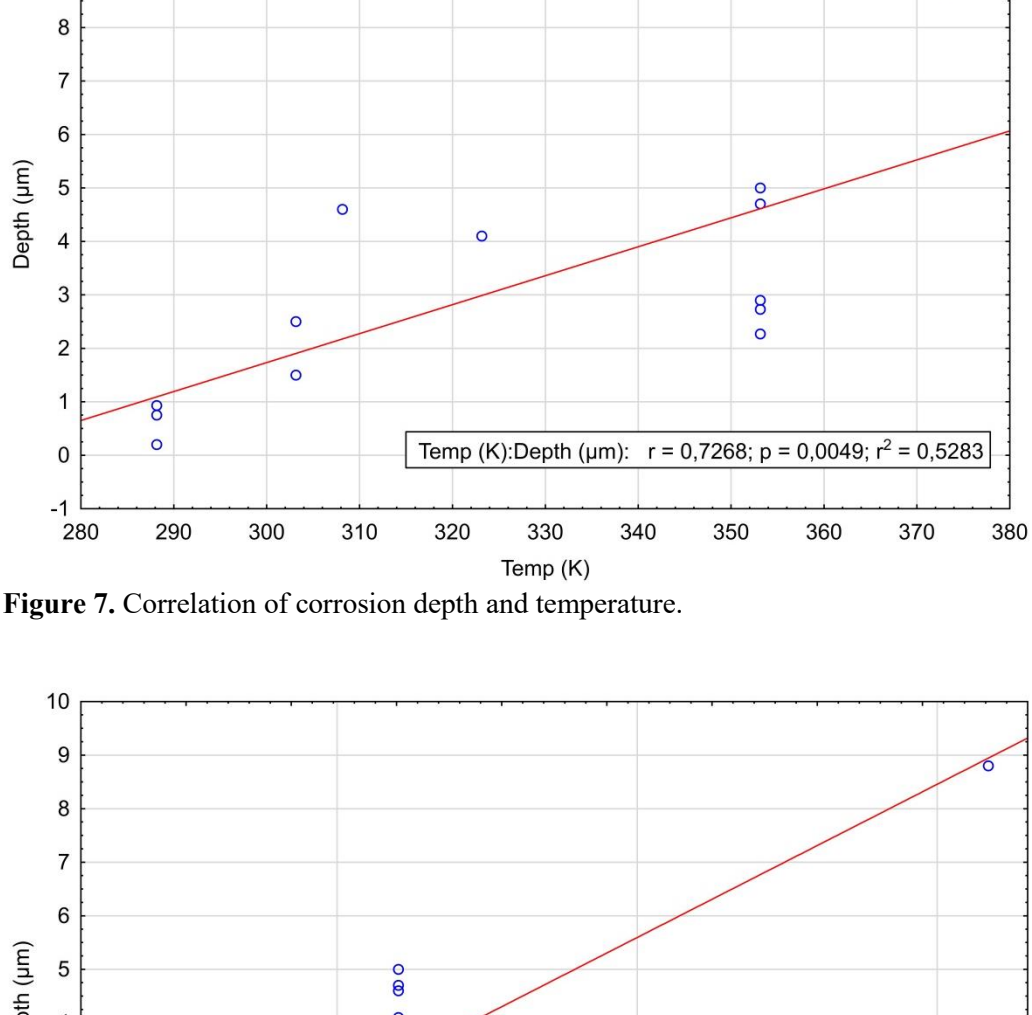

Figure 7. Correlation of corrosion depth and temperature.

Figure 8. Correlation of corrosion depth and residual O_2. The data is shown with a logarithmic x-axis in order to make the graph more readable, however, a linear fit was used to determine the correlation coefficient.

The correlation matrix also revealed a moderate but statistically significant negative correlation of the integrated corrosion rates with exposure time (R= -0.55). These three correlations are expected and understood. Residual O_2 is expected to control the corrosion on shorter time scales when no other oxidant (sulfide) is yet available. Higher temperature enhances the transport of O_2 to the copper surfaces, both by enhancing the diffusion rate of O_2 in water saturated clay, but also by drying out the heated zone which enhances convection of gases. The corrosion rate should decrease with time as O_2

is expected to be depleted on a timescale that is shorter than that required for sulfidic groundwater to become a significant contributor to corrosion.

However, the analysis also showed that there is a strong correlation of residual O_2 with time (R=0.84) as well as a moderate correlation between residual O_2 and temperature (R=0.46). These correlations have no physical meaning but are rather due to the experimental design; the longest exposures have been performed for the largest experiments, larger clay volume means larger amount of residual O_2, and the larger experiments have also been heated to higher temperatures. Another effect that comes into play here is that the larger and warmer experiments did not only contain more O_2 initially, but also, both the size and temperature makes the period required for water saturation of the clay longer, meaning that entrapped O_2 can be transported (via diffusion and convection) rapidly through the heated zone.

When linear regression analysis was performed on the whole set of data, i.e. including all gravimetric corrosion depths from Febex, LOT, ABM, and MiniCan in Table 4, temperature was found to be a relatively strong explanatory variable determining the corrosion depth (R^2=0.53, Table 6). The corresponding R^2 values for residual O_2 and bentonite thickness are 0.54 and 0.61, respectively. However, the explanatory degree of these variables depend to a some extent on the data point from Febex, in which the total amount of O_2 was much higher than in any other test. By excluding the Febex data from the linear regression analysis, temperature gets a slightly lower but still statistically significant explanatory degree of 43%, whereas residual O_2 only reduces to 57%. Thus, although the explanatory degree of temperature and O_2 when the whole data set is analyzed has some dependence on Febex, the dependence is not crucial.

Multiple regression analysis of the data set of Table 4, setting corrosion depth as the dependent variable and temperature, time, O_2, and bentonite thickness as independent variables, gave a total explanatory degree of 87%. Since the total amount of residual O_2 might not be available for corrosion of copper, especially not in Febex in which the diffusion distance is very long and since there was a large heated steel surface competing for O_2, it might be better to account for residual O_2 by approximating it with the bentonite thickness. Nevertheless, repeating the multiple regression analysis with the O_2 variable excluded had a very slight effect on the explanatory power of the model (R^2=0.86). Excluding both time and O_2, keeping only the temperature and bentonite thickness as independent variables, reduced the explanatory degree to 75%, which is still rather high.

As was discussed above in the linear regression analysis, the single data point from Febex could have an unbalanced influence on the data set. Therefore, a multiple regression analysis was performed on the data set with Febex excluded. The explanatory degree of the whole model now decreased from 87% to 79%, which is still rather high. Excluding O_2 among the independent variables, accounting for the available O_2 by the thickness of the bentonite instead, decreased the explanatory degree of the model further to 72%. It can thus be concluded that irrespective of whether Febex data is included or not in the analysis, and whether the availability of O_2 is described by the total amount of residual O_2 or the thickness of the bentonite clay, the most important variables determining the corrosion depth in the field tests are residual O_2 and temperature, as illustrated by the plot in Figure 9.

Table 5. Linear and multiple regression analysis of the gravimetric data set in Table 4. The values presented are coefficients of determination, R^2-values (in the text referred to as explanatory degree, in %). The abbreviation n.s. means not statistically significant, while n.a. means not applicable.

Type of regression	Corrosion depth vs				
	Temperature	Time	Residual O_2	Bentonite thickness	Whole model
Linear; all data	0.53	n.s.	0.54	0.61	n.a.
Linear: -Febex	0.42	0.54	0.57	0.51	n.a.
Multiple; all data	n.a.	n.a.	n.a.	n.a.	0.87
Multiple; -O_2	n.a.	n.a.	n.a.	n.a.	0.86
Multiple; -O_2, -time	n.a.	n.a.	n.a.	n.a.	0.75
Multiple; -Febex	n.a.	n.a.	n.a.	n.a.	0.79
Multiple; -Febex, - O_2	n.a.	n.a.	n.a.	n.a.	0.72

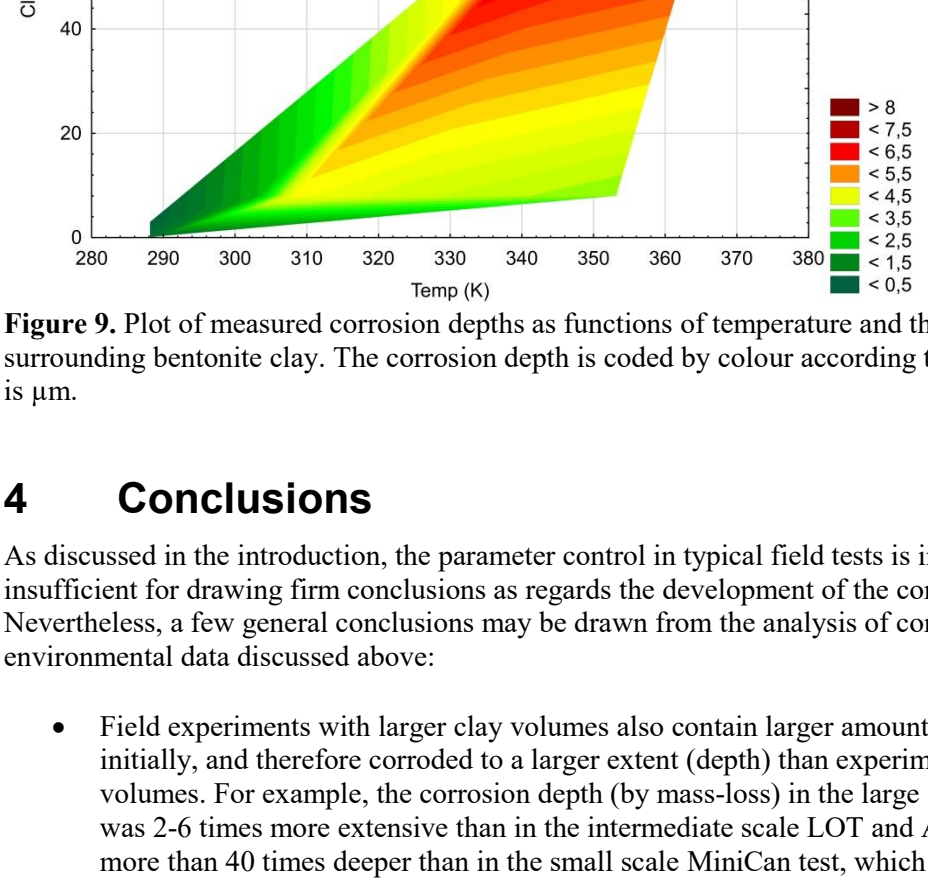

Figure 9. Plot of measured corrosion depths as functions of temperature and thickness of the surrounding bentonite clay. The corrosion depth is coded by colour according to the scale and the unit is µm.

4 Conclusions

As discussed in the introduction, the parameter control in typical field tests is in many cases insufficient for drawing firm conclusions as regards the development of the corrosion process. Nevertheless, a few general conclusions may be drawn from the analysis of corrosion and environmental data discussed above:

- Field experiments with larger clay volumes also contain larger amounts of residual oxygen initially, and therefore corroded to a larger extent (depth) than experiments with smaller clay volumes. For example, the corrosion depth (by mass-loss) in the large scale experiment Febex was 2-6 times more extensive than in the intermediate scale LOT and ABM experiments, and more than 40 times deeper than in the small scale MiniCan test, which contained very little residual oxygen due to its small clay volume.

- In experiments with larger clay volumes and larger amounts of residual oxygen, i.e. LOT, Prototype, and Febex, divalent oxygen containing corrosion products are observed, e.g. $Cu_2(OH)_3Cl$.

- In experiments with small amounts of residual oxygen, i.e. the MiniCan series, O_2 was depleted within a few months from the start of the experiment and only monovalent copper oxide (Cu_2O) was observed.

- While both Cu_2S and Cu_2O were observed spectroscopically and the elements O and S occurred in similar amounts on the copper surfaces in MiniCan, only small amounts of sulfur rich particles were detected in LOT, only traces of sulfur were found in Prototype, while no sulfur was detected on the copper specimens in Febex.

- In the field experiments reviewed, the measured corrosion depths correlated well with both the amount of residual O_2 and temperature. It is thus concluded that the corrosion of copper under repository like initial conditions is controlled primarily by residual O_2 and temperature.

- In the conceptual corrosion model employed in SKB's safety assessments, the early corrosion is controlled by mass-balance of oxygen, while the subsequent long-term sulfide corrosion is controlled by sulfide transport limitations, i.e. the low sulfide concentration in the ground water and diffusion through the bentonite clay. This conceptual model is compatible with the results of the field experiments reviewed and analyzed herein.

References

SKB's (Svensk Kärnbränslehantering AB) publications can be found at www.skb.com/publications.

Birgersson M, Goudarzi R, 2018. Investigations of gas evolution in an unsaturated KBS-3 repository. SKB TR-18-11, Svensk Kärnbränslehantering AB.

Giroud N, 2014. FEBEX – assessment of redox conditions in phase 2 before dismantling. Nagra Arbeitsbericht NAB 14-55, Nagra, Switzerland.

Gordon A, Sjögren L, Taxen C, Johansson A J, 2017. Retrieval and post-test examination of packages 4 and 5 of the MiniCan field experiment. SKB TR-16-12, Svensk Kärnbränslehantering AB.

Gordon A, Pahverk H, Börjesson E, Johansson A J, 2018. Examination of copper corrosion specimens from ABM 45, package 5. SKB TR-18-17, Svensk Kärnbränslehantering AB.

Karnland O, Sandén T, Johannesson L-E, Eriksen T, Jansson M, Wold S, Pedersen K, Motamedi M, Rosborg, B, 2000. Long term test of buffer material. Final report on the pilot parcels. SKB TR-00-22, Svensk Kärnbränslehantering AB.

Karnland O, Olsson S, Dueck A, Birgersson M, Nilsson U, Heman-Håkansson T, Pedersen K, Nilsson S, Eriksen T, Rosborg B, 2009. Long term test of buffer material at the Äspö Hard Rock Laboratory, LOT project. Final report on the A2 test parcel. SKB TR-09-29, Svensk Kärnbränslehantering AB.

Karnland O, Olsson S, Sandén T, Fälth B, Jansson M, Eriksen T, Svärdström K, Rosborg B, 2011. Long term test of buffer material at the Äspö HRL, LOT project. Final report on the A0 test parcel. SKB TR-09-31, Svensk Kärnbränslehantering AB.

King F, Lilja C, Vähänen M, 2013. Progress in the understanding of the long-term corrosion behaviour of copper canisters. Journal of Nuclear Materials 438, 228–237.

King F, Chen J, Qin Z, Shoesmith D, Lilja C, 2017. Sulphide-transport control of the corrosion of copper canisters. Corrosion Engineering, Science and Technology 52, 210–216.

Lanyon G W, Gaus I, 2016. Main outcomes and review of the FEBEX In Situ Test (GTS) and Mock-up after 15 years of operation. Nagra Technischer Bericht NTB 15-04, Nagra, Switzerland.

Rosborg, 2013a. Recorded corrosion rates on copper electrodes in the Prototype Repository at the Äspö HRL. SKB R-13-13, Svensk Kärnbränslehantering AB.

Rosborg, 2013b. Post-test examination of a copper electrode from deposition hole 5 in the Prototype Repository. SKB R-13-14, Svensk Kärnbränslehantering AB.

Rosborg B, Eden D, Karnland O, Pan J, Werme L, 2004. Real-time monitoring of copper corrosion at the Äspö HRL. In Féron D, Macdonald D D (eds). Prediction of long term corrosion behaviour in nuclear waste systems: proceedings of the 2nd International Workshop Organized by the Working Party on Nuclear Corrosion (WP4) of the European Federation of Corrosion (EFC), Nice, September 2004 (EUROCORR'2004). Chatenay-Malabry, France: Andra, 11–23.

Rosborg B, Kosec T, Kranjc A, Kuhar V, Legat A, 2012. The corrosion rate of copper in a bentonite test package measured with electric resistance sensors. SKB R-13-15, Svensk Kärnbränslehantering AB.

Sandén T, Nilsson U, Andersson L, Svensson D, 2018. ABM45 experiment at Äspö Hard Rock Laboratory. Installation report. SKB P-18-20, Svensk Kärnbränslehantering AB.

SKB, 2010. Corrosion calculations report for the safety assessment SR-Site. SKB TR-10-66, Svensk Kärnbränslehantering AB.

Smart N R, Rance A P, 2009. Miniature canister corrosion experiment – results of operations to May 2008. SKB TR-09-20, Svensk Kärnbränslehantering AB.

Smart N, Rance A, Reddy B, Fennell P, Winsley R, 2012. Analysis of SKB MiniCan Experiment 3. SKB TR-12-09, Svensk Kärnbränslehantering AB.

Smart N, Reddy B, Nixon D, Rance A, Johansson A J, 2015. A Miniature Canister (MiniCan) Corrosion experiment. Progress report 5 for 2008–2013. SKB P-14-19, Svensk Kärnbränslehantering AB.

Smith J, Qin Z, Shoesmith D, King F, Werme L, 2004. Corrosion of copper nuclear waste containers in aqueous sulphide solutions. MRS Online Proceedings Library 824, Scientific Basis for Nuclear Waste Management XXVIII.

Smith J, Qin Z, King F, Werme L, Shoesmith D W, 2007a. Sulfide film formation on copper under electrochemical and natural corrosion conditions. Corrosion 63, 135–144.

Smith J, Wren J C, Odziemkowski M, Shoesmith D W, 2007b. The electrochemical response of preoxidized copper in aqueous sulfide solutions. Journal of The Electrochemical Society 154, C431–C438.

Svemar C, Johannesson L-E, Grahm P, Svensson D, Kristensson O, Lönnqvist M, Nilsson U, 2016. Prototype Repository Opening and retrieval of outer section of Prototype Repository at Äspö Hard Rock Laboratory**.** Summary report. SKB TR-13-22, Svensk Kärnbränslehantering AB.

Taxén C, Lundholm M, Person D, Jakibsson D, Sedlakova M, Randelius M, Karlsson O, Rydgren P, 2012. Analyser av koppar från prototypkapsel 5 och 6. SKB P-12-22, Svensk Kärnbränslehantering AB. (In Swedish.)

Wersin P, Kober F (eds), 2017. FEBEX-DP. Metal corrosion and iron–bentonite interaction studies. Nagra Arbeitsbericht NAB 16-16, Nagra, Switzerland.

Corrosion Science 210 (2023) 110833

Contents lists available at ScienceDirect

Corrosion Science

journal homepage: www.elsevier.com/locate/corsci

Penetration of corrosive species into copper exposed to simulated O_2-free groundwater by time-of-flight secondary ion mass spectrometry (ToF-SIMS)

Xiaoqi Yue [a], Per Malmberg [b], Elisa Isotahdon [c], Vilma Ratia-Hanby [c], Elina Huttunen-Saarivirta [c], Christofer Leygraf [a], Jinshan Pan [a,*]

[a] Div. of Surface and Corrosion Science, Dept. of Chemistry, KTH Royal Institute of Technology, Stockholm, Sweden
[b] Dept. of Chemistry and Chemical Engineering, Chalmers University of Technology, Gothenburg, Sweden
[c] VTT Technical Research Centre of Finland Ltd., Espoo, Finland

ARTICLE INFO

Keywords:
Copper
Anoxic corrosion
Sulfide
ToF-SIMS
Nuclear waste

ABSTRACT

ToF-SIMS analysis of copper samples after exposures to simulated groundwater with and without sulfide addition was performed to investigate the penetration of corrosive species containing H, S, O, and Cl, into copper. Depth profiles show extent of penetration and 2D/3D images reveal local elemental distribution of the corrosive species at different depths inside copper. Pre-oxidation did not reduce the penetration while sulfide additional in groundwater and exposure at 60 °C significantly promoted the penetration. The extent of penetration of the corrosive species into copper demonstrates the need for risk assessment of complex corrosion forms such as sulfide-induced embrittlement and cracking.

1. Introduction

Spent fuel from nuclear power plants is highly radioactive and its safe disposal is as important as nuclear power plant safety. Governmental regulations require safe isolation of nuclear waste for a minimum of 100,000 years, which imposes a great engineering challenge. The nuclear waste disposal concept in Sweden and Finland is based on a three-barrier system, where the spent fuel is placed in cast-iron inserts, which are then sealed in copper canisters as the first barrier. The canisters are surrounded by a bentonite clay layer as the second barrier, further placed in bedrock (third barrier) in the depth of 400–1000 m [1,2]. High-purity oxygen-free phosphorus-containing copper (OFP-Cu) has been chosen for fabricating the canisters that will be placed in granite environments under anaerobic reduction and anoxic aqueous conditions. The bentonite clay is a buffer material between the bedrock and the canisters, swelling when exposed to water and thus dampening minor movements within the repository system, and retaining eventual release of radioactive nuclides upon possible canister failure. The bedrock provides the outermost barrier between the nuclear waste and the biosphere [1,2].

During long-term storage in the repository of the Cu canisters, cracks in the bedrock and the swelling of bentonite by groundwater lead to a direct contact of the Cu canisters with groundwater and the microbes in it. The groundwater contains a high level of Cl^- and SO_4^{-2} ions, and microbiological activity in the vicinity or on the surface of the canister produces sulfide species (mainly HS^- ions) [3–6]. Trapped O_2 exists in the system during initial period of the repository closure, but is gradually consumed by oxidation reactions and microorganisms. Once the trapped O_2 is completely consumed, the major threat to the long-term durability of the canister is corrosion by sulfide species (e.g., HS^-) produced in the groundwater by microbial activity and/or mineral dissolution. Microbial activity has been reported to initiate and accelerate general and localized corrosion of Cu, and cause a biotically-induced formation of a Cu_2S layer [3–7]. Corrosion of Cu under oxic and anoxic conditions, and the influence of radiation and microbiological activity, have been investigated, often separately, over 40 years [8–13]. Studies of Cu corrosion were often focused on chemical and electrochemical degradation of copper at the electrolyte/metal interface, and analysis of the corrosion products formed on the surface [14,15]. Chemical conversion of a native Cu_2O film to Cu_2S on the surface has been observed [16], and S-induced corrosion detected down to the depth of 100 nm into the Cu material [17]. At atomic level, the dissociation of sulfide species on the Cu surface is a spontaneous process, releasing atomic S and H. The co-existence with S promotes the H adsorption into copper according to DFT calculations [18,19]. Moreover, sulfide-induced corrosion reactions can generate H on the Cu

* Corresponding author.
E-mail address: jinshanp@kth.se (J. Pan).

https://doi.org/10.1016/j.corsci.2022.110833
Received 16 September 2022; Received in revised form 8 November 2022; Accepted 14 November 2022
Available online 21 November 2022

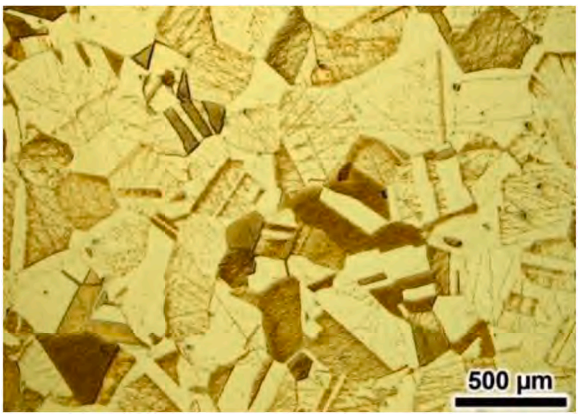

Fig. 1. Optical micrograph of an etched OFP-Cu material showing typical microstructure with large grains (of different crystallographic orientations) and annealing twins [19]. Thin lines show grinding scratches where plastic deformation exist.

surface [14]. Atomic H can also be produced at the water/Cu interface through radiolysis of water, and gamma radiation from spent nuclear fuel greatly increases the H generation on Cu, up to several orders of magnitude depending on the dose of the radiation [12,13]. In general, H has detrimental effects on the mechanical properties of Cu and can create voids and microcracks in Cu materials [20–23]. Adsorption and diffusion of H in Cu depend on the surface condition and presence of microstructural defects, such as dislocations and inclusions, and grain boundaries are the primary trapping sites of H [24]. In the Cu microstructure, H-induced lattice deformations may be heterogeneous, giving rise to local strains and stresses. Therefore, H incorporation into Cu can lead to the formation of a macroscopic lattice expansion, especially when accumulated in the surface region. H-induced strain localization has been observed in Cu in the initial stage of plastic deformation [25], and friction stir welding to seal the canister was found to increase H uptake in the weld zone and lead to strain localization around it [26]. H incorporation into Cu material leads to accelerated creep and the formation of microcracks with an intergranular nature [27]. H-induced damage of Cu canister has, so far, been considered to be negligible due to the belief that the H permeation depth would be too small to influence the mechanical integrity of Cu canister [28,29]. However, in the presence of tensile strains, sulfide has been shown to cause stress corrosion cracking (SCC) of Cu in anaerobic chloride containing environments [10,11,30].

A recent review gives an overview of the corrosion issues, debated questions, and ongoing research programs [6]. The corrosion of Cu canister has been assessed under expected repository conditions using a uniform corrosion rate to calculate the corrosion allowance [6]. However, the risks for several complex forms of Cu corrosion have been debated for a long time, even in the Land and Environmental Court of Sweden, which concluded that further information is needed regarding five issues: *i*) corrosion due to reaction in O_2-free water; *ii*) pitting due to reaction with sulfide; *iii*) SCC due to reaction with sulfide; *iv*) hydrogen embrittlement (HE); *v*) the effect of radioactive radiation on pitting, SCC and HE. Swedish Nuclear Fuel and Waste Management Co (SKB) has addressed these issues in an official report [31]. However, there are still intensive debates about these issues in Sweden [19,32,33]. Earlier in 2022, the Swedish government made a decision allowing SKB to start the long process preparing for the final disposal, meanwhile requesting regular revisions of the safety risk assessment of the system and eventual improvement. Clearly, there is a need to gain a deep understanding of the roles of H, S, O, and Cl in SCC and HE of Cu during the long exposure to the groundwater containing sulfide. This requires the detection of penetration and distribution of these corrosive species into the Cu microstructure. In this work, we utilized time-of-flight secondary ion mass spectroscopy (ToF-SIMS) to reveal the penetration of H, S, O, and Cl into Cu caused by the exposure to a O_2-free simulated groundwater with and without additional sulfide. This communication is focused on the ToF-SIMS results and their implications in nuclear waste disposal context.

2. Experimental

2.1. Sample preparation and exposure to simulated groundwater

Hot-rolled OFP-Cu, the material for making the canister, was used as the material for the experiments. The OFP-Cu was provided by Posiva Oy, Finland. The copper material had a typical hot-rolled microstructure, with large grains (from several tens to hundreds of micrometres in size) and annealing twins, see Fig. 1. Two initial conditions were used in the long exposure experiments: (*i*) the polished Cu surface, and (*ii*) pre-oxidised Cu surface that was after equal grinding exposed for seven days to air at the temperature of 90 °C. The samples had the dimensions of 10 mm × 10 mm × 3 mm, the surface was wet-ground down to 600 grits, and cleaned in acetone and ethanol prior to the exposure. The pre-oxidation was done to simulate the effect of initial oxic conditions at the elevated temperature on Cu, prior to anoxic phase in disposal. The elevated temperature was chosen to take into account the effect of radiation from the spent fuel. Highly radioactive nuclear waste repositories may exhibit significant temperature variations depending on their location, time, and type of waste, a temperature increase up to 90 °C is predicted within 10–30 years after closure, followed by a slow temperature decrease to natural condition in thousands of years [6,8].

The exposures were conducted at VTT using simulated groundwater with and without additional sulfide. Table 1 gives the chemical composition of the groundwater, which was derived based on the groundwater chemistry of the planned disposal site and the effect of ion exchange with the bentonite. The sulfide was added in the form of Na_2S. Besides sulfide addition, the groundwater contains a high level of chloride and sulphate ions. The experiments were mostly conducted at room temperature (22 °C) in glass vessels, while some samples were exposed at 60 °C in glass vessels placed in a heat chamber. The test vessels were gas-tight laboratory glass bottles with the volume of 5 L. The experiments were carried out in anoxic environment: the water and vessels were flushed with argon before the start of the tests. Vessels were sealed with butyl rubber stoppers to prevent O_2 contamination during the experiment. Redox potential monitoring and chemical analysis of the groundwater were performed to verify that anoxic nature of test system was maintained over the test duration. The exposure at 60 °C was done replicating the period of increased temperature in the early period of disposal. After the exposure, the samples were dried in air and then stored in desiccator. Exposure runs with different levels of added Na_2S and time durations, electrochemical measurements and characterization of the corrosion products were reported in the final project report [34]. The samples after exposure to the groundwater without/with 0.001 M (32 mg/L) Na_2S addition were chosen for ToF-SIMS analysis.

Table 1
The chemistry of the simulated groundwater, to which 0.001 M Na_2S was added.

	K	Ca	Cl	Na*	SO_4	Br	HCO_3	Mg	Sr	Si	B	F	Mn	PO_4	lactate
mg/L	54.7	280.0	5274.0	3180.2	595.0	42.3	13.7	100.0	8.8	3.1	1.1	0.8	0.2	0.1	1

* Original Na content; actual amount also includes the addition of Na_2S.

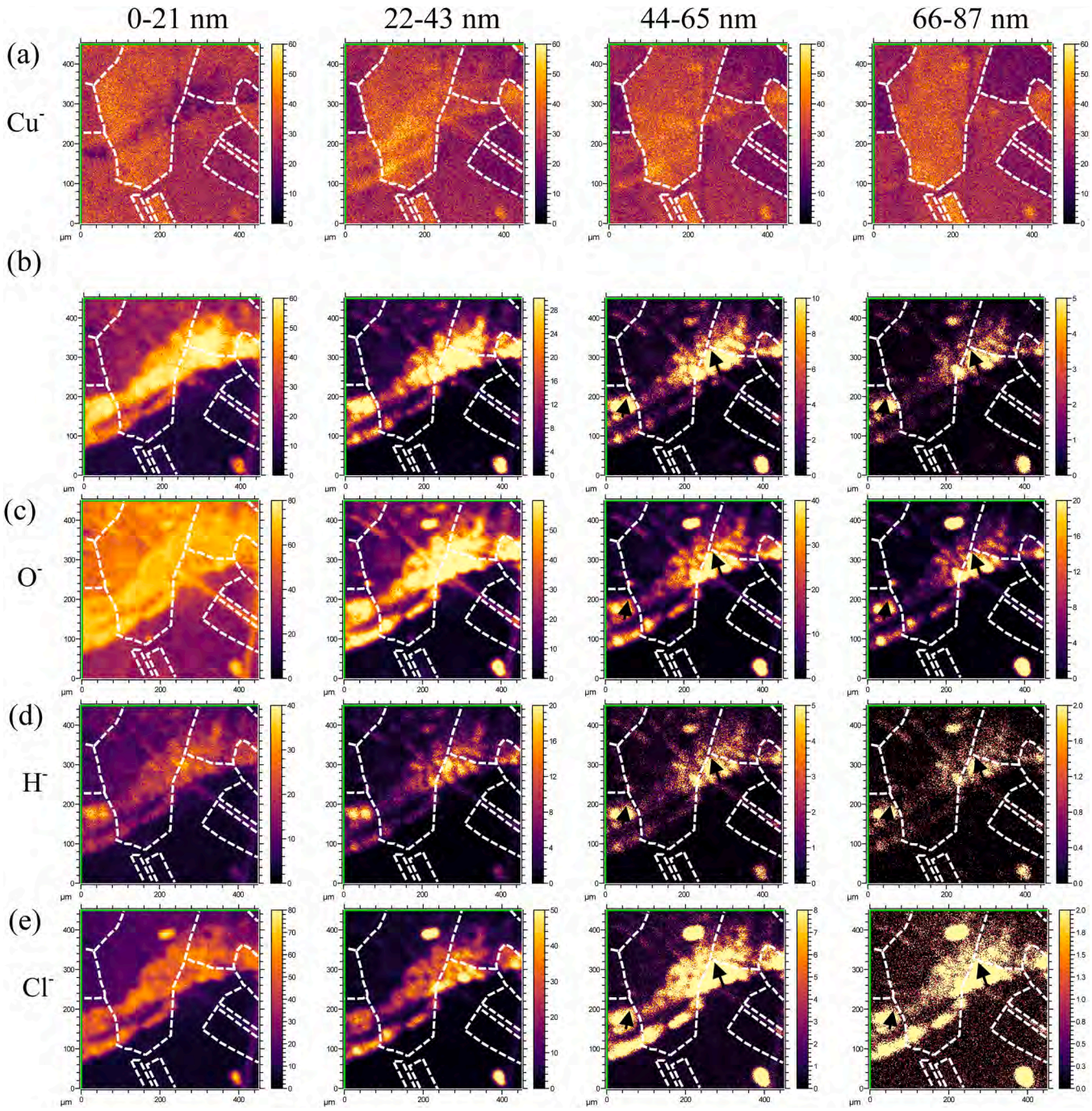

Fig. 2. Plane views by ToF-SIMS analyses at different depth intervals (0–21, 22–43, 44–65 and 66–87 nm) of a polished Cu sample after 9-month exposure in the simulated groundwater without Na_2S, at ambient temperature. (a) Cu^-, (b) S^-, (c) O^-, (d) H^-, and (e) Cl^-. The field of view is 450 μm × 450 μm. Arrows mark the segregation along the grain boundaries.

2.2. ToF-SIMS measurements

ToF-SIMS analyses were performed for selected Cu samples after the exposure. Before the analysis, the exposed samples were stored in desiccator for a long time: 1 year for the 9-month exposed samples and 0.5 year for the 4-month exposed samples. ToF-SIMS techniques including depth profiling and 2D/3D imaging, and their applications in material science have been described in literature [35–38]. ToF-SIMS has been extensively used to study high temperature oxidation mechanisms of alumina formers [39,40] and corrosion processes of engineering alloys [41–43]. In two SKB reports, ToF-SIMS measurements were included in the study of corrosion of Cu in O_2-free pure water, however, only depth profiles were briefly discussed regarding the estimate the thickness of the oxide film, while no 2D/3D imaging was made to map the distribution of the corrosive species inside the Cu metal [44,45]. In our work, ToF-SIMS measurements were performed at the Infrastructure for Chemical Imaging at Chalmers University of Technology, using a ToF-SIMS V instrument (ION-ToF, GmbH, Münster, Germany) equipped with a 25 keV Bismuth LMIG (Liquid metal ion gun) and a 10 keV Cs sputter gun providing high precision information on the composition of the elements, with a mass resolution m/Δm: 6000, and focus of the ion beam: 1–2 μm. The sputtered area was 650 μm × 650 μm (at 256 × 256 pixels), while the data from the central part of 450 μm × 450 μm were used for quantitative analysis to avoid possible edge effects.

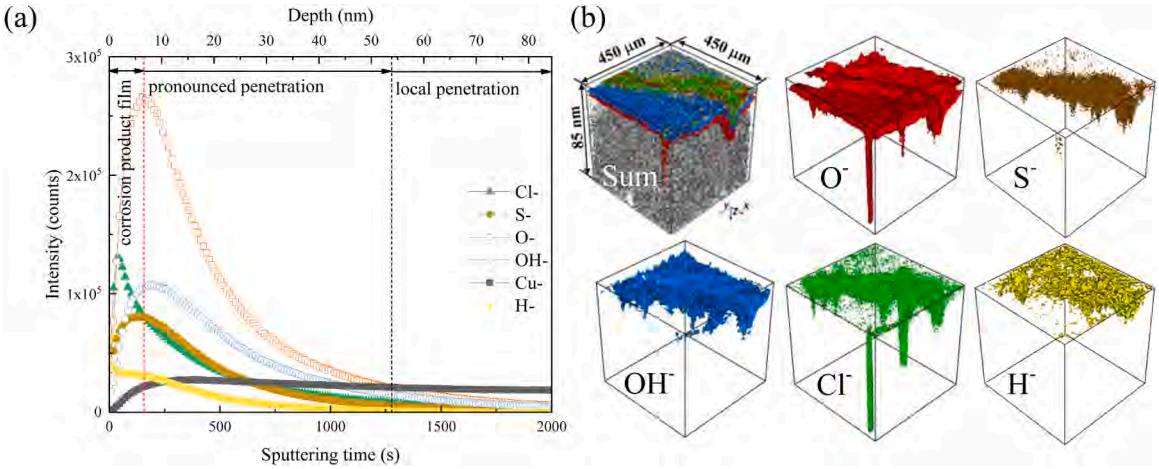

Fig. 3. (a) ToF-SIMS ion depth profiles, and (b) reconstructed ToF-SIMS 3D images of concentrated corrosive species in the volume including all the analysed areas in Fig. 2. The signal of OH^- is also included to show the presence of OH species in the corrosion products.

The signals of detected negative ions were used for plotting the depth profiles (in-depth variation of total counts over analysed area) and for construction of 2D/3D images (lateral distribution at certain depths). Both depth profile and image analyses were performed using the ION-ToF Surface Lab software (Version 6.3, ION-ToF, GmbH, Münster, Germany). The same instrument and software were used in corrosion studies as reported in previous publications [42,43]. With the setup used, the lateral resolution for imaging is ca. 0.5 μm. The mass resolution remained well above 4500–5000 with well-shaped gaussian peaks for all the elements shown in the paper, which indicates a reliable interpretation of the the ToF-SIMS data without any considerable effect of artifacts, particularly the role of topography, porosity, cracks, etc. The sputtering rate was 0.042 nm/s, determined by measuring the total depth of sputter crate using a white light interferometer (Zygo NewView7300). Note that the sputtering rate may vary slightly between the corrosion product layer and Cu matrix. However, this does not affect the discussion focusing on the penetration of the corrosive species inside the Cu matrix.

3. Results and discussion

Analysis of the ToF-SIMS data from the Cu samples provides depth profiles, revealing in-depth variations in the content of the corrosive species, and sequences of 2D images at different depths as well as 3D images of the analysed volume, showing their lateral distribution at different depth intervals. As a common practice, the signal intensity (count) vs. sputtering time is plotted in the depth profiles, and the depth value converted from the sputtering time is also added to the plots. Note that the intensity of Cu is relatively low because the ionization yield of Cu (metallic and oxidized) is much lower than that of H, S, O, and Cl due to a lower relative sensitivity factor (RSF) in ion sputtering processes. Whereas, the RSF is similar for S, H, and Cl, and somewhat higher for O, as reported in literature [35]. Ideally, the interface between the Cu metal substrate and corrosion product film is defined at the point of the rapid raise of the metal signal and the drop of the signal of corrosive species. However, it is not straightforward in this case, because some Cu grains were more corroded than others, causing uneven penetration of the corrosive species into the Cu substrate. In fact, there is no sharp boundary at the interface, therefore we define the interface at the point when the Cu signal increased to a stable level and where the signal of O or S species also started to decrease, similar to the literature report [41]. In the 2D images, the colour contrast shows the variation of the signal intensity, which indicates the difference in the concentration in a relative scale. In the 3D images, the Z-axis (depth) is not in proportion to the X and Y axes but scaled to demonstrate the changes in the distribution of corrosive species, to ease the visualization of their penetration into the Cu substrate. Note that some 3D images are included in the supplementary material.

3.1. Corrosion of Cu in simulated groundwater without Na_2S

Figs. 2 and 3 display the ToF-SIMS results from a polished sample after 9-month exposure in the simulated groundwater without Na_2S, at ambient temperature. Fig. 2 presents 2D images of Cu^-, S^-, O^-, H^- and Cl^- acquired at different depth intervals (0–21, 22–43, 44–65, and 66–87 nm) below the surface, showing lateral distribution of Cu, S, O, H and Cl in the surface and near-surface regions. The 2D images are sum frames constructed by combining individual planes obtained within certain sputtering time intervals, from which the depth ranges were calculated using the sputtering rate. To visualize the Cu grains and in some cases also the annealing twins (parallel lines), broken lines were added in the images to illustrate the grain boundaries. The sequence of the 2D images manifests the progress of the corrosion of Cu from the surface towards the interior microstructure. As seen in Fig. 2, the 2D images at all depths show some areas of higher intensity of S^-, O^-, H^-, and Cl^-, however, the intensity of Cu^- varies only slightly in these areas, indicating that the intensity variation of Cu^- is mainly originated from the different orientations of the Cu grains. Areas of lower Cu^- intensity (seen in darker contrast) are associated with the corrosion products, which could be seen only in the depth range of 0–21 nm. The correlation between the high intensity areas (seen in bright contrast) of S^-, O^-, H^-, and Cl^- indicates the joint actions of these corrosive species, and their local segregation shows nonuniform nature of the corrosion process. The corrosion products formed on the surface likely contained oxides and sulphates, probably also hydroxides and Cl-containing compounds. Thanks to the high sensitivity to detect hydrogen, the ToF-SIMS measurement revealed the distribution of H, not only in the corrosion product on the surface, but also inside the Cu microstructure (Fig. 2(d)).

Fig. 3 displays depth profiles (Fig. 3(a)) and 3D topographical images (Fig. 3(b)) for the groundwater-exposed Cu sample at a 450 μm raster size (field of view: 450 μm × 450 μm) constructed by concatenating ToF-SIMS data of concentrated corrosive species. Six signals are included in Fig. 3, the Cu^- is originated from the Cu metal and other signals represent corrosive species originating from the exposure environment. The increase of Cu^- ions was used for characterizing the matrix because the intensity of Cu^- is higher than that of Cu^{2-}, which can provide a better resolution. Based on the depth profiles of Cu^- and O^-, the thickness of the corrosion product film is estimated to be ca. 7 nm (Fig. 3(a)). This is in reasonable agreement with the average corrosion rate determined by the weight loss measurements, which include the dissolved part [34]. The

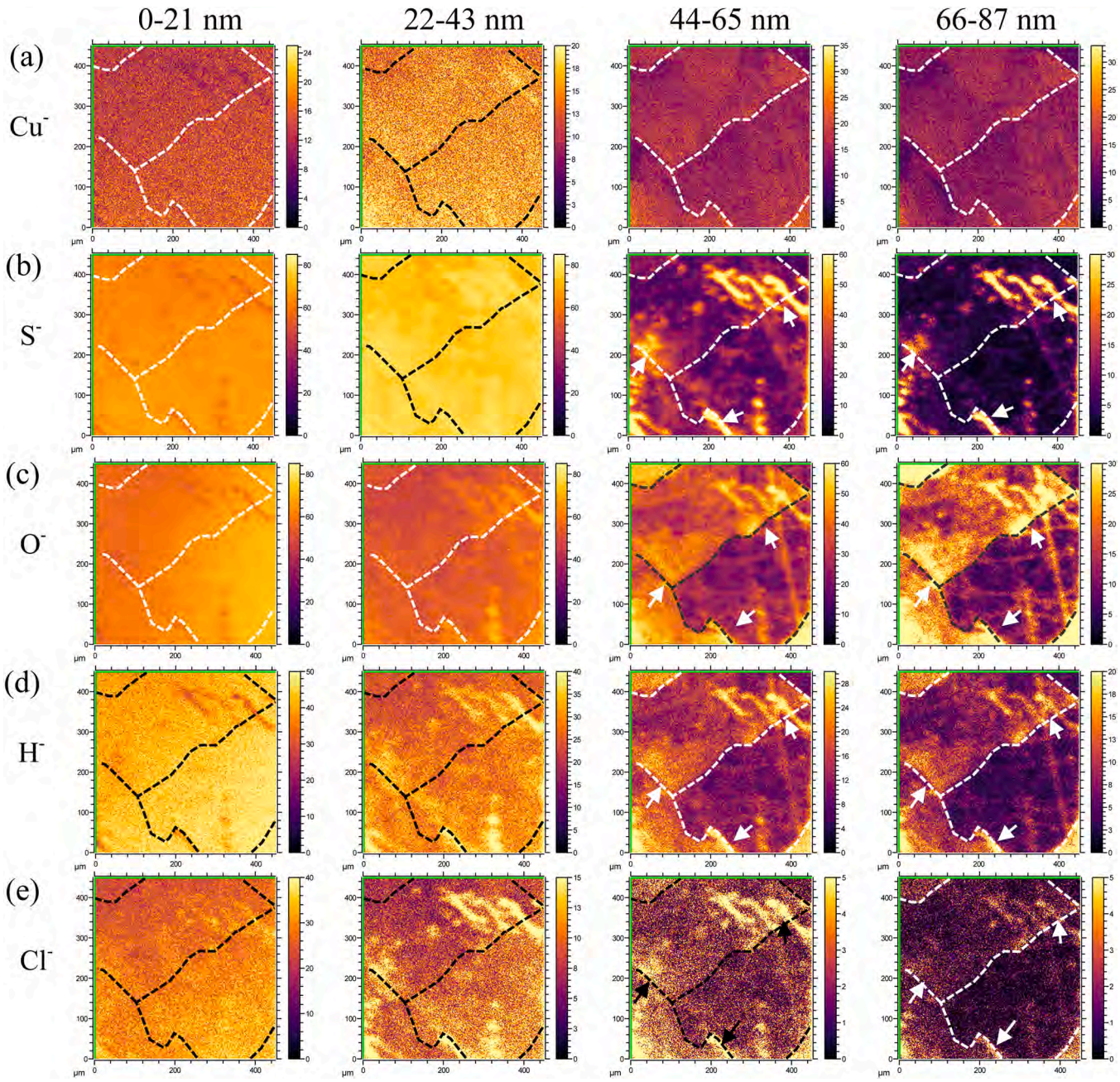

Fig. 4. Plane views by ToF-SIMS analysis at different depth intervals (0–21, 22–43, 44–65 and 66–87 nm) of a polished Cu sample after 9-month exposure in the simulated groundwater with 0.001 M Na_2S, at ambient temperature. (a) Cu^-, (b) S^-, (c) O^-, (d) H^-, and (e) Cl^-. The field of view is 450 μm × 450 μm. Arrows mark the segregation along the grain boundaries.

depth profiles show pronounced penetration of the corrosive species reaching the depth of 55 nm. Moreover, further local penetration of the corrosive species can be seen as continuously decreasing intensities with sputtering time in the logarithmic plot (supplementary Fig. S1). The pronounced penetration refers to the depth range with substantially higher contents (reflected by signal intensity) of the corrosive species distributed in a large part of the matrix, while local penetration refers to the depth range where the detected singal of the corrosive species persists and decreases with increasing depth, but still higher than the background level. The small magnitude of signal intensity beyond the background level indicates the deep penetration occurring only at some local sites. The boundary between "pronounced penetration" and "local penetration" is defined from the decline of S^-/O^- signal and the relatively stable Cu^- signal to their intersection, as shown in the depth profile plots.

The 3D images (Fig. 3(b)) visualize the corrosion product layer and local deep penetration of corrosive species (especially O and Cl) into the Cu microstructure. High level of O is seen throughout the corrosion product layer, whereas high levels of S, Cl, OH, and H are seen in some local areas. The results suggest the formation of heterogeneous corrosion products consisting of oxides/hydroxides as well as S- and Cl-containing compounds.

The sites with the deep penetration of O and Cl likely represent some grain boundaries in the microstructure. However, the width of the deep penetration channels is quite large (up to tens of μm), see Fig. 3(b), indicating the significant extent of intergranular corrosion. The ToF-SIMS results demonstrate that the Cu corrosion takes place not only through surface reactions but also through penetration of corrosive species into the Cu substrate. Without any sulfide addition, the corrosion

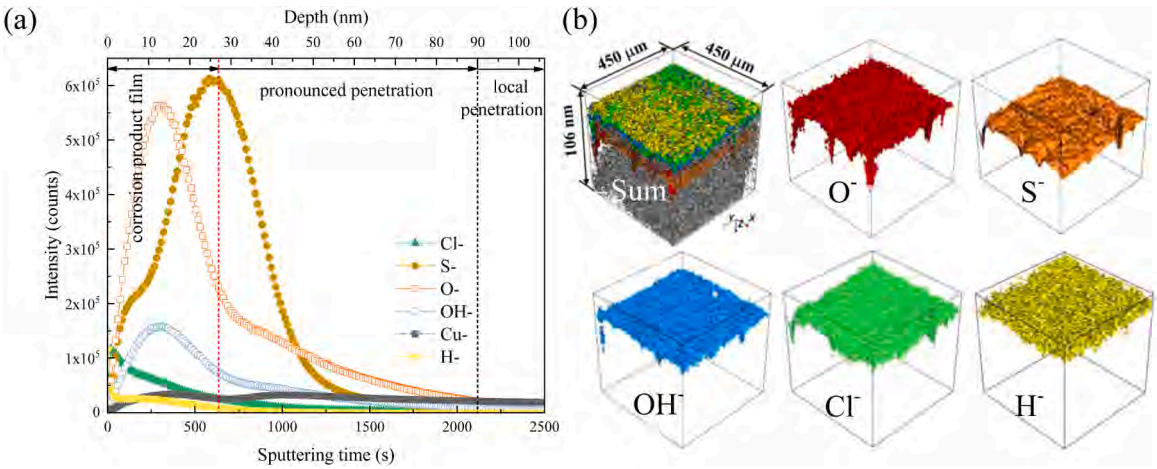

Fig. 5. (a) ToF-SIMS ion depth profiles, and (b) reconstructed ToF-SIMS 3D images of concentrated corrosive species in the volume including all the analysed areas in Fig. 4.

product layer formed on the surface is quite thin, however, the corrosion process is not uniform and local penetration of corrosive species into the Cu substrate is evident. Estimation of the penetration depth of the corrosive species, in particular S, into the Cu substrate and the implications are discussed in the summary section below.

3.2. Corrosion of Cu in simulated groundwater with 0.001 M Na_2S

Figs. 4 and 5 display the ToF-SIMS results obtained for a polished sample after 9-month exposure in the simulated groundwater with 0.001 M Na_2S, at ambient temperature. Fig. 4 presents 2D images of Cu^-, S^-, O^-, H^- and Cl^- acquired at different depth intervals below the surface, showing the lateral distribution of Cu, S, O, H and Cl in the surface and sub-surface regions, while Fig. 5 displays depth profiles and 3D images of concentrated corrosive species distributed in the entire analyzed volume. The depth intervals are chosen to be the same as those in Figs. 2 and 3 for easy comparison. It can be seen in the 2D plane views that these corrosive species, especially S and O, are present in the whole surface layer in the depth range of 0–43 nm, evidenced by the strong intensity over the whole area. Such behaviour was not detected in the absence of sulfide. With the depth exceeding 43 nm, the overall intensity for S^-, O^-, Cl^-, and H^- decreases and becomes uneven over the analysed area, indicating local segregation of the corrosive species. The distributions of S, O, Cl, and H reveal similar features, suggesting the joint action of these corrosive species. However, in the depth range of 44–87 nm, S distribution is essentially concentrated in local spots and lines (marked as arrows), whereas O distribution seems to reflect the grain orientations. The distribution of H resembles that of both O and S, and Cl level becomes very low. These findings indicate that there is some difference between these species in the local penetration and segregation in Cu microstructure. The segregation along the lines may be associated with the grain boundaries, and some of them may become preferential corrosion pathways as observed in previous studies [10, 11, 51]. These features are very different from those in the absence of sulfide, indicating its important role in the development of corrosion products and the progress of corrosion into the Cu metal.

Fig. 5 shows a thicker corrosion product film formed on the surface and also significantly enhanced penetration of the corrosive species into the Cu microstructure as compared to the case without sulfide (Fig. 3). The depth profiles in Fig. 5(a) show higher intensity of Cl^- and H^- in the outmost layer (several nm in depth), and the maximum intensity of O^- and OH^- around 12 nm. The outmost layer mainly contains oxides and hydroxides, and adsorbed species from the solution and surface contamination may also be present in this layer. The peaks of O^- and OH^- indicate the position of the oxide/hydroxide layer. Interestingly, the signal of S^- reached a maximum at the depth around 27 nm, where the intensity of O^- and OH^- decreased to a low level. Judged by the depth of maximum intensity of S^- and increased intensity of Cu^-, the thickness of the corrosion product film is estimated to be 27 nm, which is much thicker than that of the sample exposed to the groundwater without Na_2S (Fig. 3(a)). Pronounced penetration of corrosive species reached the depth of 90 nm, see Fig. 5(a), and futher local deep penetration (>106 nm) can be seen in the logarithmic plot (supplementary Fig. S2). The 3D images in Fig. 5(b) visualize the corrosion products formed on the surface, heterogenous distribution and local penetration of the corrosive species in the Cu metal. Deep local penetration is seen to follow some fast paths, seemingly along the grain boundaries, as shown in Fig. 4.

These results indicate that the corrosion product film consists of an O-rich outer layer and S-rich inner layer. The outer layer of oxide/hydroxide could be formed during the storage time after the sample was taken out from the O_2-free groundwater. The formation of a relatively thick S-rich layer on the Cu metal suggests a fast S-induced corrosion during the exposure to the O_2-free groundwater with 0.001 M Na_2S, which also leads to the significantly enhanced penetration of the corrosive species into the Cu microstructure, in particular along some fast paths. It should be mentioned that the open circuit potential value for Cu remained below - 0.8 V vs. Ag/AgCl during the entire period of exposure, indicating the reducing condition (O_2-free) of the exposure environment. Thermodynamically, this suggests the formation of copper sulfide as the main corrosion product [34]. Besides, the thickness of the corrosion product layer, ca. 27 nm, indicates that it is not a traditional passive film like that on stainless steels with the thickness of a few nm.

3.3. Effect of pre-oxidization

Figs. 6 and 7 display the ToF-SIMS results obtained for a pre-oxidized sample after 9-month exposure in the simulated groundwater with 0.001 M Na_2S, at ambient temperature. Fig. 6 presents 2D images of Cu^-, S^-, O^-, H^- and Cl^- acquired at different depth intervals from the surface, the plane views show lateral distribution of Cu, S, O, H and Cl in the surface and sub-surface regions. The pre-oxidized sample has an initial oxide film on the surface. In the surface layer (0–21 nm in depth), O is present and distributed uniformly. The O level increases towards the near-surface areas, down to the depth of 65 nm, and then decreases with increasing depth. In contrast, high level of S is present in the surface layer (0–21 nm), locally concentrated in specific grains and lines, but the level decreases with increasing depth. In the depth range of 66–87 nm, where the O intensity was lower, an increased level of S was detected again, being located in specific grains and lines. Only minor

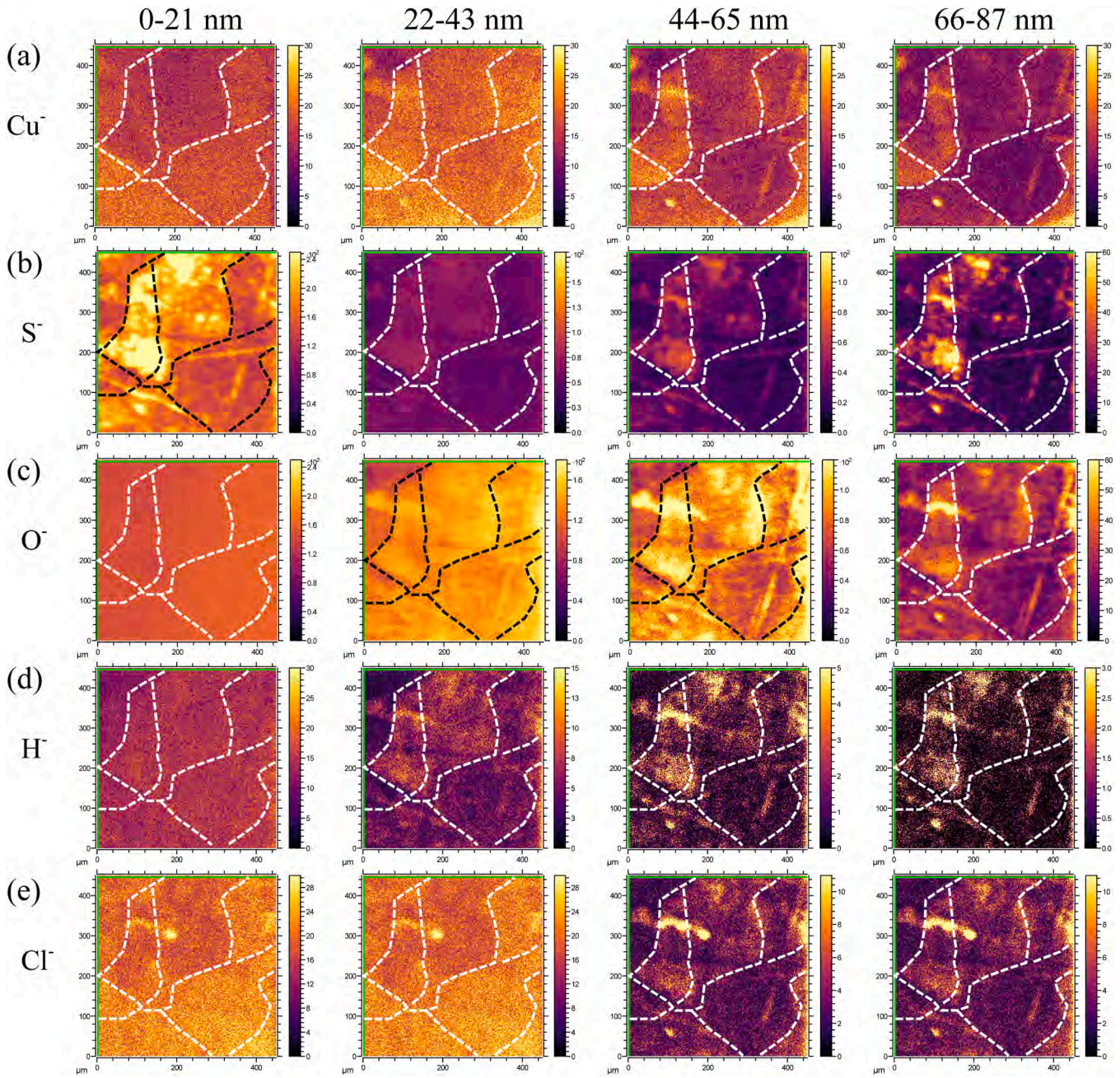

Fig. 6. Plane views by ToF-SIMS analysis at different depth intervals (0–21, 22–43, 44–65 and 66–87 nm) of a pre-oxidised Cu sample after 9-month exposure in simulated groundwater with 0.001 M Na_2S, at ambient temperature. (a) Cu^-, (b) S^-, (c) O^-, (d) H^-, and (e) Cl^-. The field of view is 450 μm × 450 μm.

levels of Cl and H were detected, being locally distributed, especially at increased depths. In this case, local penetration of the corrosive species are clearly seen in the depth range of 44–87 nm. In many sites, O and S are segregated together, and even H and Cl are seen to co-exist at some sites.

Fig. 7 displays the depth profiles of the corrosive species for a pre-oxidized sample after 9-month exposure in the simulated groundwater with 0.001 M Na_2S, at ambient temperature. The depth profiles show that the O^- peak is much higher and broader than the S^- peak. Judged by the depth of maximum S^- intensity and increased Cu^- intensity, the thickness of the corrosion product film is estimated to be ca. 25 nm, similar to that of the polished sample. Nevertheless, in this case, the depth profiles of O^- and S^- are very different from those of the polished sample (Fig. 5(a)), which has a S-dominant layer beneath the O-dominant layer. This indicates the effect of the initial oxide on the sulfide-induced corrosion process, i.e., the presence of initial oxide film reduces the sulfide-induced corrosion to some extent. However, despite of a lower intensity, the S^- peak is located slightly deeper than the O^- peak (Fig. 7). It suggests that localized S penetration can occur through the oxide film, evidenced by the similar local segregation in the surface layer (0–21 nm in depth) and inside the Cu substrate (66–87 nm in depth), see Fig. 6(b). The heterogenous corrosion products, the pronounced penetration of the corrosive species into the Cu substrate down to the depth of 147 nm, and further local penetration can be viewed in the 3D images and the log plot of depth profiles (supplementary Fig. S3). These results indicate that the exposure of the pre-oxidized sample to the anoxic groundwater with 0.001 M Na_2S results in both the formation of O- and S-rich compounds on the surface and also penetration of the corrosive species into the Cu microstructure, despite the presence of an initial oxide film on the surface. The corrosive species seem to have some

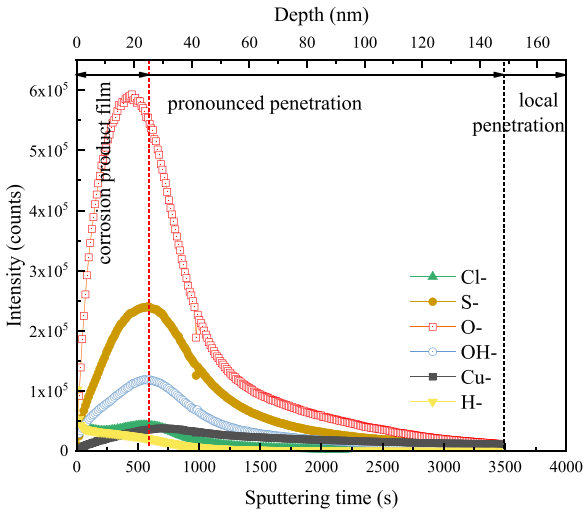

Fig. 7. ToF-SIMS ion depth profiles of concentrated corrosive species in the volume including all the analysed areas in Fig. 6.

joint actions that promote their penetration into the Cu microstructure.

3.4. Effect of elevated exposure temperature of 60 °C

Figs. 8 and 9 display 2D images obtained from two pre-oxidized samples after 4-month exposure in the simulated groundwater with 0.001 M Na_2S, one at ambient temperature (22 °C), and another at 60 °C. The total sputtering time is 2500 s for the sample exposed at ambient temperature and 12000 s for the one exposed at 60 °C, respectively. The latter was much longer because of a much deeper penetration of the corrosive species. In Fig. 8(a), the contrast in Cu^- intensity reflects the different crystallographic orientations of the grains (with different atomic packing densities). The S^- and O^- signals are strong and quite uniform in the surface layer (0–25 nm in depth), and decrease in the overall intensity with increasing depth. Beyond 25 nm, S^- and O^- signals show localized high intensity, indicating their joint penetration into the Cu microstructure. The H^- and Cl^- signals, although relatively weak, were also detected within the Cu metal, mostly appearing as small spots located along and in the vicinity of the grain boundaries. These small spots are likely the trapping sites of H and other corrosive species. Local deep penetration of the corrosive species, seemingly along grain boundaries, can be viewed in the log plot of depth profiles and the 3D images (supplementary Fig. S4(a) and (c)).

For the sample exposed to Na_2S-added groundwater at 60 °C, because of a thicker corrosion product film and deeper penetration of corrosive species, larger depth intervals are used for constructing 2D images, see Fig. 9. The contrast in Cu^- intensity reveals high-angle boundaries (added broken lines), which are likely high-angle grain boundaries and twins. The S^- images show a high level of S uniformly distributed down to the depth of 250 nm, while it is concentrated along the lines at greater depths, consistent with the Cu^- images. The O^- intensity from the surface down to 250 nm is much lower than for S^-, but consistent trends are seen for S^- and O^- images obtained at greater depths. In the S^- and O^- images for the depth range of 376–500 nm, lines with relatively high signal intensity are seen inside large grains, which are likely associated with the grinding scratches (with residual strain and concentrated dislocations) on the sample. Overall, the S^- signal has the highest intensity in the whole analysed area down to the depth of 375 nm, suggesting that S is the dominant corrosive species in the corrosion product film. Local enrichment of the corrosive species is seen in the depth range of 250–375 nm, and their segregation along the lines and at many spots was detected in the depth range of 376–500 nm. Interestingly, the spots appear as being connected along certain lines, which may be associated with a large extent of segregation along the grain and sub-grain boundaries. The heterogenous corrosion products on the surface and local deep penetration of the corrosive species can be viewed in the log plot of depth profiles and the 3D images (supplementary Fig. S4(b) and (d)).

For comparison, the depth profiles for the two samples are plotted in Fig. 10. In both cases, S^- has a higher intensity than O^-, and the S^- peak is broader than the O^- peak. Obviously, the corrosion product film is much thicker and the penetration of the corrosive species is much deeper for the sample exposed at 60 ℃ than the one exposed at ambient temperature. Judged from the O^-, S^-, and Cu^- profiles, the thickness of the corrosion product film is estimated to be ca. 25 nm for the sample exposed at ambient temperature, while it is around 170 nm for the sample exposed at 60 °C. It is striking that the high intensity of S^- extends deep into the Cu substrate when exposed at 60 °C. Pronounced penetration of S reached the depth of 440 nm (Fig. 10(b)), while the local penetration along grain boundaries is likely much deeper. Clearly, the sulfide-induced corrosion of Cu in the anoxic groundwater is greatly accelerated by increasing the exposure temperature to 60 °C, and the ingress of the corrosive species, especially S, is largely promoted by the increased temperature.

4. Overall discussion and implications of the results

In this work, after the exposure runs, the Cu samples were stored in desiccators for a long time and then in air for many days before the ToF-SIMS analysis. During the storage in air, conversion of some part of sulfides to oxides is possible due to oxidation. Meanwhile, surface adsorption and contamination may occur during this period leading to modification of the outermost layer (a few nm thick). Moreover, due to the large Cu grains, up to a few hundreds of μm in size, the analysed area (450 μm × 450 μm) may only include a small number of grains, so caution should be taken in quantitative comparison between the samples. Furthermore, the sample surface area selected for ToF-SIMS analyses were relatively smooth, without visible porosity and cracks. The morphology of the corrosion scale is shown in Fig. S5. The results show detectable levels of the corrosive species in all cases, and some other areas may have even higher levels. The 2D images and linear plots of the depth profiles reveal pronounced penetration of the corrosive species, while the depth of local penetration is much deeper in some cases, judged by the logarithmic plots (highlighting small changes). To determine the local penetration depth requires long sputtering times until reaching the depth where the corrosive species is reduced to the background level. Since H atoms are highly mobile even at ambient temperature, part of atomic H entering into the Cu during the exposure in the groundwater may have egressed from the sample during the storage time before the ToF-SIMS analysis. Thus, the detected H is only the trapped part. Accurate quantitative measurement of H requires freezing the sample before the measurement, and Nano-SIMS with nm lateral resolution is needed to resolve H segregation along grain boundaries. The ToF-SIMS data presented here are given in counts/intensity, showing the variations on a relative scale. Nevertheless, the ToF-SIMS results, showing both the depth profiles including in-depth variations and penetration of the corrosive species into the Cu substrate, and the 2D/3D images showing uneven distribution and local segregation of the corrosive species within the Cu microstructure, provide valuable information about the corrosion processes occurring not only on the Cu surface, but also inside the Cu microstructure. This information is often missing in corrosion studies.

The ToF-SIMS depth profiles of the corrosive species often show a peak followed by slow decay of the signal intensity with sputtering time. The high levels of S and O, together with a lower level of Cu, is associated with a S- and O-rich corrosion product film formed on the surface, while the slow decay of the corrosive species indicates their penetration into the Cu substrate. Deep penetration is seen to occur along some fast paths, e.g., grain boundaries, Figs. 2 and 4. The 2D images clearly show that locally concentrated S, O, H, and Cl often overlap in the same areas

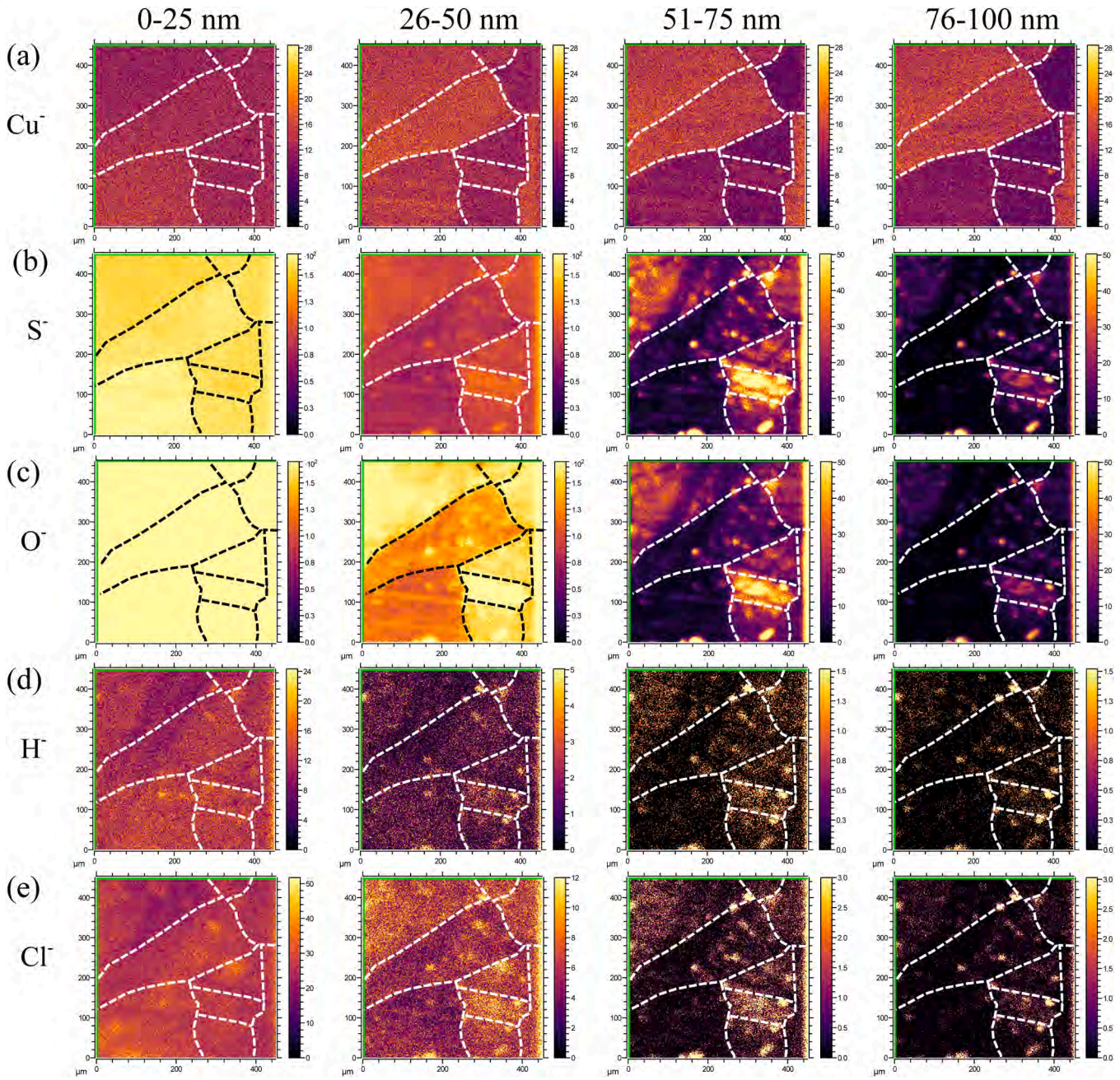

Fig. 8. Plane views by ToF-SIMS analysis at different depths (0–25, 26–50, 51–75, and 76–100 nm) of a pre-oxidised Cu sample after 4-month exposure in the simulated groundwater with 0.001 M Na_2S, at ambient temperature. (a) Cu^-, (b) S^-, (c) O^-, (d) H^-, and (e) Cl^-. The field of view is 450 μm × 450 μm.

or sites, suggesting their joint action in the corrosion process. An initial oxide film, either formed due to exposure in air or during pre-oxidation, was present on the surface before the exposure to the groundwater. During the long-term exposure to the simulated anoxic groundwater, the initial oxide film does not seem to prevent the transport of corrosive species and further corrosion of the metal. The results in Figs. 2 and 3 show that, without Na_2S addition, a thin oxide/hydroxide layer remained on the surface after the exposure, and local penetration of S, O, H, and Cl into Cu substrate occurred, seemingly along grain boundaries. In this case, the S originates from SO_4^{2-}, and Cl from Cl^- ions, both of which were involved in the corrosion process. In the presence of Na_2S (0.001 M), the corrosion was significantly accelerated, evidenced by a thicker corrosion product film formed on the surface and the enhanced penetration of the corrosive species, especially S, and deep local penetration into the Cu substrate (Figs. 4 and 5). The correlation between S^- and CuS^- in the depth profiles (Fig. S6) suggests that the S-compound in the S-rich corrosion products formed on the surface is most likely Cu sulfide [34].

Comparison of the results from the polished and pre-oxidized samples shows the effect of the pre-oxidation. On the polished sample, the corrosion product film consists of an O-rich outer layer and a S-rich inner layer (Fig. 5). Whereas, on the pre-oxidized sample, the corrosion product film contains mixed O- and S-compounds (oxides and sulfides), in which the O-compounds are dominant (Fig. 7). In both cases, significant penetration and local segregation of S, O, H, and Cl in the Cu microstructure occurred (Figs. 4 and 6). These results indicate that the initial oxide film formed during the pre-oxidation did not act as a dense barrier to impede the sulfide-induced corrosion, and S-species could easily penetrate the initial oxide film. Probably, the initial oxide film is defective or soluble in the groundwater, which allows easy penetration

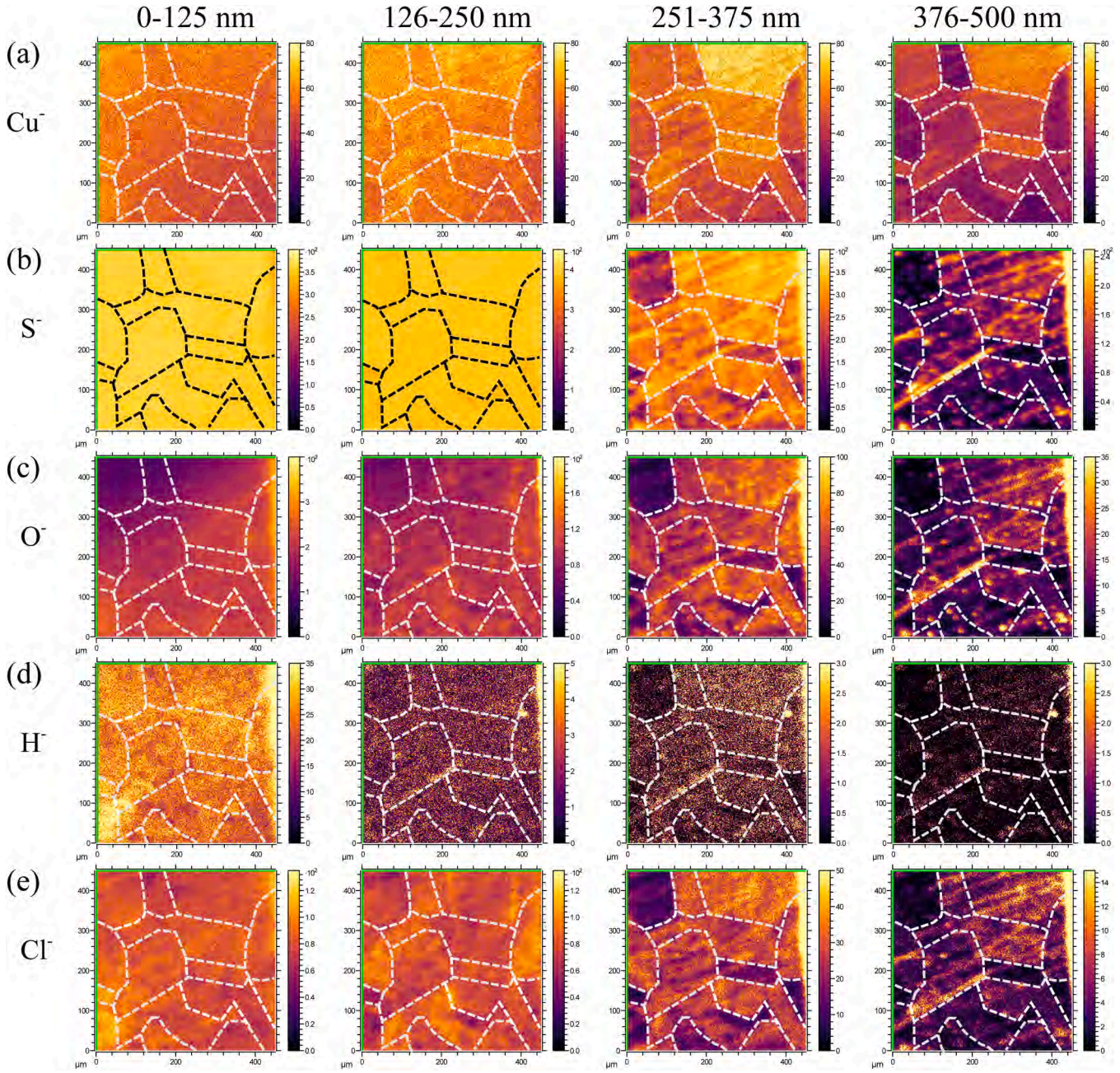

Fig. 9. Plane views by ToF-SIMS analysis at different depths (0–125, 126–250, 251–375, and 375–500 nm) of a pre-oxidised Cu sample after 4-month exposure in the simulated groundwater with 0.001 M Na_2S, at 60 ºC. (a) Cu^-, (b) S^-, (c) O^-, (d) H^-, and (e) Cl^-. The field of view is 450 μm × 450 μm.

of the S-species. In fact, the presence of a discontinuous oxide film, especially when containing oxide particles at the grain boundaries, facilitates hydrogen trapping [11]. Comparison of the results from the exposure at ambient temperature and at 60 °C show clearly that the increased temperature of 60 °C has a pronounced effect by accelerating the sulfide-induced corrosion, and the role of S-compounds is more enhanced than that of O-compounds. The thickness of the corrosion product film increased several times and the film became dominated by S-compounds (Fig. 10). Penetration of S and O into the Cu substrate was greatly promoted, and the local segregation of S, O, and Cl occurred more frequently and to a larger extent than at ambient temperature, appearing as continuous lines instead of discrete spots (Figs. 7 and 8). The local distribution of H is probably similar, but this needs to be confirmed by further Nano-SIMS analysis. The temperature effect on the penetration of S, O, and Cl into the Cu substrate can clearly be seen from the comparison of depth profiles in Fig. 11.

Thermodynamics and kinetics of Cu corrosion in pure water and simulated groundwater have been studied extensively, with respect to the deep geological disposal of nuclear waste [6,8]. Under anoxic condition, in the presence of sulfide, surface Cu-oxides will be transformed into Cu-sulfides [16,17]. DFT calculations of simple model systems suggest possible dissociation of H_2O and sulfide species and adsorption of O, H, and S on the Cu surface [18,19,46–49]. It has been claimed that ingress of H and S into the Cu lattice is not energetically favourable [32], based on the calculations showing possible formation of H_2 is some cases [47,48,50]. However, in real disposal system, high levels of Cl^- and SO_4^{2-} and also of sulfide species are present in the groundwater. Moreover, there are various types of defects on the Cu surface and inside the microstructure including dislocations, grain boundaries and voids. The ToF-SIMS results from this work demonstrate that, during exposure of

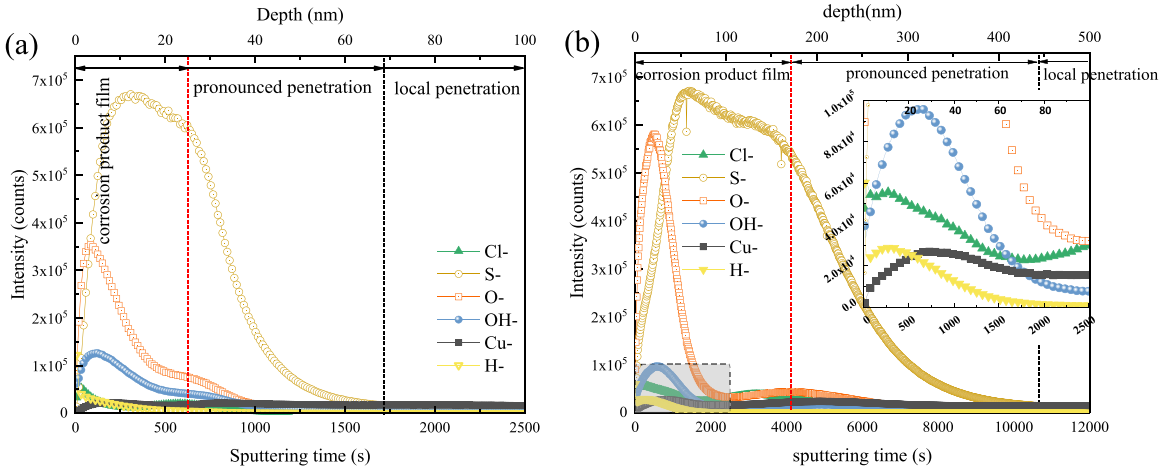

Fig. 10. ToF-SIMS ion depth profiles for the pre-oxidized Cu samples after 4-month exposure in the simulated groundwater with 0.001 M Na_2S, (a) at ambient temperature, and (b) at 60 ℃. Note the depth scale in (b) is 5 times of that in (a).

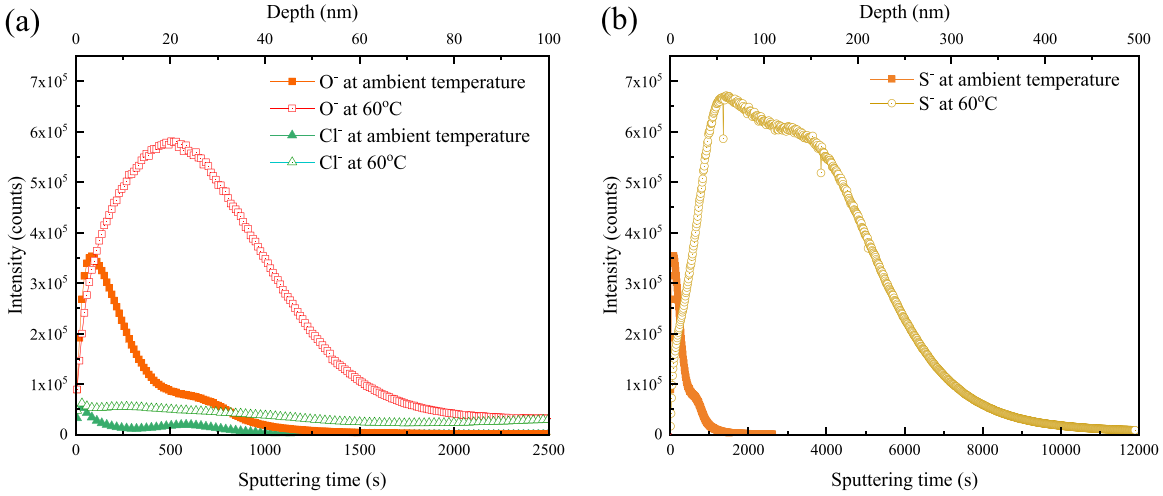

Fig. 11. ToF-SIMS ion depth profiles of (a) O^- and Cl^-, and (b) S^- on the samples after 4-month exposure in the simulated groundwater with 0.001 M Na_2S, at ambient temperature and 60 °C, respectively.

Cu samples to the groundwater, in addition to the formation of complex corrosion products on the surface, significant penetration of S, H occurs in the Cu microstructure, often observed with joint penetration of O and Cl. This local penetration of corrosion stimulating species down to the depth of several hundred nanometres along some fast paths occurs, even without added sulfide. Such local penetration suggests a severe underestimation of the corrosion risk of Cu when only considering the homogeneous corrosion processes. Furthermore, such penetration is enhanced by the sulfide addition. The elevated temperature of 60 °C greatly accelerates the corrosion on the surface and the penetration of corrosive species into the Cu substrate. Fig. 12 shows an illustration of the corrosion processes including the penetration of the S, O, H and Cl into the Cu microstructure.

The ToF-SIMS results provide clear evidence for the pronounced penetration of S, O, H and Cl into the Cu microstructure, which is heterogenous and seems to be related to the grain orientations. The grain-orientation effect on the corrosion process has also been observed by other measurements [34]. Deep penetration occurs via some fast paths, likely along some grain boundaries. These new findings provide reasonable explanations for the observations of sulfide-induced SCC and intergranular corrosion of Cu in similar environments [10,11,51]. The most striking observation is the pronounced penetration of S into Cu which is enhanced by the sulfide addition and greatly promoted by the elevated temperature of 60 °C. Based on the ToF-SIMS ion depth profiles and the 2D maps of the distribution of the corrosive species (in the grains and along the grain boundaries), the depth of pronounced penetration can be determined for the different samples. As can be seen in the log plots of the depth profiles, the depth of local penetration along grain boundaries exceeds the depth of termination of the ion sputtering. Taking the Cu sample after 4-month exposure to the Na_2S-added groundwater at 60 °C as an example, the results show that the pronounced S penetration (involving diffusion both within the grains and along the grain boundaries) reached the depth of 440 nm, whereas the depth of local penetration (along the grain boundaries) is beyond 500 nm. Assuming linear extrapolation it follows that the overall penetration rate of S is 1.32 μm/year and the rate of S penetration along grain boundaries is more than 1.5 μm/year. These rates can be used to estimate the time needed for S to penetrate the Cu metal under service conditions. Accordingly, it takes ca. 38 years and 38000 years for S to penetrate 50 μm and 5 cm thick Cu, respectively. Moreover, it takes less than ca. 33 and 33000 years for S to diffuse 50 μm and 5 cm, respectively, along the grain boundaries. These values can be compared with an SKB report compiling data of diffusion in Cu [58]. According to Figs. 3–5 in ref. 58, at 60 °C, it takes less than 1000 years for S to diffuse 5 cm in grain boundaries. In our ToF-SIMS measurements, the local S penetration along the grain boundaries could be much deeper than the

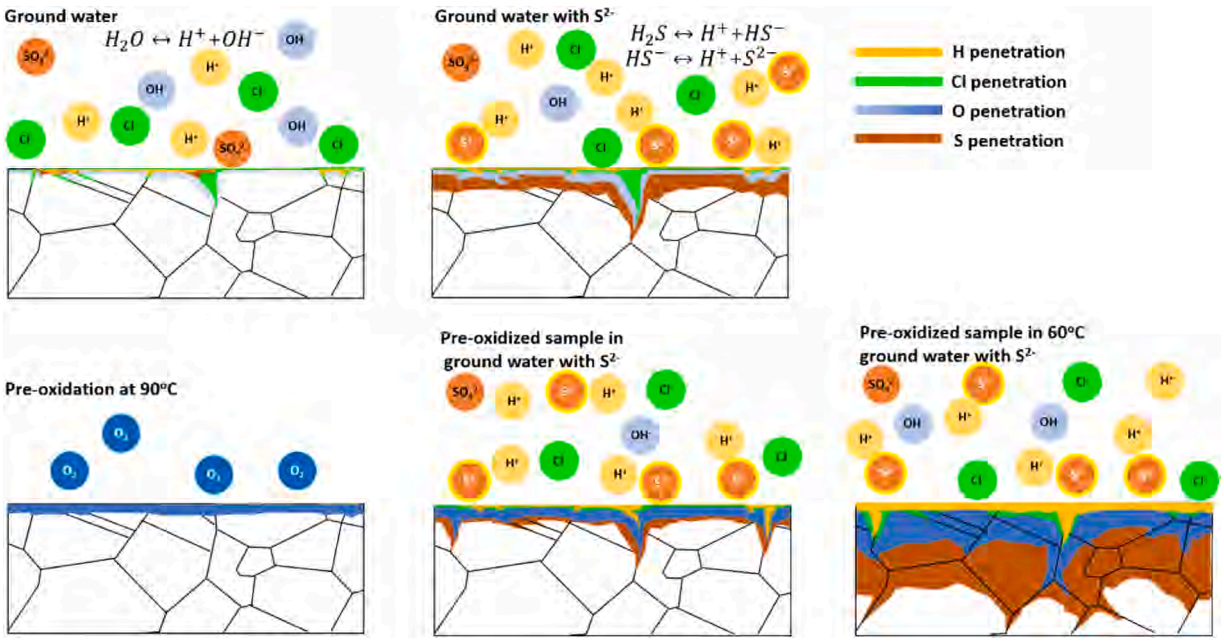

Fig. 12. Illustration of penetration of corrosive species into the Cu microstructure under different exposure conditions.

depth of termination of the ion sputtering, therefore our extrapolated results are in general agreement with the above calculation using the reported diffusion data [58]. The ToF-SIMS results demonstrate that the S penetration into the Cu microstructure and the local penetration along grain boundaries are indeed very fast under the experimental conditions.

To understand the mechanism of the internal corrosion and penetration of corrosive species inside the microstructure requires detailed knowledge at atomistic scale, typically acquired by DFT calculations. The joint actions of S and H, together with O and Cl, may have some synergistic effect on the corrosion process, which has not been addressed by DFT, although hydrogen trapping and sorption capacity was calculated for vacancy, void and grain boundaries in Cu [52–54]. A theoretical study of diffusion of dissociation products suggests that OH in a grain boundary of Cu quickly dissociates leading to fast diffusion of O and H atoms along the grain boundary [55]. Moreover, DFT calculations show that S and P tend to segregate and thus accumulate at a certain type of grain boundary in Cu [56]. In a study of impurity effects on the grain boundary cohesion in Cu, it has been found that a strong segregation of S can reduce the work (energy) of grain boundary separation below the work of dislocation emission, thus embrittling Cu, which is in agreement with experimental observations [57].

Our new findings have important implications regarding the risk for sulfide-induced SCC and embrittlement of the Cu canister. A comprehensive understanding of the corrosion mechanism is needed to provide a solid scientific basis for the risk assessment of the Cu canister in the final disposal of nuclear waste. This should include the local strain formation in the near surface region and in the bulk microstructure of the Cu, as reported previously [19]. Thus, it is crucial to take into account the internal corrosion processes occurring underneath the corrosion product film and the damage of the Cu microstructure caused by the ingress of the corrosive species in the risk assessment of Cu canister [19]. It should be mentioned that the additional radiation effect on the corrosion process caused by highly radioactive spent fuel is not included herein and needs to be considered in future studies.

5. Conclusions

The ToF-SIMS measurements of copper samples after exposures for several months to the simulated O_2-free groundwater with and without sulfide addition provide depth profiles of concentrated corrosive species, 2D images of lateral distribution of the corrosive species at different depth intervals, and 3D images showing deep local penetration along some fast paths. Based on the results, the following conclusions can be drawn:

- During the exposure, in addition to the formation of a corrosion product film on the Cu surface, pronounced penetration of the corrosive species, H, S, O, and Cl, into Cu metal occurs in the near surface region, and deep local penetration proceeds at certain fast paths, most likely along some grain boundaries. This happens even in the absence of sulfide addition.

- The corrosion process of Cu is heterogenous and influenced by the crystallographic orientation of the Cu grains. The corrosion products formed on the surface consist mainly of O- and S-compounds and also of minor Cl-components. The corrosive species, H, S, O, and Cl often segregate together and likely exhibit joint actions, resulting in internal corrosion.

- The corrosion processes, both the formation of the corrosion product film on the surface and penetration of the corrosive species inside the Cu metal, are significantly enhanced by the sulfide addition (Na_2S) at a concentration of 0.001 M, which results in essentially S-rich corrosion products. The initial oxide film formed by pre-oxidation does not act as an effective barrier to the sulfide-induced corrosion.

- The elevated temperature of 60 °C during the exposure greatly accelerates the sulfide-induced corrosion, leading to a several times increase in the thickness of the corrosion product film and the deep penetration of the corrosive species. After four months S reaches 440 nm into the Cu substrate and more than 500 nm along local fast paths.

- The evidence of penetration of the corrosive species, H, S, O, and Cl, especially their deep local penetration into the Cu microstructure, implies the risk for embrittlement and crack initiation in the Cu material. This demonstrates the need for thorough evaluation of sulfide-induced complex forms of Cu corrosion in the risk assessment of Cu canister.

CRediT authorship contribution statement

Xiaoqi Yue: Data curation, Formal analysis, Investigation, Methodology, Writing - original draft. **Per Malmberg:** Data curation, Formal analysis, Methodology, Writing - original draft. **Elisa Isotahdon, Vilma Ratia-Hanby, Elina Huttunen-Saarivirta:** Sample preparation and

immersion tests, Writing - review & editing. **Christofer Leygraf:** Investigation, Visualization, Writing - review & editing. **Jinshan Pan:** Conceptualization, Data curation, Investigation, Methodology, Writing - original draft, Supervision.

Declaration of Competing Interest

The authors declare that they have no known competing financial interests or personal relationships that could have appeared to influence the work reported in this paper.

Data Availability

Data will be made available on request.

Acknowledgement

The financial supports from NKS (Contract AFT/NKS-R(21)127/2) and Swedish Research Council (Vetenskapsrådet, project no. 2021-04157) are greatly acknowledged.

Appendix A. Supporting information

Supplementary data associated with this article can be found in the online version at doi:10.1016/j.corsci.2022.110833.

References

[1] Saanio, T.; Ikonen, A.; Keto, P.; Kirkkomäki, T.; Kukkola, T.; Nieminen, J.; Raiko, H. Design of the Disposal Facility 2012; POSIVA-WR-13–17; Posiva, Finland, 2013.
[2] Saanio, T.; Ikonen, A.; Keto, P.; Kirkkomäki, T.; Kukkola, T.; Nieminen, J.; Raiko, H. Design of the Disposal Facility 2012; POSIVA-WR-13–17; Posiva, Finland, 2013.
[3] E. Huttunen-Saarivirta, P. Rajala, M. Bomberg, L. Carpén, Corrosion of copper in oxygen-deficient groundwater with and without deep bedrock micro-organisms: characterisation of microbial communities and surface processes, Appl. Surf. Sci. 396 (2017) 1044, https://doi.org/10.1016/j.apsusc.2016.11.086.
[4] L. Carpen, P. Rajala, M. Bomberg, Corrosion of copper in anoxic ground water in the presence of SRB, Corros. Sci. Technol. 17 (2018) 147, https://doi.org/10.14773/CST.2018.17.4.147.
[5] E. Huttunen-Saarivirta, E. Ghanbari, F. Mao, P. Rajala, L. Carpén, D.D. Macdonald, Kinetic properties of the passive film on copper in the presence of sulfate-reducing bacteria, J. Electrochem. Soc. 165 (2018) C450, https://doi.org/10.1149/2.007189jes.
[6] D.S. Hall, M. Behazin, W. Jeffrey Binns, P.G. Keech, An evaluation of corrosion processes affecting copper-coated nuclear waste containers in a deep geological repository, Prog. Mater. Sci. 118 (2021), 100766, https://doi.org/10.1016/j.pmatsci.2020.100766.
[7] F. King, M. Kolář, I. Puigdomenech, P. Pitkänen, C. Lilja, Modeling microbial sulfate reduction and the consequences for corrosion of copper canisters, Mater. Corros. 72 (2021) 339, https://doi.org/10.1002/maco.202011770.
[8] F. King, C. Lilja, K. Pedersen, P. Pitkänen, M. Vähänen, An Update of the State-of-the-art Report on the Corrosion of Copper under Expected Conditions in A Deep Geologic Repository, SKB-10-67, Swedish Nuclear Fuel and Waste Management Co., Sweden, 2010.
[9] C. Padovani, F. King, C. Lilja, D. Féron, S. Necib, D. Crusset, V. Deydier, N. Diomidis, R. Gaggiano, T. Ahn, P.G. Keech, D.D. Macdonald, H. Asano, N. Smart, D.S. Hall, H. Hänninen, D. Engelberg, J.J. Noël, D.W. Shoesmith, The corrosion behaviour of candidate container materials for the disposal of high-level waste and spent fuel – a summary of the state of the art and opportunities for synergies in future R&D, Corros. Eng. Sci. Technol. 52 (2017) 227, https://doi.org/10.1080/1478422X.2017.1356973.
[10] R. Becker, J. Öijerholm, Slow Strain Rate Testing of Copper in Sulfide Rich Chloride Containing Deoxygenated Water at 90 °C, SSM 2017:02, Swedish Radiation Authority, Sweden, 2017.
[11] A. Forsström, R. Becker, H. Hänninen, Y. Yagodzinskyy, M. Heikkilä, Sulphide-induced stress corrosion cracking and hydrogen absorption of copper in deoxygenated water at 90°C, Mater. Corros. 72 (2021) 317, https://doi.org/10.1002/maco.202011695.
[12] C.M. Lousada, I.L. Soroka, Y. Yagodzinskyy, N.V. Tarakina, O. Todoshchenko, H. Hänninen, P.A. Korzhavyi, M. Jonsson, Gamma radiation induces hydrogen absorption by copper in water, Sci. Rep. 6 (2016) 24234, https://doi.org/10.1038/srep24234.
[13] I. Soroka, N. Chae, M. Jonsson, On the mechanism of γ-radiation-induced corrosion of copper in water, Corros. Sci. 182 (2021), 109279, https://doi.org/10.1016/j.corsci.2021.109279.
[14] J. Chen, Z. Qin, D.W. Shoesmith, Kinetics of corrosion film growth on copper in neutral chloride solutions containing small concentrations of sulfide, J. Electrochem. Soc. 157 (2010) C338, https://doi.org/10.1149/1.3478570.
[15] J. Chen, Z. Qin, T. Martino, M. Guo, D.W. Shoesmith, Copper transport and sulphide sequestration during copper corrosion in anaerobic aqueous sulphide solutions, Corros. Sci. 131 (2018) 245, https://doi.org/10.1016/j.corsci.2017.11.025.
[16] J.M. Smith, J.C. Wren, M. Odziemkowski, D.W. Shoesmith, The electrochemical response of preoxidized copper in aqueous sulfide solutions, J. Electrochem. Soc. 154 (2007) C431, https://doi.org/10.1149/1.2745647.
[17] H.M. Hollmark, P.G. Keech, J.R. Vegelius, L. Werme, L.-C. Duda, X-Ray absorption spectroscopy of electrochemically oxidized Cu exposed to Na_2S, Corros. Sci. 54 (2012) 85, https://doi.org/10.1016/j.corsci.2011.09.001.
[18] C.M. Lousada, A.J. Johansson, P.A. Korzhavyi, Molecular and dissociative adsorption of water and hydrogen sulfide at perfect and defective Cu(110) surfaces, Phys. Chem. Chem. Phys. 19 (2017) 8111.
[19] F. Zhang, C. Örnek, M. Liu, T. Müller, U. Lienert, V. Ratia-Hanby, L. Carpén, E. Isotahdon, J. Pan, Corrosion-induced microstructure degradation of copper in sulfide-containing simulated anoxic groundwater studied by synchrotron high-energy X-ray diffraction and ab-initio density functional theory calculation, Corros. Sci. 184 (2021), 109390.
[20] J.B. Condon, T. Schober, Hydrogen bubbles in metals, J. Nucl. Mater. 207 (1993) 1–24, https://doi.org/10.1016/0022-3115(93)90244-S.
[21] T.G. Nieh, W.D. Nix, The formation of water vapor bubbles in copper and their effect on intergranular creep fracture, Acta Metall. 28 (1980) 557, https://doi.org/10.1016/0001-6160(80)90122-4.
[22] S. Nakahara, Microscopic mechanism of the hydrogen effect on the ductility of electroless copper, Acta Metall. 36 (1988) 1669, https://doi.org/10.1016/0001-6160(88)90234-9.
[23] Y. Okinaka, H.K. Straschil, The effect of inclusions on the ductility of electroless copper deposits, J. Electrochem. Soc. 133 (1986) 2608, https://doi.org/10.1149/1.2108489.
[24] M.G. Ganchenkova, Y.N. Yagodzinskyy, V.A. Borodin, H. Hänninen, Effects of Hydrogen and Impurities on Void Nucleation in Copper: Simulation Point of View, Philos. Mag. 94 (31) (2014) 3522–3548, https://doi.org/10.1080/14786435.2014.962642.
[25] Y. Yagodzinskyy, E. Malitckii, F. Tuomisto, H. Hänninen, Hydrogen-induced strain localisation in oxygen-free copper in the initial stage of plastic deformation, Philos. Mag. 98 (9) (2018) 727–740, https://doi.org/10.1080/14786435.2017.1417647.
[26] A. Forsström, S. Bossuyt, Y. Yagodzinskyy, K. Tsuzaki, H. Hänninen, Strain localization in copper canister FSW welds for spent nuclear fuel disposal, J. Nucl. Mater. 523 (2019) 347–359, https://doi.org/10.1016/j.jnucmat.2019.06.024.
[27] Y. Yagodzinskyy, E. Malitckii, T. Saukkonen, H. Hänninen, Hydrogen-enhanced creep and cracking of oxygen-free phosphorus-doped copper, Scr. Mater. 67 (12) (2012) 931–934, https://doi.org/10.1016/j.scriptamat.2012.08.018.
[28] Å. Martinsson, R. Sandström, C. Lilja, Hydrogen in Oxygen-Free, Phosphorus-Doped Copper: Charging Techniques, Hydrogen Contents and Modelling of Hydrogen Diffusion and Depth Profile, SKB-TR-13-09, Swedish Nuclear Fuel and Waste Management Co, Sweden, 2013.
[29] Å. Martinsson, R. Sandström, Hydrogen depth profile in phosphorus-doped, oxygen-free copper after cathodic charging, J. Mater. Sci. 47 (2012) 6768, https://doi.org/10.1007/s10853-012-6592-y.
[30] N. Taniguchi, M. Kawasaki, Influence of sulfide concentration on the corrosion behavior of pure copper in synthetic seawater, J. Nucl. Mater. 379 (2008) 154.
[31] Supplementary Information on Canister Integrity Issues, SKB TR-19–15, Swedish Nuclear Fuel and Waste Management Co, 2019.
[32] A. Hedin, J. Johansson, F. King, Comment on "corrosion-induced microstructure degradation of copper in sulfide-containing simulated anoxic groundwater studied by synchrotron high-energy X-ray diffraction and Ab-initio density functional theory calculation, Corros. Sci. 199 (2022), 110182, https://doi.org/10.1016/j.corsci.2022.110182.
[33] J. Pan, C. Örnek, U. Lienert, M. Liu, T. Müller, F. Zhang, V. Ratia-Hanby, L. Carpén, E. Isotahdon, Reply to comment on "corrosion-induced microstructure degradation of copper in sulfide-containing simulated anoxic groundwater studied by synchrotron high-energy X-ray diffraction and Ab-initio density functional theory calculation, Corros. Sci. 199 (2022), 110183, https://doi.org/10.1016/j.corsci.2022.110183.
[34] E. Isotahdon, V. Ratia-Hanby, E. Huttunen-Saarivirta, X. Yue, J. Pan, Corrosion of copper in sulphide containing environment: the role and properties of sulphide films – Annual report 2021, NKS-460, Nordic Nuclear Safety Research NKS, 2022. https://www.nks.org/en/nks_reports/view_document.htm?
[35] D.S. Mcphail, Applications of secondary ion mass spectrometry (SIMS) in materials science, J. Mater. Sci. 41 (2006) 873.
[36] John C. Vickerman, David Briggs (Eds.), ToF-SIMS: Materials Analysis by Mass Spectrometry, 2nd ed., SurfaceSpectra Ltd., 2012.
[37] T. Wirtz, P. Philipp, J.-N. Audinot, D. Dowsett, S. Eswara, High-resolution high-sensitivity elemental imaging by secondary ion mass spectrometry: from traditional 2D and 3D imaging to correlative microscopy, Nanotechnology 26 (2015), 434001.
[38] J. Ekar, P. Panjan, S. Drev, J. Kovač, ToF-SIMS depth profiling of metal, metal oxide, and alloy multilayers in atmospheres of H_2, C_2H_2, CO, and O_2, J. Am. Soc. Mass Spectrom. 33 (2022) 31. ⟨https://surfacespectra.com/books/tof-sims/⟩.
[39] M.J. Graham, R.J. Hussey, Characterization and growth of oxide films, Corros. Sci. 44 (2002) 319, https://doi.org/10.1016/S0010-938X(01)00063-4.

[40] J. Jedlinski, A. Bernasik, K. Kowalski, M. Nocun, On the application of SIMS to study the oxidation mechanisms of alumina formers, Mater. High. Temp. 22 (2005) 505, https://doi.org/10.1179/mht.2005.061.
[41] A. Seyeux, G.S. Frankel, N. Missert, K.A. Unocic, L.H. Klein, A. Galtayries, P. Marcus, ToF-SIMS imaging study of the early stages of corrosion in Al-Cu thin films, J. Electrochem. Soc. 158 (2011) C165.
[42] M. Esmaily, P. Malmberg, M. Shahabi-Navid, J.E. Svensson, L.G. Johansson, ToF-SIMS Investigation of the Corrosion Behavior of Mg Alloy AM50 in Atmospheric Environments, Appl. Surf. Sci. 360 (2016) 98, https://doi.org/10.1016/j.apsusc.2015.11.002.
[43] N. Mortazavi, C. Geers, M. Esmaily, V. Babic, M. Sattari, K. Lindgren, P. Malmberg, B. Jönsson, M. Halvarsson, J.E. Svensson, I. Panas, L.G. Johansson, Interplay of water and reactive elements in oxidation of alumina-forming alloys, Nat. Mater. 17 (2018) 610, https://doi.org/10.1038/s41563-018-0105-6.
[44] K. Möller, Korrosion av koppar i rent syrefritt vatten, R-12-05, Swedish Nuclear Fuel and Waste Management Co, 2012, p. 31. R-12-05.
[45] K. Ollila, Copper Corrosion Experiments under Anoxic Conditions, R-13-34, Swedish Nuclear Fuel and Waste Management Co, 2013, p. 39. R-13-34.
[46] A.B. Belonoshko, A. Rosengren, Ab initio study of water interaction with a Cu surface, Langmuir 26 (2010) 16267.
[47] C.M. Lousada, A.J. Johansson, P.A. Korzhavyi, Thermodynamics of H_2O splitting and H_2 formation at the Cu(110)–water interface, J. Phys. Chem. C. 119 (2015) 14102.
[48] C.M. Lousada, A.J. Johansson, P.A. Korzhavyi, Molecular and dissociative adsorption of water at a defective Cu(110) surface, Surf. Sci. 658 (2017) 1.
[49] C.M. Lousada, A.J. Johansson, P.A. Korzhavyi, Adsorption of hydrogen sulfide, hydrosulfide and sulfide at Cu(110)—polarizability and cooperativity effects. First stages of formation of a sulfide layer, ChemPhysChem 19 (2018) 2159.
[50] A.J. Johansson, C. Lilja, T. Brinck, On the formation of hydrogen gas on copper in anoxic water, J. Chem. Phys. 135 (2011), 084709.
[51] N. Taniguchi, M. Kawasaki, Influence of sulfide concentration on the corrosion behavior of pure copper in synthetic seawater, J. Nucl. Mater. 379 (2008) 154.
[52] M.G. Ganchenkova, Y.N. Yagodzinskyy, V.A. Borodin, H. Hänninen, Effects of hydrogen and impurities on void nucleation in copper: simulation point of view, Philos. Mag. 94 (2014) 3522–3548.
[53] P.A. Korzhavyi, R. Sandström, Monovacancy in copper: trapping efficiency for hydrogen and oxygen impurities, Comput. Mater. Sci. 84 (2014) 122.
[54] C.M. Lousada, P.A. Korzhavyi, Hydrogen sorption capacity of crystal lattice defects and low Miller index surfaces of copper, J. Mater. Sci. 55 (2020) 6623.
[55] A.B. Belonoshko, A. Rosengren, A possible mechanism of copper corrosion in anoxic water, Philos. Mag. 92 (2012) 4618.
[56] C.M. Lousada, P.A. Korzhavyi, Segregation of P and S impurities to a Σ9 grain boundary in Cu, Metals 10 (2020) 1362.
[57] Y. Li, P.A. Korzhavyi, R. Sandström, C. Lilja, Impurity effects on the grain boundary cohesion in copper, Phys. Rev. Mater. 1 (2017), 070602.
[58] H. Magnusson, K. Frisk, Self-diffusion and impurity diffusion of hydrogen, oxygen, sulphur and phosphorus in copper, TR-13-24, Swed. Nucl. Fuel Waste Manag. (2013). ⟨https://www.skb.se/publication/2477839/TR-13-24.pdf⟩.

Corrosion Science 184 (2021) 109390

Contents lists available at ScienceDirect

Corrosion Science

journal homepage: www.elsevier.com/locate/corsci

Corrosion-induced microstructure degradation of copper in sulfide-containing simulated anoxic groundwater studied by synchrotron high-energy X-ray diffraction and *ab-initio* density functional theory calculation

Fan Zhang [a], Cem Örnek [b], Min Liu [a], Timo Müller [c], Ulrich Lienert [c], Vilma Ratia-Hanby [d], Leena Carpén [d], Elisa Isotahdon [d], Jinshan Pan [a,*]

[a] KTH Royal Institute of Technology, Division of Surface and Corrosion Science, Stockholm, Sweden
[b] Istanbul Technical University, Department of Metallurgical and Materials Engineering, Istanbul, Turkey
[c] Deutsches Elektronen-Synchrotron (DESY), Photon Science, Hamburg, Germany
[d] VTT Technical Research Centre of Finland, Espoo, Finland

ARTICLE INFO

Keywords:
Copper canister
Hydrogen infusion
Lattice degradation
Nuclear waste
HEXRD
DFT

ABSTRACT

Synchrotron high-energy XRD measurements and ab-initio DFT calculations were employed to investigate microstructural degradation of copper upon exposure to sulfide-containing anoxic groundwater simulating nuclear waste repository. After two-month exposure, the high-energy XRD measurements revealed heterogeneous lattice deformation in the microstructure and lattice expansion in near-surface regions. The DFT calculations show that sulfur promotes hydrogen adsorption on copper. Water causes surface reconstruction and promotes hydrogen insertion into the microstructure, occurring via interstitial sites next to vacancies leading to lattice dilation and metal bond weakening. Hydrogen infusion in the presence of sulfur caused lattice degradation, indicating a risk for H-induced cracking.

1. Introduction

A large amount of spent fuel is produced every year from commercial nuclear power plants, 1% of the nuclear waste is highly radioactive and its safe disposal is as important as nuclear safety. Deep geological disposal is the prefered approach for permanent storage of the nuclear waste in several countries. Governmental regulations stipulate safe long-term isolation of nuclear waste for a minimum of 100,000 years, which imposes a great engineering challenge. The nuclear waste disposal concept in Sweden and Finland is based on a multi-barrier system, where the spent fuel is first placed in cast-iron inserts, which are then inserted into canisters as a barrier to seal the cast-iron inserts. The canisters will be placed in bedrock in the depth of 400–1000 meters, surrounded by bentonite clay buffer, to achieve the isolation from the human living environment [1–3]. High-purity copper has been chosen for fabricating the canisters that will be placed under granite environments at anaerobic reduction and anoxic aqueous conditions [4]. The compacted bentonite clay acts as a sealing material providing another barrier separating groundwater and the canisters, buffering minor movements of the repository system, and retaining eventual release of nuclides upon canister failure [2,3]. The bedrock is considered stable and durable, providing an outer barrier of the multi-barrier structure between nuclear waste and the biosphere.

For the safety assessment, corrosion of copper under oxic and anoxic conditions, and radiation-influenced and microbiologically-influenced corrosion have been intensively investigated over 40 years [5–11]. A recent review gives an overview of the corrosion issues, debated questions, and ongoing research programs [12]. A number of reports assessing corrosion of copper canister under expected repository conditions with conservative assumptions, often using a uniform corrosion rate in the calculation of corrosion allowance, have concluded that there is no considerable risk for canister failure [12]. However, the risks for several complex forms of copper corrosion have been debated in the Land and Environmental Court of Sweden, leading to the statement to the Swedish Government, that supplementary information related to the long-term behaviour of the copper canisters should be presented and

* Corresponding author.
E-mail address: jinshanp@kth.se (J. Pan).

https://doi.org/10.1016/j.corsci.2021.109390
Received 29 November 2020; Received in revised form 2 March 2021; Accepted 10 March 2021
Available online 15 March 2021

evaluated regarding five issues: i) corrosion due to reaction in oxygen-free water; ii) pitting due to reaction with sulphide; iii) stress corrosion cracking due to reaction with sulphide; iv) hydrogen embrittlement; v) the effect of radioactive radiation on pitting, stress corrosion cracking and hydrogen embrittlement [13]. Clearly, there is a need to gain a deep understanding of the role of sulphur and hydrogen in stress corrosion cracking (SCC) and hydrogen embrittlement of copper in the ground water containing sulphide.

To cover all aspects of safety assessment, it is necessary to evaluate the scenarios when cracks are present in the rock and the bentonite is swelling with groundwater, so copper canisters get into contact with groundwater and even microbes where bentonite sealing could be damaged. Microbial activity on the surface or in the vicinity of the canister was modeled [14], and it was reported to initiate and accelerate general and localized corrosion [15]. Oxygen exists in the initial period of the repository closure and is gradually consumed by oxidation reactions and microorganisms [12]. Oxidation of copper can result in a surface film of Cu_2O or $CuO/Cu(OH)_2$. Once the trapped oxygen is completely consumed, the major threat to the long-term durability of the canister is corrosion by sulfide species (e.g., HS^-) produced in the groundwater by mineral dissolution and/or microbial activity of, e.g., sulfate-reducing bacteria and methanogens in the repository environment [12,16]. Sulfide is known to be a corrosive agent causing SCC of copper in anaerobic chloride containing environments [8,9,17]. Previous studies have shown the role of sulfate-reducing microorganisms [18,19], and biotically-induced formation of Cu_2S layer [20,21], in the corrosion of copper. The sulfide leads to corrosion of copper, forming stable and insoluble sulfides [22–24], e.g.,

$$2Cu + S^{2-} \rightarrow Cu_2S + 2e^- \quad (1)$$

The sulphide-induced corrosion process can be sustained by cathodic reduction of water or HS^-.

$$2H_2O + 2e^- \rightarrow H_2 + 2OH^- \quad (2)$$

$$2HS^- + 2e^- \rightarrow H_2 + 2S^{2-} \quad (3)$$

Studies on copper corrosion often focused on chemical and electrochemical degradation at the copper/electrolyte interface [25,26]. It was also reported that sulfide-induced corrosion might also have a significant influence on the bulk material of copper. Chemical conversion of a film of Cu_2O to Cu_2S on copper has been shown to proceed to completion and extend deep into the bulk Cu [27]. The conversion was observed to extend into the sub-surface region as deep as 100 nm [28]. Moreover, hydrogen may be produced when copper corrodes in the presence of sulfide. In general, hydrogen has detrimental effects on mechanical properties of copper and can create bubbles and microcracks of copper materials [29–32]. Adsorption and diffusion of hydrogen in copper depend on the surface condition and microstructural defects such as dislocations and inclusions, and grain boundaries are primary trapping sites of hydrogen [33,34]. Hydrogen-induced damage of copper canister has, so far, been considered to be negligible due to the belief that the permeation depth of hydrogen would be too small to influence the mechanical integrity of copper canister [35,36]. However, the previously used method only yielded depth-profiles of hydrogen [33,36], but no information about its role in the SCC and hydrogen embrittlement of copper. In the presence of tensile stress/strain, exposure to ground water containing sulfide can cause SCC of copper [8,9,17]. To achieve an atomistic understanding of the mechanism of the SCC and hydrogen embrittlement, it is necessary to study corrosion-induced lattice degradation of copper, particularly the role of sulfur and hydrogen. To our knowledge, this has not been done before.

Here, we report synchrotron high-energy X-ray diffraction (HEXRD) measurements in transmission mode and *ab-initio* density functional theory (DFT) calculations to investigate the effect of exposure to simulated anoxic groundwater containing sulfide on the lattice degradation of copper. The interatomic lattice distances (d-spacing) were measured in 20 μm increments through the entire two-mm thick sample to reveal an in-depth gradient of the lattice deformation and thus the extent of the exposure-induced lattice degradation. DFT calculations of Cu-S-H systems (also in water) were carried out to provide an atomistic understanding of the surface adsorption, dissociation, and infusion of hydrogen that lead to degradation of the Cu lattice.

2. Experimental

2.1. Material used

The tested material was hot rolled, oxygen-free, phosphorus-containing copper (> 99.95 wt.% Cu, 0.005 wt.% P), which is the material used for making canisters, and provided by Finnish nuclear waste management company Posiva Oy. The specimens were cut into approximately 10 mm × 10 mm × 2 mm, and the surface was ground and polished down to 1 μm finishing. Prior to exposure, the specimens were cleaned in acetone and ethanol. The copper material had a typical hot-rolled microstructure, with large grains (several tens to hundreds of micrometers in size) and annealing twins, as seen in Fig. 1. As-polished and pre-oxidized samples were investigated. The pre-oxidation was done at 90 °C in ambient air for seven days after the polishing to simulate the effect of exposure to oxic conditions prior to the anoxic stage. It was previously observed that the pre-oxidation increased mass loss of copper specimens during exposure to anoxic conditions [37].

2.2. Corrosion exposure

The specimens were exposed to simulated groundwater in a sealed bottle for 53 days. The chemical components of the water are given in Table 1, which represent the groundwater of the Finnish disposal site and the effects of added bentonite. Sulfide was added in the form of Na_2S with a concentration of 10^{-3} mol/L (32 mg/L). The exposure was done at room temperature (22 °C) in a laboratory-grade borosilicate glass bottle with a volume of 2 L. The experiment environment was anoxic, achieved by purging the water and the vessel with argon before the start of the test and sealing the vessel with butyl rubber stopper.

2.3. High-energy X-ray diffraction experiment

HEXRD measurements were carried out at the Swedish Materials Science beamline P21.2 at PETRA III of the DESY, Hamburg, Germany. The photon energy was 96 keV (corresponding to 0.1291 Å). The distance between the sample and the Varex 4343CT flat panel detector was about 1.6 m. LaB6 was used for geometrical calibration. The sample surface was aligned to be parallel to the X-ray beam. The sample was

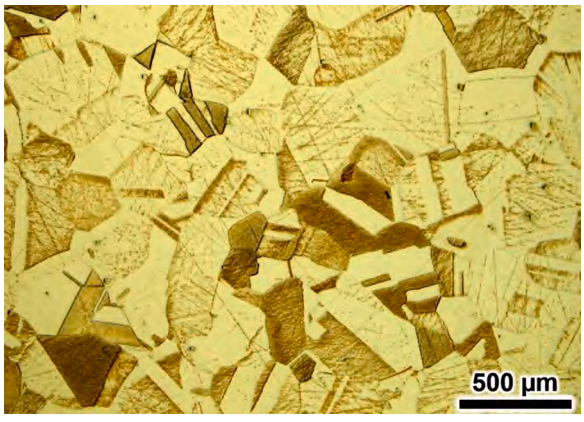

Fig. 1. Optical micrograph of an etched copper sample showing typical microstructure (large grains and annealing twins) of canister material.

Table 1
Chemical components of the used simulated groundwater.

	K	Ca	Cl	Na	SO_4	Br	HCO_3	Mg	Sr	Si	B	F	Mn	PO_4	S	lactate
mg/L	54.7	280.0	5274.0	3226.1	595.0	42.3	13.7	100.0	8.8	3.1	1.1	0.8	0.2	0.1	32.0	1.0

positioned 45° towards the beam with respect to its vertical rotational axis and illuminated 1.5 mm away from the edge to reduce the effective sample depth for transmission to about 3 mm. The beam size was 20 μm (vertical) x 55 μm (horizontal). The sample surface was defined as the position where the intensity of the transmitted beam through the specimen had its half intensity when sampling across the sample surface. The sample was moved vertically in steps of 20 μm (z-axis). At each z-position (height), a 2-D diffraction pattern was recorded with a sampling time of 1 s. During each data sampling, the sample was moved by 1 mm along the horizontal axis (parallel to the surface) to improve grain statistics, resulting overall in a serpentine sample movement (transmission was kept less than 3 mm). The measurement at the surface yields diffraction signals from approximately 10 μm beneath the surface and all other measurement points include signals from a volume of 20 μm height. The measurement time for each scanned layer was 3.8–4.0 s, including the summation of sampling time and dead time for stage movement. The sample was scanned from 150 μm above the upper-side surface down to 150 μm below the lower-side surface to capture the entire specimen. The measurement setup is schematically illustrated in Fig. 2. The diffraction patterns were collected and stored as tiff files, which were then integrated azimuthally in a range of ±5° using pyFAI [38]. The diffraction data were also integrated over the entire azimuth full-circle (0–360°). The intensities were normalized using the primary beam intensity, which was collected simultaneously to compensate beam fluctuation. All images were background subtracted. Data analysis was performed using the Peak Analyzer module Fit Peaks (Pro) of OriginPro 2020b V9.7.5.184 software, utilizing a mixture algorithm of Lorentzian and Gaussian peaks for fitting, which gave the best fitting quality. The *d*-spacing was determined from the position of the 111 Bragg peak. The full-ring integration provided average but statistically relevant information about the changes in the lattice size. The d-spacings of the non-exposed specimen was taken as the reference point, and all the relative changes of the lattice parameter were calculated with respect to the non-exposed condition.

3. DFT calculation

DFT calculation was performed to study the surface adsorption and dissociation of S-components (H_2S and HS) on Cu(110) surface and the infusion of H into the Cu lattice, to achieve an atomistic understanding of the effect of S and H on the lattice degradation. Cu(110) surface was chosen in the calculation for easy comparison with literature reports, and the results differ only slightly for other surface orientations. Two types of interactions of H_2S with Cu were considered, i.e., the adsorption at the Cu(110) surface, and the insertion into defects in the Cu subsurface region. The Cu surface was modelled by a six-layer slab orientated at 110, which contains 36 Cu atoms, which is commonly used in DFT calculations of Cu. A vacuum layer equal to about two times the height of the slab was added to the calculation model. The Dmol3 code was used to theoretically investigate the interaction between environments and Cu [39,40], where the generalized gradient approximation (GGA) with PW91 exchange-correlation function [41] was applied, and a k-point of 3 × 6 × 1 was selected in the calculation. All the core electrons in the system were treated with DFT semi-core pseudopotentials. Optimization was regarded to be complete when the energy, residual force and displacement of each atom of the system converged to 10^{-5} Hartree (Ha), 0.002 Ha/Å, and 0.005 Å, respectively.

4. Results and discussion

4.1. Deformation of Cu lattice

From the HEXRD data, d-spacing of the Cu lattice was determined. Fig. 3 displays polar *d*-spacing plots of a non-exposed sample (reference), a pre-oxidized sample (oxidized), and a pre-oxidized sample after the exposure to the simulated groundwater (exposed or sulfur-exposed). The polar plots show the calculated d-spacing as a function of the azimuthal angle and depth from the surface of the sample. The vertical axis on the left of each polar plot (depth information) indicates the position inside the sample, with units in microns. The depth axis is radial, with 0 μm showing the sample surface. The increasing number of depths indicates the measured d-spacing below the surface. The polar plot shows the measured d-spacing for down to 1000 μm in bulk. The azimuth angle is plotted in the hoop-direction. The color code represents the magnitude of d-spacing, with the lattice size increasing from cold to hot colors. The outer ring of the polar plot shows the d-spacings for the surface along with all azimuth angles.

The non-exposed reference sample (Fig. 3a) shows quite uniform *d*-

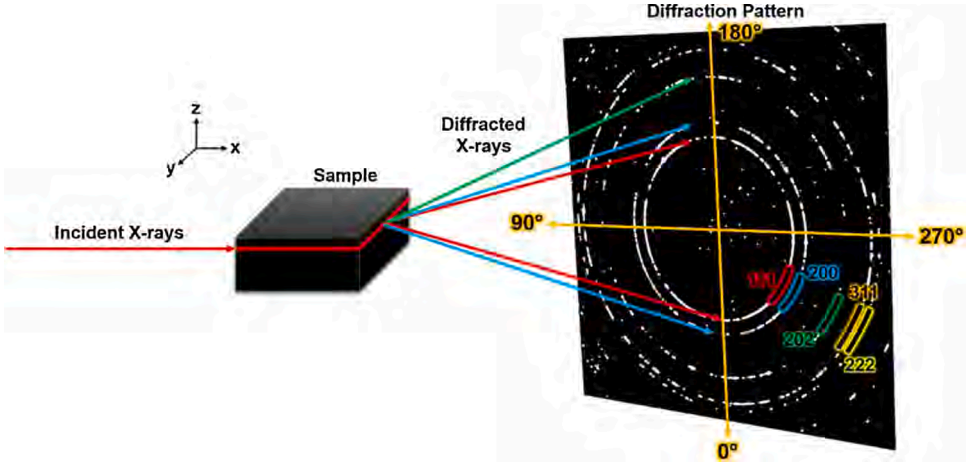

Fig. 2. Schematic illustration of the experimental setup for the HEXRD measurements showing X-rays radiating the copper specimen and the diffracted X-rays with the 2D diffraction pattern collected by a flat-panel detector. The azimuth angles are indicated.

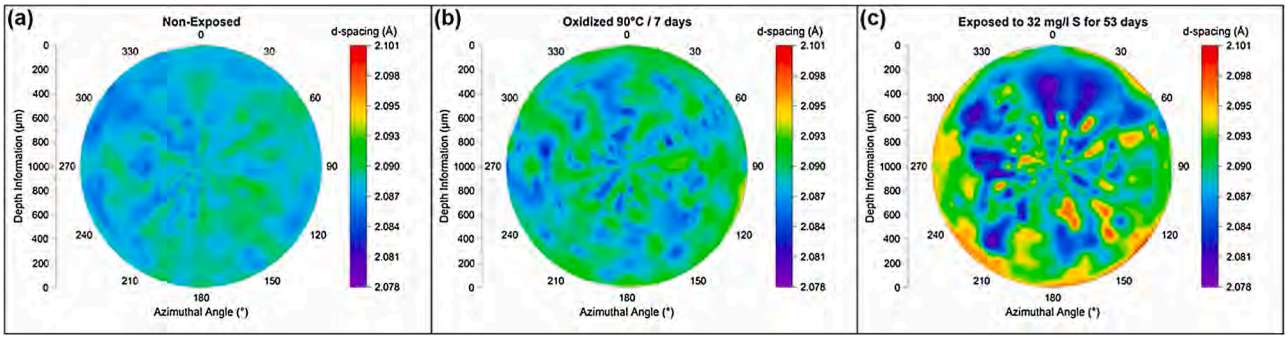

Fig. 3. Polar plots showing the calculated d-spacing of the Bragg peak with (111) orientation as a function of depth from the surface and azimuthal angle for the copper specimens of (a) the non-exposed condition, (b) pre-oxidized at 90 °C for seven days, and (c) pre-oxidized and exposed to 32 mg/l of sulfide-containing groundwater.

spacing values expected for the Cu lattice, with small deviations across the measured depth reflecting the heterogeneities in the microstructure, such as grain boundaries and grains in different sizes as shown in Fig. 1. In contrast, the magnitude and scatter of the *d*-spacings increased for the pre-oxidized sample (Fig. 3b). The sulfur-exposed sample had the largest *d*-spacings, indicating most degradation (Fig. 3c). While the pre-oxidation affected the near-surface region down to a depth of 20−40 µm (see also Fig. 5), the sulfur-exposure resulted in large lattice expansion down to 400 µm, with some expansion occurred on individual sites in the microstructure between 400 µm and 900 µm in depth. It seems that compensating lattice contraction occurred in the sub-surface microstructure as compared to the non-exposed and pre-oxidized specimens (Fig. 3c). Hence, the exposure to the simulated groundwater caused both heterogeneous lattice expansion and contraction. The size of the large grains of the microstructure was 200−500 µm and thus much larger than the X-ray beam size (20 µm × 55 µm), which explains the discrete heterogeneities in the d-spacings. Each scan line contained signals form approximately 50–100 grains, which is well-representative for the entire microstructure. Compensating lattice contraction, to a small extent, was also observed for the pre-oxidized specimen (Fig. 3b).

The lattice expansion, measured in the exposed specimen, showed a preferential azimuthal orientation. The lattice expansion was more pronounced along with the azimuthal angles 120−240°, which means that the lattice expanded orthogonal to the exposed surface. The increase of the interatomic distance of the lattice implies grain elongation due to directional strain formation, which is likely induced by the infusion of H, and possibly also S and/or O atoms, from the environment into the lattice of the Cu (discussed in the sections below).

Furthermore, the change of the *d*-spacing was used to calculate the relative change of the lattice parameter at different depths, which includes strain development due to H insertion into the lattice. As shown in Fig. 4, the pre-oxidation caused lattice expansion of the surface region, evidenced by positive values of the relative lattice change at most azimuthal angles (Fig. 4a). In contrast, the sulfur-exposure resulted in both lattice expansion and contraction in the surface region (Fig. 4a) and

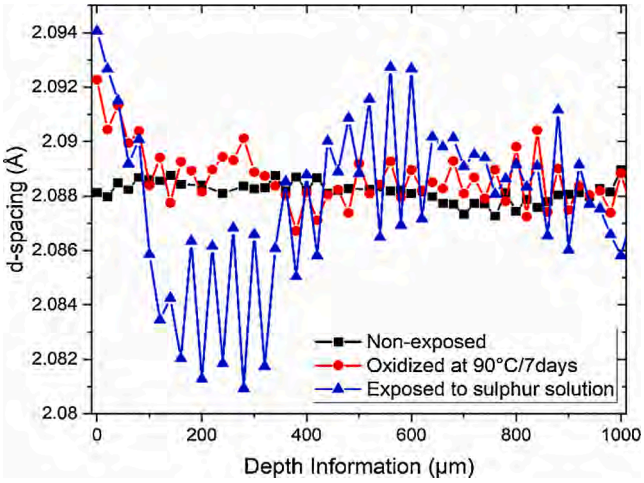

Fig. 5. The measured d-spacings (integrated over the entire (111)-oriented 2D-diffraction ring) plotted against the depth from the surface of the copper specimens.

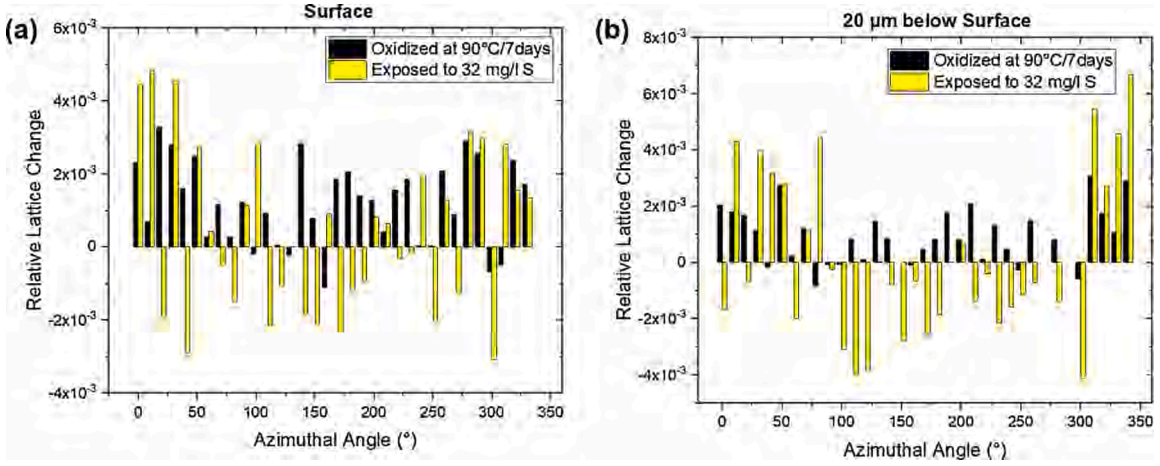

Fig. 4. The calculated relative change of lattice parameter in (a) the near-surface region, and (b) 20 µm below the surface, for the pre-oxidized and the sulfur-exposed sample, respectively.

the sub-surface region at 20 μm (Fig. 4b), varying with azimuthal angle. The non-uniform lattice deformation is due to the large scatter in grain size in the microstructure, as explained above. A histogram figure summarizes the measured d-spacings for all tested specimens can be found in the supplementary material (Fig. S1), which shows the lattice degradation as surface and near-surface lattice expansion and the formation of compensating lattice contraction in the sub-surface, which was more severe for the sulfur-exposed Cu sample than the pre-oxidized one.

4.2. Lattice deformation of the near-surface region

Fig. 5 shows the measured *d*-spacings plotted against the depth, i.e., in-depth gradient, for the samples. The *d*-spacings were calculated from full-ring-integrated data, indicating the lattice expansion in the near-surface region caused by the pre-oxidation and the sulfur-exposure, which is evident by comparison with the non-exposed sample showing nearly constant *d*-spacing across the depth. The pre-oxidation led to lattice expansion of the near-surface region down to ~90 μm. The exposure to the sulfide-containing groundwater resulted in an altered surface layer of ~400 μm. The magnitude of lattice expansion was more pronounced for the sulfur-exposed sample, clearly demonstrating a lattice degradation effect induced by the sulfide-containing groundwater. In addition to lattice expansion of the near-surface region down to ~90 μm, the sulfur-exposure also led to lattice contraction (depth of 100−400 μm in Fig. 5) beneath the lattice expansion near-surface region. However, the pre-oxidized sample did not show a similar compensation effect; therefore, the mechanism for the sub-surface lattice contraction must be of a different nature. The pronounced lattice contraction in the sulfur-exposed sample might have been generated due to compensation of lattice expansion of the near-surface region.

It is well-known that the pre-oxidation causes the formation of copper oxides, typically CuO/Cu_2O, on the Cu surface. The oxides have higher lattice constants and thus lead to a widening of the Cu lattice underneath the oxides. However, the thickness of the oxide film was reported to be only a few hundreds of nm [42,43]. Our HEXRD results, shown in Fig. 5, suggest that the pre-oxidation causes significant lattice deformation in the near-surface region down to 90 μm in depth. The surface grains became distorted, which led to the evolution of macro-strains. Note that the sulfur-exposed sample was also pre-oxidized; therefore, the measured data represent the effects of the pre-oxidation and sulfidation occurred during the exposure to the simulated groundwater. Therefore, the difference between these two samples shows the effect of interactions of the pre-oxidized sample with the sulfide-containing groundwater. The data of the sulfur-exposed sample show that the relative change of the lattice parameter in the surface region reaches a magnitude of 10^{-3}, indicating a high level of lattice deformation developed in the surface region, which can be explained by considering the H-induced lattice dilation.

The fitting results of the full-ring diffraction data in Fig. 6 revealed that the full-width at half maximum (FWHM) values of all Bragg peaks increased by the pre-oxidation and exposure to the S-containing water, with the latter having the most severe effect. Increase of FWHM typically indicates the formation of micro-deformation, i.e., the deformation within grains, and/or the reduction of the grain size. The deformation of the surface layer due to the formation of corrosion products result in heterogeneous grain deformation, which is reduced with increasing depth in bulk. However, the exposure to the S-containing water resulted in larger surface deformation (lattice expansion) and also sub-surface deformation (lattice contraction). The oxidation on the surface was rather homogeneous and caused a widening of the lattice, but the degradation caused by the exposure to the S-containing water exhibited a more heterogeneous nature. During the exposure to the simulated groundwater, Cu sulfides can form as a result of the corrosion of Cu. Moreover, pre-formed Cu_2O film can also be converted to the Cu_2S film, which was reported to extend into the bulk of Cu for about 100 nm from

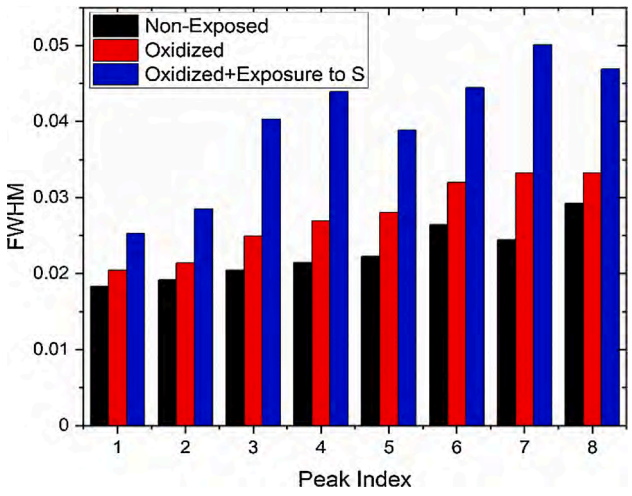

Fig. 6. Full-width at half maximum (FWHM) values from all measured diffraction peaks for the analyzed copper specimens, averaged over the entire sample thickness.

the surface [28]. However, the formation of corrosion products alone cannot explain the large lattice deformation, in particular, not the sub-surface lattice contraction observed in the sulfur-exposed sample. There are, apparently, other effects that resulted in the sub-surface lattice degradation. H and S can absorb and enter into Cu lattice, and their ingress is most favored at grain boundaries. Most likely, the H and S ingress caused the lattice degradation observed in the sulfur-exposed sample.

4.3. Adsorption of H_2S, HS, S, H on Cu(110) surface

In the assessment of corrosion risk of the Cu canister during long-term geological disposal, a key question is the corrosion of material integrity caused by S and H because of their presence in the groundwater in bedrock. DFT calculation of adsorption energies of H_2S, HS, S, H on Cu (110) surface was performed. Fig. 7 shows the calculated adsorption energies (binding strength) and corresponding models for the adsorbate species on Cu(110) surface. As seen in Fig. 7a, individual S atom adsorbs on the Cu(110) surface with adsorption energy (E_{ad}) of −1.5 eV, indicating a strong interaction between S and Cu surface. Compared to one S atom, H_2S molecule shows a low affinity towards Cu surface, the adsorption energy of which agrees well with the calculated value reported in the literature [44,45], while the adsorption energy of HS group is −0.7 eV, slightly lower than that of H_2S [45]. For a single H atom on Cu, a weak binding strength is found, with an adsorption energy of −0.2 eV, agreeing well with the literature [44]. By contrast, H_2S in its full dissociation form, i.e., H_S_H, significantly enhances the adsorption strength, and so is the dissociated HS (H_S), indicating a synergistic effect of H and S on the adsorption onto the Cu surface. Moreover, dissociation of H_2S into H_S_H and HS into H_S most likely proceeds spontaneously on the Cu surface, indicated by the large energy differences.

4.4. Insertion of H into Cu(110) lattice

Vacancies and interstitial atoms are two types of point defects in metals, which render the infusion of atoms from the environment into metal lattice. Interstitial H in metal is utilized for hydrogen storage, in which H dissolves in the metal lattice as solute and thus form hydride [46]. In general, atomic infusion can induce a large strain within metals, which may eventually lead to material rupture [47,48]. Here, we performed DFT calculation to investigate H insertion into Cu(110) lattice via the two types of defects, i.e., Cu vacancy or interstitial site,

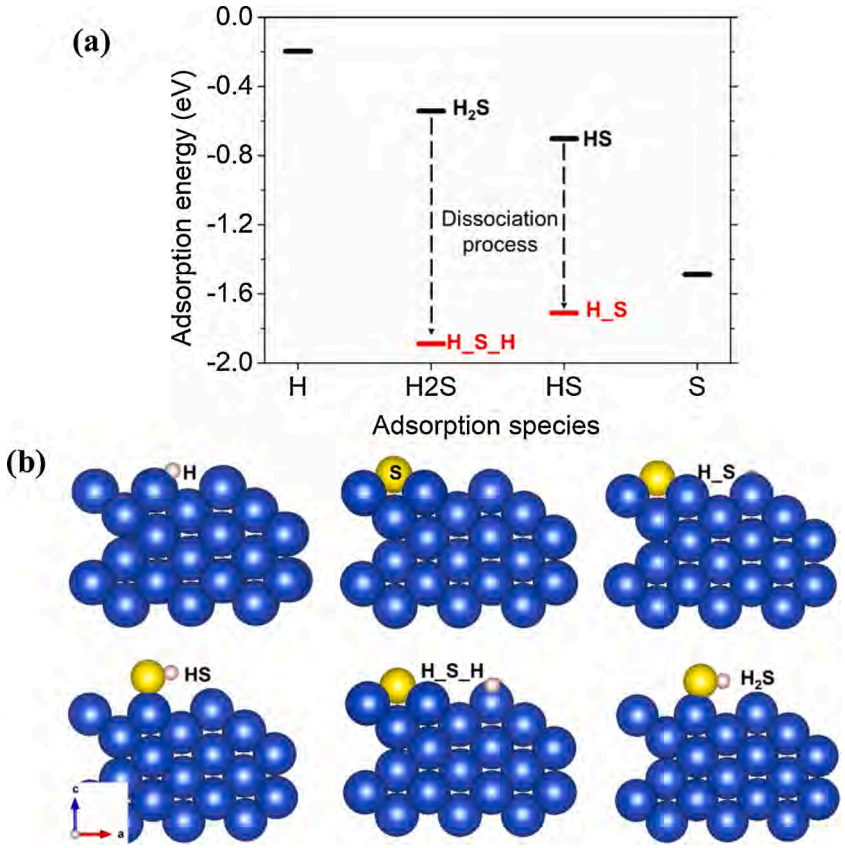

Fig. 7. (a) Calculated adsorption energies (E_{ad}) of H_2S and HS in their molecular form (H_2S, or HS), and full dissociation form (H_S_H, or H_S), and of individual S and individual H. (b) The adsorption configurations of molecular/dissociated H_2S/HS after optimization are depicted in side view, with yellow, light pink, and blue balls representing S, H, and Cu atoms.

respectively. First, individual H atom was introduced into Cu(110) via a Cu vacancy located at different depths, i.e., 1st, 2nd and 3rd atomic layer, denoted as the case "vac" in the modeling. Structure models with one H atom located at an interstitial site at 1st, 2nd and 3rd atomic layers are showing in Fig. 8a. While H stayed at nearly the same location in the first and third layer, the calculated insertion energies indicate that such insertion via vacancy is energetically unfavorable, as shown in Fig. 8b. In the case when H is inserted into a vacancy at the second atomic layer, after optimization the H atom moved up and stayed above the surface, suggesting a transition from "insertion" mode to "adsorption" mode, which resulted in a more stable configuration (binding energy of H on Cu surface is −0.36 eV) compared to the other two cases. This indicates that Cu vacancy promotes H adsorption, as compared to H adsorption on perfect Cu(110) surface (binding energy is −0.2 eV, see Fig. 8b). Furthermore, by introducing one vacancy next to the H atom, the insertion energy is slightly reduced and even to a native value (favorable) when the vacancy is at the same atomic layer as the H atom (Fig. 8b). The models as well as insertion energy corresponding to an

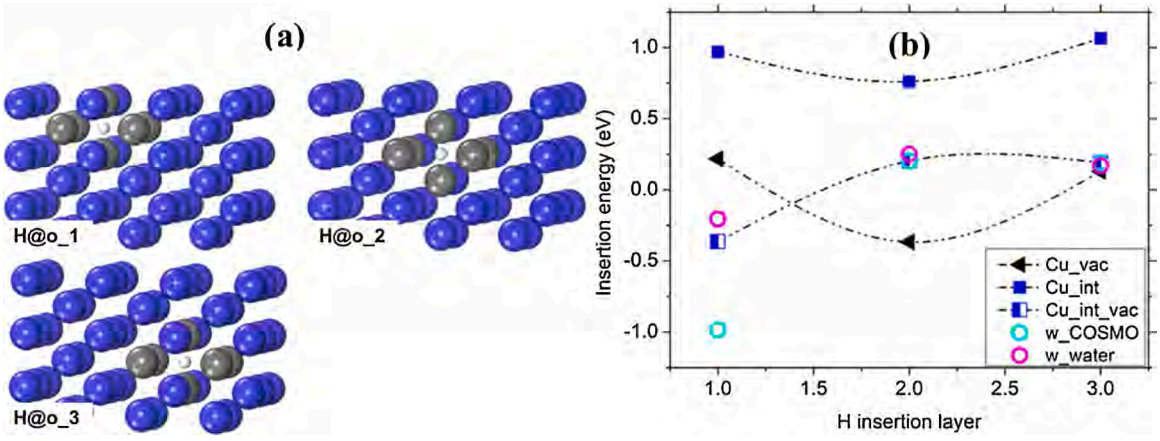

Fig. 8. (a) Models of Cu(110) surface with one H at 1st, 2nd and 3rd atomic layers denoted as H@o_1, H@o_2, H@o_3, respectively. The six Cu atoms comprising the octahedron around H atom (in light pink) are highlighted in grey, whereas other Cu atoms are in blue. (b) Insertion energy of H at a vacancy (case "vac"), an interstitial site (case "int"), and at an interstitial site accompanied by a vacancy (case "vac_int") in Cu(110) at 1st, 2nd and 3rd atomic layers. The effect of both implicit and explicit solvation is considered within the scheme of the "vac_int" case.

extra vacancy at different atomic layers can be found in the supplementary material (Fig. S2).

On the other hand, it is more likely that small atoms insert into metal lattice by occupying interstitial sites. For face-centered cubic metals like copper, its octahedral interstitial sites are usually more accessible for accommodation of small solute atoms. Here we only consider the octahedral interstitial site, the most favorable occupation site of H atom, as an example to show the energetical as well as structural characters of H insertion. The local structure comprised by the H atom and six surrounding Cu atoms are shown in Fig. 9a, and calculated lattice relaxation (expansion or contraction) along different directions are shown in Fig. 9b–d. For the interstitial H atom alone (case "int") without vacancy, the calculated insertion energy is higher (less favorable) compared to the vacancy case discussed above, see Fig. 8b. This could be attributed to large local relaxations within Cu lattice caused by H insertion. Further modeling was done by introducing an extra vacancy besides the H atom (case "vac_int"). Three situations with different relative locations between the H atom and the vacancy were considered, i.e., the vacancy is located at the upper layer, lower layer, or the same layer as the H atom. The results show that only when the vacancy is at the same layer as the H atom, it could significantly stabilize the H insertion (negative insertion energy, Fig. 8b). This can be understood by considering the almost vanished relaxations (especially in the z-direction) when a neighboring Cu vacancy is present, shown as "With vacancy" in Fig. 9b–d. A complete depiction of insertion energy data for different vacancy positions at different atomic layers can be found in the supplementary material (Fig. S3).

In the ideal case, the smallest and biggest distance between two Cu atoms within the local octahedron (Fig. 9a) are 2.578 Å and 3.646 Å, respectively. With one H atom staying at the center of this octahedron after optimization, positive relaxation in the z-direction (i.e., normal to Cu surface) is 17~22 % of the original atomic distance (Cu_0-Cu_5), significantly larger than that in x- or y-direction (Fig. 9b–d). Such large positive relaxations imply that the whole structure in z-direction must bear a large lattice dilation. On the other hand, H-induced relaxation in x-direction decreases as the H atom moves into inner layers, probably due to that the surface allows larger deformation. In contrast, relaxations in the y-direction are negligibly small (Fig. 9b–d). These calculations suggest that H insertion in octahedral interstitial sites generates strains in an anisotropic way, providing certain evidence for our experimental observations. Moreover, the enlarged Cu—Cu bond length and the lattice relaxation in x, y, and z1/z2 directions induced by H insertion, shown in Fig. 9, indicate a decrease of the metal bond strength, although the local relaxation/bond decrease may not be reflected in the averaged Cu bond strength.

Additionally, both implicit and explicit water environments were included in the modeling to investigate their influence on H insertion into Cu lattice. In the implicit water model, water molecules are treated as a continuum medium (COSMO) model [49,50], whereas in the explicit water model, two monolayers of water molecules (equal to twelve water molecules on the Cu slab) were considered in the calculation. For thick water layers, explicit water models become too difficult for the calculation, while the implicit water model is a good approximation of aqueous environments since water molecules are treated as a continuous aqueous layer. It turns out that the water solvation barely influences the insertion energy, except in the case when H lies at the first octahedral interstitial site under implicit water environment, where the insertion energy decreases largely to a negative value around −1 eV (Fig. 8b). In this case, the water environment causes a considerable reconstruction of the Cu surface, with a surface Cu atom occupying the subsurface Cu vacancy, as illustrated in Fig. 10, which is not observed in the non-solvation case. Such reconstruction could be responsible for the large decrease of the insertion energy. When the H atom moves deeper into the Cu lattice, the effect of solvation on the insertion energy quickly weakens (Fig. 8b).

4.5. Diffusion of H in Cu

The diffusion of H, S, and O in Cu, and self-diffusion of Cu have been reviewed concerning the safety assessment of the copper canister [51]. The transport mechanism and kinetics of these elements depend on the service condition, such as temperature and time [52]. Cu and S are substitutional elements and their diffusion takes place through the movement of point defects in the crystalline lattice. Lattice diffusion via

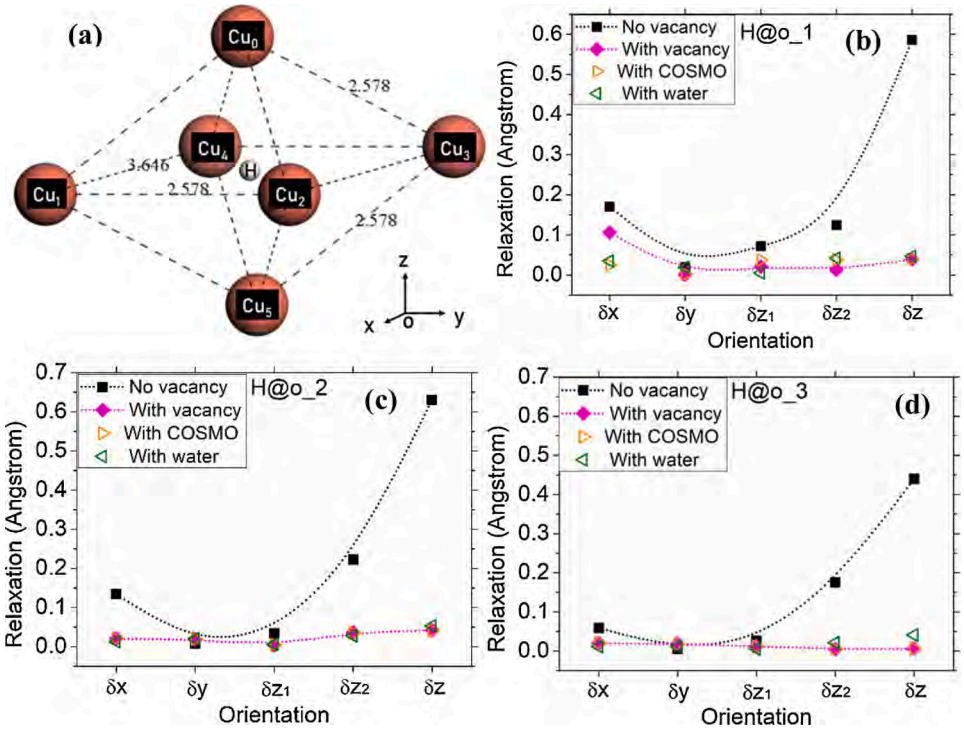

Fig. 9. (a) Configuration (before optimization) with one H atom located at the center of the octahedron comprised by six Cu atoms, which gives initial atomic distances between two Cu atoms: $Cu_{1\text{-}4} = Cu_{2\text{-}3} = 3.646$ Å (x direction), $Cu_{1\text{-}2} = Cu_{3\text{-}4} = 2.578$ Å (y direction), while Cu_0 and Cu_5 are both 2.578 Å away from the other four Cu atoms (denoted as z_2, z_1 direction, respectively); $Cu_{0\text{-}5} = 2.578$ Å is denoted as z direction. (b)~(d) Comparison between the relaxations induced by H insertion within o_1, o_2, o_3 under differed situations.

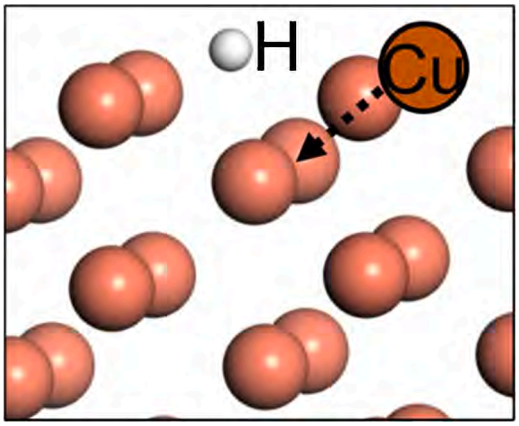

Fig. 10. A snapshot shows a surface Cu atom moves to and finally occupies a subsurface Cu vacancy when H atom is located at the first octahedral interstitial site.

vacancy is the dominating mechanism for diffusion of such large substitutional elements in metals at high temperatures. At temperatures below 100 °C, however, diffusion of Cu and S occurs almost entirely along grain boundaries, and the diffusivity of S is higher than the self-diffusion of Cu. S has very low solubility in Cu due to the formation of sulfides, which is a pinning effect. Estimated by using the diffusion data at room temperature, it takes 100,000 years for S and more than a million years for Cu to diffuse 5 cm distance (the thickness of the canister) along the grain boundaries in Cu [51].

O and H are the interstitial elements that can permeate the whole material via the interstitial sites. The interstitial diffusion occurs typically much faster than substitutional diffusion. However, similar to S, the solubility of O in Cu is very low at ambient temperature due to the formation of oxides. There are experimental data of self-diffusion of Cu at grain boundaries down to 250 °C [53], whereas no experimental data of S and O diffusion in Cu below 500 °C can be found because that is not detectable [51]. Thus, diffusion of S, O, and Cu is negligible at ambient temperature [51,52]. In contrast, H produced from the sulfide-induced corrosion of Cu can diffuse into the Cu [54], along the grain boundaries and also through the grains of Cu lattice. H has high mobility and permeability down to room temperature [55], and hydrogen depth profiles in hydrogen-charged copper specimens could be measured [35,36]. H diffusion in Cu lattice is much faster than S and O. By using the diffusion data in [51], it is estimated that H diffusion in Cu can reach 5 cm diffusion distance within 1000 years at room temperature. Based on the literature reports about H, S and O diffusion in Cu reviewed recently [56], only H diffusion in Cu lattice is considerable in our system.

4.6. H-induced lattice deformation and its implications

During long-term storage in the repository of the Cu canister, H may be produced on the Cu surface in contact with the groundwater by multiple processes. Microbiological activity in the vicinity, near-field and far-field [12,14,16,57], or on the surface of the canister if the bentonite barrier is damaged [15,19–21], produce sulfide species (mainly HS^- ions), and dissociation of the sulfide species on the Cu surface releases atomic S and H, which is a spontaneous process according to the DFT calculation [45, and this work]. Moreover, sulfide-induced corrosion reaction of Cu can generate H on the surface [24,25]. Furthermore, atomic H can also be produced at water/Cu interface through radiolysis of water, and it has been reported that gamma radiation from spent nuclear fuel greatly increases the H infusion into Cu, up to several orders of magnitudes depending on the dose of the radiation [10,11]. The DFT calculations suggest that H adsorption on Cu is energetically favorable, and co-existence with S promotes the H adsorption. H diffusion into Cu via interstitial sites is enhanced in the presence of vacancies in the Cu lattice. Moreover, water environment leads to a reconstruction of Cu surface, which facilitates the H insertion into Cu lattice. Thus, there is a risk for H-induced damage of the copper material associated with H infusion.

H absorption and diffusion in Cu are affected by the microstructure, and H can be trapped in defects such as grain boundaries and dislocations. H atoms entering the Cu material may lead to formation of voids and bubbles [30,34], and also enhance the creep rate and formation of microcracks showing an intergranular dimpled fracture [58,59]. At atomic level, H insertion into Cu lattice via interstitial sites leads to local lattice dilation, which also indicates a weakening of the Cu—Cu bond strength, implying a tendency for embrittlement. In the Cu material, the grains have different sizes and orientations, and the H-induced lattice deformation may vary and distribute heterogeneously in the microstructure. The lattice dilation due to H insertion is not directly related to macroscopic stress; however, if there is a depth gradient, then stresses may arise, which changes the lattice spacing. So changes of lattice spacings have two superimposed reasons: lattice dilation from H insertion and stresses caused by heterogeneous hydrogen distribution. Therefore, as a result of these two effects, H infusion can lead to the formation of a macroscopic lattice expansion, especially when accumulated in the surface region leading to a depth gradient.

The HEXRD measurements in this work show that deformation of Cu lattice induced by the 2-month exposure to the simulated groundwater occurred from the surface and extended deep into the bulk. The most lattice widening and lattice expansion occurred in the near-surface region down to 90 μm into the bulk. Based on the solubility and diffusion data, only H infusion could explain the measured Cu lattice deformation of this length scale, and the DFT calculation provides support for H-induced expansion of the Cu lattice. In this case, the hydrogen originated only from the corrosion reactions occurring during the exposure. The water environment facilitated the surface degradation, and S diffusion via grain boundaries may have contributed to the lattice deformation in the near-surface region. The measurement results provide clear evidence for highly heterogeneous lattice deformation, which is due to the microstructural heterogeneities in the Cu material. The tensile strain/stress curves were measured for the Cu material in sulfide-containing synthetic seawater, which show initial yielding starting at about 70 MPa and the maximum stress after about 40 % deformation is about 170 MPa [17]. Taking Young's modulus as 120 GPa, the respective elastic strains are 6×10^{-4} and 1.4×10^{-3}. These numbers should be considered as macroscopic averages over many grains. It was concluded that the Cu material is susceptible to intergranular attack (selective grain boundary dissolution) at low sulfide concentration (<0.005 M) and SCC at higher sulfide concentration (0.01 M). Recent experimental studies have confirmed the susceptibility of the Cu material to intergranular attack and SCC at high sulfide concentration [8,9]. In our work, without hydrogen charging and without applied strain, the two months exposure in the sulfide-containing groundwater already led to highly heterogeneous lattice deformation in the microstructure, and the measured lattice expansion in the surface region (within a depth of 90 μm) reached a magnitude of 10^{-3}, which shows the risk for a transition from elastic to plastic deformation and thus initiation of cracks at individual local sites.

Hydrogen-induced strain localization was observed in the Cu material in the initial stage of plastic deformation [60], and friction stir welding to seal the canister was found to increase hydrogen uptake in the weld zone and lead to strain localization near the weld zone [61]. Most likely, hydrogen infusion and associated local strain development play an important role in the reported susceptibility of Cu to SCC in the ground water containing sulfide [8,9,17]. During long-term storage in the repository of the Cu canister in the ground water containing sulfides, the sulfide-induced corrosion and hydrogen infusion may occur and lead to local strain development to a significant level and extend to a considerable depth. At grain boundaries in the surface region (interface between Cu and corrosion product), the H infusion and associated local tensile strain may lead to the initiation of microcracks, as reported in the

literature [30,34,58,59]. In a review report focusing on SCC of copper canisters, a conclusion of low risk for SCC was made based on considerations of classical SCC mechanisms caused by SCC agents (ammonia, acetate, nitrite, etc.), but the role of hydrogen in the sulfide-induced corrosion was ignored [62]. In the safety assessment reports, the corrosion allowance calculation mainly considers the rates of uniform corrosion in different forms [5,12,13]. For the sulfide-induced corrosion, the consequence was calculated as uniform corrosion thickness based on the amount of sulfur-species that reacts with copper and forms copper sulfide (Cu_2S) on the surface [54], without considering the effect of hydrogen that can enter the copper material. However, our HEXRD measurements clearly demonstrate the risk for H-induced SCC of the Cu material exposed to sulfide-containing groundwater. The DFT calculations provide a fundamental understanding of the role of S and H in the lattice degradation (embrittlement), which can result in highly heterogeneous microstructure degradation in the near-surface region leading to SCC of the canister. Considering the new findings from this work and recent studies of S- and H-induced corrosion and SCC [8,9,19–21,45,60,61], in the safety assessment of Cu canister, the risk for such complex forms of corrosion, i.e., SCC and hydrogen embrittlement, must be considered based on the state-of-the-art of the knowledge. Since the level of sulfide is a crucial issue, further studies are needed to improve our understanding at the atomic level in order to fully assess the risk for SCC and hydrogen embrittlement of Cu canister induced by sulfide-species in the groundwater, and by the radiation of spent fuel, alone and combined. It is necessary to consider not only the general corrosion as measured by the formation of corrosion products on the surface, but also the consequence of SCC and hydrogen embrittlement induced by H infusion into the Cu lattice and the influence of the microstructure.

5. Conclusion

Synchrotron HEXRD measurement and *ab initio* DFT calculation were combined to investigate the effects of pre-oxidation and exposure to simulated anoxic groundwater containing sulfide on the degradation of the lattice of the Cu material. The HEXRD measurement yielded 3-dimensional *d*-spacing data of the Cu samples, showing heterogeneous lattice deformation. The DFT calculation provided energetics of adsorption of H and S on Cu surface, as well as lattice relaxation induced by H insertion via interstitial sites in Cu lattice. The following conclusions can be drawn:

- The pre-oxidation of the Cu sample caused a lattice expansion mainly in the near-surface region ca. 90 μm deep.
- The exposure to the sulfide-containing simulated anoxic groundwater for two months caused a significant lattice deformation extending several hundreds of μm into the bulk, with an in-depth gradient of lattice expansion in the near-surface region ca. 90 μm deep and lattice contraction beneath the expansion region.
- Dissociation of H_2S and HS are exothermic processes, indicating spontaneous adsorption of H, H_S and H_S_H on Cu surface. The presence of S promotes the adsorption of H on the Cu surface.
- Water environment causes a considerable surface reconstruction of Cu lattice, leading to a large decrease in the insertion energy of H in the surface layer facilitating H ingress.
- H insertion via interstitial sites in Cu lattice occurs preferably in the presence of vacancies, and causes lattice expansion, mainly in the vertical direction to the surface. H insertion leads to a weakening of Cu-Cu bond strength.
- Only H infusion can explain the measured lattice dilation in the surface region after the exposure to the S-containing simulated anoxic groundwater, which indicates a risk for H-induced initiation of microcracks.
- As an overall implication the results clearly demonstrate the risk for H-induced SCC of Cu as canister material during long-term storage of nuclear fuel when exposed to sulfide-containing ground water.

Author statement

F.Z. performed the first literature survey, conducted the synchrotron experiments, and wrote the manuscript. C.Ö. conducted the synchrotron experiments, performed data analysis, and wrote the manuscript. M.L. performed DFT calculations, joined the synchrotron experiment, and wrote the manuscript. T.M. and U.L. supported and conducted the synchrotron experiments, and contributed to the manuscript writting. V. R.-H., L.C. and E.I. prepared the samples, performed corrosion exposure experiment, and contributed to the manuscript writing. J.P. acquired the funding, coordinated the project, planned and conducted experiments, and wrote the manuscript.

Data availability statement

The raw/processed data required to reproduce these findings will be shared by the corresponding author upon reasonable request.

Declaration of Competing Interest

The authors declare that they have no known competing financial interests or personal relationships that could have appeared to influence the work reported in this paper.

Acknowledgements

The financial support from NKS (Contract AFT/NKS-R(19)127/2) is greatly acknowledged. We are also grateful for the funding support from Swedish Research Council's program Röntgen-Ångström Cluster "In-situ High Energy X-ray Diffraction from Electrochemical Interfaces (HEXCHEM)" (project no. 2015-06092) and for PETRA III at DESY for providing the access to the beamline P21.2 for the HEXRD measurement. Moreover, we thank the Swedish National Infrastructure for Computing (SNIC) for providing the Swedish super-computing resource that enabled the DFT calculations.

Appendix A. Supplementary data

Supplementary material related to this article can be found, in the online version, at doi:https://doi.org/10.1016/j.corsci.2021.109390.

References

[1] Z.T. Wang Ju, Ten years progress of the radioactive waste disposal, The International Progress 7 (2003) 476.
[2] Design and Production of the KBS-3 Repository, SKB-TR-10-12, Swedish Nuclear Fuel and Waste Management Co., Sweden, 2010 updated in 2013.
[3] T. Saanio, A. Ikonen, P. Keto, T. Kirkkomäki, T. Kukkola, J. Nieminen, H. Raiko, Design of the Disposal Facility 2012, POSIVA-WR-13-17, Finland, 2013.
[4] T. Hedman, A. Nyström, C. Thegerström, Swedish containers for disposal of spent nuclear fuel and radioactive waste, C. R. Phys. 3 (2002) 903.
[5] F. King, C. Lilja, K. Pedersen, P. Pitkänen, M. Vähänen, An Update of the State-of-the-art Report on the Corrosion of Copper Under Expected Conditions in a Deep Geologic Repository, SKB-10-67, Swedish Nuclear Fuel and Waste Management Co., Sweden, 2010.
[6] C. Padovani, F. King, C. Lilja, D. Féron, S. Necib, D. Crusset, V. Deydier, N. Diomidis, R. Gaggiano, T. Ahn, P.G. Keech, D.D. Macdonald, H. Asano, N. Smart, D.S. Hall, H. Hänninen, D. Engelberg, J.J. Noël, D.W. Shoesmith, The corrosion behaviour of candidate container materials for the disposal of high-level waste and spent fuel – a summary of the state of the art and opportunities for synergies in future R&D, Corrosion Eng. Sci. Technol. 52 (2017) 227.
[7] A. Hedin, A.J. Johansson, C. Lilja, M. Boman, P. Berastegui, R. Berger, M. Ottosson, Corrosion of copper in pure O_2-free water? Corros. Sci. 137 (2018) 1.
[8] R. Becker, J. Öijerholm, Slow Strain Rate Testing of Copper in Sulfide Rich Chloride Containing Deoxygenated Water at 90 °C, SSM 2017:02, Swedish Radiation Authority, Sweden, 2017.
[9] R. Becker, A. Forsström, Y. Yagodzinskyy, H. Hänninen, M. Heikkilä, Sulphide-induced Stress Corrosion Cracking and Hydrogen Absorption in Copper Exposed to

Sulphide and Chloride Containing Deoxygenated Water at 90°C, SSM 2020:01, Swedish Radiation Authority, Sweden, 2020.
[10] C.M. Lousada, I.L. Soroka, Y. Yagodzinskyy, N.V. Tarakina, O. Todoshchenko, H. Hänninen, P.A. Korzhavyi, M. Jonsson, Gamma radiation induces hydrogen absorption by copper in water, Sci. Rep. 6 (2016) 24234.
[11] I. Soroka, N. Chae, M. Jonsson, On the mechanism of γ-radiation-induced corrosion of copper in water, Corros. Sci. 182 (2021), 109279.
[12] D.S. Hall, M. Behazin, W.J. Binns, P.G. Keech, An evaluation of corrosion processes affecting copper-coated nuclear waste containers in a deep geological repository, Prog. Mater. Sci. 118 (2021) 100766, https://doi.org/10.1016/j.pmatsci.2020.100766.
[13] Supplementary Information on Canister Integrity Issues, SKB TR-19-15, Swedish Nuclear Fuel and Waste Management Co., Sweden, 2019.
[14] F. King, M. Kolar, I. Puigdomenech, P. Pitkänen, C. Lilia, Modeling microbial sulfate reduction and the consequences for corrosion of copper canisters, Mater. Corros. 72 (2021) 339.
[15] L. Carpén, P. Rajala, E. Huttunen-Saarivirta, M. Bomberg, Corrosion behavior of copper in simulated anoxic groundwater inoculated with sulfate reducing bacteria and methanogens. Corrosion 2017, NACE International, New Orleans, Louisiana, USA, 2017, p. 15.
[16] K. Pedersen, Microbial Processes in Radioactive Waste Disposal, SKB-TR-00-04, Swedish Nuclear Fuel and Waste Management Co., Sweden, 2000.
[17] N. Taniguchi, M. Kawasaki, Influence of sulfide concentration on the corrosion behavior of pure copper in synthetic seawater, J. Nucl. Mater. 379 (2008) 154.
[18] E. Huttunen-Saarivirta, P. Rajala, L. Carpén, Corrosion behaviour of copper under biotic and abiotic conditions in anoxic ground water: electrochemical study, Electrochim. Acta 203 (2016) 350.
[19] L. Carpén, P. Rajala, M. Bomberg, Corrosion of copper in anoxic ground water in the presence of SRB, Corros. Sci. Technol. 17 (2018) 147.
[20] E. Huttunen-Saarivirta, E. Ghanbari, F. Mao, P. Rajala, L. Carpén, D.D. Macdonald, Kinetic properties of the passive film on copper in the presence of sulfate-reducing bacteria, J. Electrochem. Soc. 165 (2018) C450.
[21] E. Huttunen-Saarivirta, P. Rajala, M. Bomberg, L. Carpén, Corrosion of copper in oxygen-deficient groundwater with and without deep bedrock micro-organisms: characterization of microbial communities and surface processes, Appl. Surf. Sci. 396 (2017) 1044.
[22] D. Kong, C. Dong, A. Xu, C. Man, C. He, X. Li, Effect of sulfide concentration on copper corrosion in anoxic chloride-containing solutions, J. Mater. Eng. Perform. 26 (2017) 1741.
[23] J. Chen, Z. Qin, D. Shoesmith, Long-term corrosion of copper in a dilute anaerobic sulfide solution, Electrochim. Acta 56 (2011) 7854.
[24] T. Martino, R. Partovi-Nia, J. Chen, Z. Qin, D.W. Shoesmith, Mechanisms of film growth on copper in aqueous solutions containing sulphide and chloride under voltammetric conditions, Electrochim. Acta 127 (2014) 439.
[25] J. Chen, Z. Qin, D. Shoesmith, Kinetics of corrosion film growth on copper in neutral chloride solutions containing small concentrations of sulfide, J. Electrochem. Soc. 157 (2010) C338.
[26] J. Chen, Z. Qin, T. Martino, M. Guo, D. Shoesmith, Copper transport and sulphide sequestration during copper corrosion in anaerobic aqueous sulphide solutions, Corros. Sci. 131 (2018) 245.
[27] J. Smith, J. Wren, M. Odziemkowski, D. Shoesmith, The electrochemical response of preoxidized copper in aqueous sulfide solutions, J. Electrochem. Soc. 154 (2007) C431.
[28] H. Hollmark, P. Keech, J. Vegelius, L. Werme, L.-C. Duda, X-ray absorption spectroscopy of electrochemically oxidized Cu exposed to Na_2S, Corros. Sci. 54 (2012) 85.
[29] J. Condon, T. Schober, Hydrogen bubbles in metals, J. Nucl. Mater. 207 (1993) 1.
[30] T. Nieh, W. Nix, The formation of water vapor bubbles in copper and their effect on intergranular creep fracture, Acta Metall. 28 (1980) 557.
[31] S. Nakahara, Microscopic mechanism of the hydrogen effect on the ductility of electroless copper, Acta Metall. 36 (1988) 1669.
[32] Y. Okinaka, H. Straschil, The effect of inclusions on the ductility of electroless copper deposits, J. Electrochem. Soc. 133 (1986) 2608.
[33] J. Angeli, A. Bengtson, A. Bogaerts, V. Hoffmann, V.-D. Hodoroaba, E. Steers, Glow discharge optical emission spectrometry: moving towards reliable thin film analysis–a short review, J. Anal. At. Spectrom. 18 (2003) 670.
[34] M. Ganchenkova, Y. Yagodzinskyy, V. Borodin, H. Hänninen, Effects of hydrogen and impurities on void nucleation in copper: simulation point of view, Philos. Mag. 94 (2014) 3522.
[35] Å. Martinsson, R. Sandström, C. Lilja, Hydrogen in Oxygen-free, Phosphorus-doped Copper: Charging Techniques, Hydrogen Contents and Modelling of Hydrogen Diffusion and Depth Profile, SKB-TR-13-09, Swedish Nuclear Fuel and Waste Management Co., Sweden, 2013.
[36] Å. Martinsson, R. Sandström, Hydrogen depth profile in phosphorus-doped, oxygen-free copper after cathodic charging, J. Mater. Sci. 47 (2012) 6768.
[37] E. Isotahdon, L. Carpen, P. Rajala, Corrosion of copper in geological repository for nuclear waste - the effect of oxic phase on the corrosion behaviour of copper in anoxic environment, in: The European Corrosion Congress, EUROCORR 2019, 2019.
[38] G. Ashiotis, A. Deschildre, Z. Nawaz, J.P. Wright, D. Karkoulis, F.E. Picca, J. Kieffer, The fast azimuthal integration Python library: pyFAI, J. Appl. Crystallogr. 48 (2015) 510.
[39] B. Delley, An all-electron numerical method for solving the local density functional for polyatomic molecules, J. Chem. Phys. 92 (1990) 508.
[40] B. Delley, From molecules to solids with the DMol 3 approach, J. Chem. Phys. 113 (2000) 7756.
[41] J.P. Perdew, J.A. Chevary, S.H. Vosko, K.A. Jackson, M.R. Pederson, D.J. Singh, C. Fiolhais, Atoms, molecules, solids, and surfaces: applications of the generalized gradient approximation for exchange and correlation, Phys. Rev. B 46 (1992) 6671.
[42] M. O'reilly, X. Jiang, J. Beechinor, S. Lynch, C. NíDheasuna, J. Patterson, G. Crean, Investigation of the oxidation behaviour of thin film and bulk copper, Appl. Surf. Sci. 91 (1995) 152.
[43] C. Gattinoni, A. Michaelides, Atomistic details of oxide surfaces and surface oxidation: the example of copper and its oxides, Surf. Sci. Rep. 70 (2015) 424.
[44] Q.L. Tang, H_2S splitting on Cu (110): insight from combined periodic density functional theory calculations and microkinetic simulation, Int. J. Quantum Chem. 113 (2013) 1992.
[45] C.M. Lousada, A.J. Johansson, P.A. Korzhavyi, Molecular and dissociative adsorption of water and hydrogen sulfide at perfect and defective Cu (110) surfaces, Phys. Chem. Chem. Phys. 19 (2017) 8111.
[46] U. Eberle, M. Felderhoff, F. Schueth, Chemical and physical solutions for hydrogen storage, Angew. Chemie Int. Ed. 48 (2009) 6608.
[47] F. Fujita, T. Sohmura, Hydrogen in stainless steel and Fe-Ni alloys, Le Journal de Physique Colloques 37 (1976). C6-379-C6-383.
[48] R.H. Rusli, T. Fujita, Approximation of hydrogen induced delayed fracture of overlaid cladding in pressure vessels steel structure, J. Eng. Technol. Sci. 40 (2008) 110.
[49] A. Klamt, G. Schüürmann, COSMO: a new approach to dielectric screening in solvents with explicit expressions for the screening energy and its gradient, J. Chem. Soc. Perkin Trans. 2 (1993) 799.
[50] B. Delley, The conductor-like screening model for polymers and surfaces, Mol. Simul. 32 (2006) 117.
[51] H. Magnusson, K. Frisk, Self-diffusion and Impurity Diffusion of Hydrogen, Oxygen, Sulphur and Phosphorus in Copper, SKB TR-13-24, Swedish Nuclear Fuel and Waste Management, Sweden, 2013.
[52] H. Magnusson, K. Frisk, Thermodynamic Evaluation of Cu-H-O-S-P System - Phase Stabilities and Solubilities for OFP-copper, SKB TR-13-11, Swedish Nuclear Fuel and Waste Management Co., Sweden, 2013.
[53] D. Gupta, Comparative Cu diffusion studies in advanced metallizations of Cu and Al-Cu based thin films, MRS Online Proc. Lib. Arch. 337 (1994).
[54] Corrosion Calculations Report for the Safety Assessment SR-Site, SKB TR-10-66, Swedish Nuclear Fuel and Waste Management Company, Sweden, 2010.
[55] G. Caskey Jr, A. Dexter, M. Holzworth, M. Louthan Jr, R. Derrick, The effect of oxygen on hydrogen transport in copper, Corrosion 32 (1976) 370.
[56] H. Magnusson, K. Frisk, Diffusion, permeation and solubility of hydrogen in copper, J. Phase Equilibria Diffus. 38 (2017) 65.
[57] SR-Site – Sulphide Content in the Groundwater at Forsmark, SKB TR-10-39, Swedish Nuclear Fuel and Waste Management Co., Sweden, 2010.
[58] R. Wu, F. Seitisleam, R. Sandström, L. Jin, Creep Crack Growth in Phosphorus Alloyed Oxygen Free Copper, SKB R-11-11, Swedish Nuclear Fuel and Waste Management Co., Sweden, 2011.
[59] Y. Yagodzinskyy, E. Malitckii, T. Saukkonen, H. Hänninen, Hydrogen-enhanced creep and cracking of oxygen-free phosphorus-doped copper, Scr. Mater. 67 (2012) 931.
[60] Y. Yagodzinskyy, E. Malitckii, F. Tuomisto, H. Hänninen, Hydrogen-induced strain localization in oxygen-free copper in the initial stage of plastic deformation, Philos. Mag. 98 (2017) 727.
[61] A. Forsström, S. Bossuyt, Y. Yagodsinskyy, K. Tsuzaki, H. Hänninen, Strain localization in copper canister FSW welds for spent nuclear fuel disposal, J. Nucl. Mater. 523 (2019) 347.
[62] F. King, R. Newman, Stress Corrosion Cracking of Copper Canisters, SKB TR-10-04, Swedish Nuclear Fuel and Waste Management Co., Sweden, 2010.